A discontinuous Galerkin method for continuum dislocation dynamics in a fully-coupled elastoplasticity model

Zur Erlangung des akademischen Grades eines

Doktors der Naturwissenschaften

von der KIT-Fakultät für Mathematik des Karlsruher Instituts für Technologie (KIT) genehmigte

Dissertation

von

Lydia Wagner

Tag der mündlichen Prüfung: 22. Mai 2019

1. Referent: Prof. Dr. Christian Wieners

2. Referent: Prof. Dr. Willy Dörfler

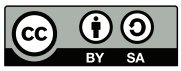

Für meinen Vater

Contents

CHAPTER 1
Introduction

1.1 Motivation

In many engineering applications, components of all sorts are designed to be resilient while being lightweight and inexpensive in terms of material need. They are tailored for a particular purpose including specific expected external forces which the material needs to withstand without failure. Nowadays, the selection of shape and material is usually based on numerical simulations of the material behavior under loading instead of expensive experimental studies. A major task of mechanical engineering and materials science is the development of accurate material models which allow to predict the material response to outer forces.

It is well-known that metals can be permanently deformed if the applied forces are high enough. Such plastic deformation is of large interest for many applications. Classical plasticity models provide estimates for critical stresses. If these stresses are surpassed, a plastic deformation is expected. Additionally, the models comprise stress–strain relations describing the flow and hardening properties. They are typically of phenomenological nature and scale-invariant. These models are widely used and offer reliable results in most cases. On small scales, however, they often fail to describe the experimentally observed physical effects. In the magnitude of few micro-meters, the microstructure of crystalline materials like metals distinctly affects the overall behavior and thereby a size-dependent deformation process is caused. This behavior can be explained by taking a closer look at the microstructure: plasticity is caused by line defects in the crystalline structure called dislocations. When subjected to stresses they can move and interact. This causes local inhomogeneities in the material which provoke plastic deformation and might induce a size-dependent macroscopic material behavior.

Owing to these local effects, the view on plasticity significantly depends on the scale of observation, see Figure 1.1. In order to represent small scale effects, continuum plasticity

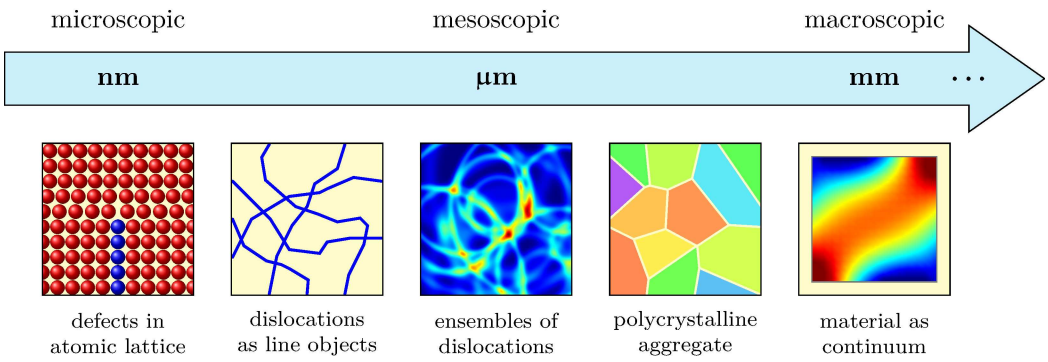

Figure 1.1: Length scales in plasticity

models can be complemented by internal variables. By adding an internal length scale, size effects are approximated in strain gradient plasticity theories. These are a direct generalization of the classical continuum plasticity models and are still not self-contained but include parameters based on experimental data.

For the development of plasticity models which account more precisely for the underlying physics, an in-depth analysis of crystal defects on atomic scale is necessary. The prediction of dislocation motion and interaction is a key challenge in materials science. There are various models which aim to describe the physical observations in dependence of material properties, load and environmental factors like temperature. These models are inherently based on small scales. They are generally not feasible for engineering applications due to a very high computational effort involved. Using simplifications and averaging procedures, physical models describing the dislocation microstructure on larger scales have been developed.

Averaging processes naturally imply a loss of information. The representation of local effects in a larger scale model is a great challenge and the subject of current research. In particular, the interactions of dislocations due to their local stress fields are of great interest because of their importance for the macroscopic material behavior. In a bottom-up approach, these are successively included in mesoscale plasticity models.

Despite the advances in the development of dislocation based plasticity models, the numerical simulation of plastic material behavior in consideration of dislocation motion still entails high computational costs. The development of efficient numerical methods for the approximation of plasticity is thus indispensable. Since the experimentally observed material behavior is largely influenced by local effects, a precise account of those is required while keeping the computational effort within reasonable limits.

1.2 Objective of this work

The goal of this work is the development of a numerical scheme approximating a specific material model for dislocation based plasticity. The considered physical model involves the solution of a macroscopic boundary value problem and of a system of evolution equations representing the dislocation motion.

We aim for a mathematical formulation of all corresponding relations allowing for a discretization in space and time of the overall plasticity problem. In order to derive a fully-coupled numerical approximation method, in particular a coupling mechanism relating the approximations of the macroscopic problem and of the microscopic problem describing the dislocation motion is required.

Besides the development of a numerical scheme, another objective of this work is a rigorous numerical investigation of its properties. This necessitates the design of suitable test configurations. After analyzing the numerical convergence behavior in simplified situations, more complex numerical tests can be performed with a view to examining whether the physically expected effects can be retained within the approximation scheme.

1.3 Scope and outline

This work is structured as follows.

We start by summarizing the considered physical model in Chapter 2, 3 and 4. In Chapter 2, the basic physical quantities in continuum mechanics are introduced. We provide a description of the kinematic relations of solid bodies and state the concepts of strain and stress. This allows to formulate a framework for elastoplasticity based on the impulse and angular momentum balance laws and a relation of strains and stresses in a linear elastic small strain constitutive law.

Chapter 3 provides a different view of solids. Metals and many other materials in the solid state exhibit a crystalline structure. In this chapter, we show the basics of crystallography and introduce the concept of dislocations including the fundamentals of dislocation motion.

The principles presented in Chapter 2 and 3 are conflated in a continuum elastoplasticity model considering dislocation motion. In Chapter 4, a short overview of the development of respective approaches is given. To this end, the concept of dislocation density is explained. Finally, the continuum dislocation dynamics model is specified. It is supplemented by a velocity law for dislocation densities. Together with the elastoplasticity model given in Chapter 2, this yields the fully-coupled model which is the foundation of this work.

Chapter 5 is dedicated to a formal derivation of a numerical scheme approximating the dislocation density motion. For this purpose, a splitting method is applied yielding two coupled linear conservation laws. Their space discretization is done using a finite-dimensional setting based on the discontinuous Galerkin method. It is complemented by an implicit midpoint rule for time discretization.

An approximation of the fully-coupled model is achieved in Chapter 6. First, a space discretization of the elastoplasticity problem stated in Chapter 2 based on a conforming finite element method is given. It is followed by a coupling mechanism connecting the approximation of the macroscopic problem and the approximated dislocation density motion as proposed in Chapter 4. The fully-coupled algorithm for single crystals is extended by a formulation allowing for polycrystals.

We validate the presented numerical method in Chapter 7. This is achieved by providing several configurations with analytical reference solutions and performing a series of numerical tests. Here, we examine the approximation of the macroscopic problem and the dislocation dynamics separately.

In Chapter 8 the developed algorithm is applied to two fully-coupled polycrystalline settings. We first investigate a bicrystalline geometry subject to a prescribed shear stress using a simplified dislocation mobility law. Then the approximation scheme for the full model is investigated in a tensile test of a tricrystal. The results of this numerical experiment are compared to reference data based on a smaller scale model.

We conclude this work with a short summary and an outlook on potential follow-up work in Chapter 9.

1.4 Acknowledgment

This work is embedded in the research group *Dislocation based plasticity* (FOR1650) funded by the German research foundation Deutsche Forschungsgemeinschaft (DFG). We gratefully acknowledge the financial support by the DFG. Furthermore, we would like to emphasize that the collaboration within the research group had a major impact on this work and cannot be overstated.

The development of the numerical scheme and the numerical tests presented in this work required computations involving a fairly high amount of resources. Parts thereof were performed on the supercomputer ForHLR funded by the Ministry of Science, Research and the Arts Baden-Württemberg and by the Federal Ministry of Education and Research.

CHAPTER 2
Continuum mechanics

In this chapter, the basics of continuum mechanics are presented and the related notation used throughout this work is introduced. In particular, a short introduction to the fundamental concepts of kinematics and materials theory is given. Moreover, a small strain setting for elastoplasticity is stated which provides a basis for the dislocation based plasticity model given in Chapter 4. Deeper insights to continuum mechanics can be found in various textbooks, such as e.g. Gurtin (1982) and Marsden and Hughes (1994).

2.1 Kinematics

The objective of *continuum mechanics* is to describe and investigate the deformation of bodies with continuous mass density under load. An object is thus considered a continuum in the Euclidean space and not an ensemble of point masses.

Throughout this work, we consider a solid body $\mathcal{B} \subset \mathbb{R}^3$ which is assumed to be connected and bounded with piecewise smooth boundary $\partial\mathcal{B}$. Kinematical equations are used to describe the motion of $\mathcal{B}$. For this purpose, $\mathcal{B}$ is considered the reference configuration starting from which a time-dependent motion and deformation process is measured. For each material point $\mathbf{x} \in \mathcal{B}$, the displacement at a given instant of time t is denoted by $\mathbf{u}(t, \mathbf{x})$ with the displacement function $\mathbf{u}\colon [0, \infty) \times \mathcal{B} \to \mathbb{R}^3$. Consequently, the current position of a material point $\mathbf{x} \in \mathcal{B}$ at time $t \in [0, \infty)$ is given by the motion function

$$\boldsymbol{\chi}\colon [0, \infty) \times \mathcal{B} \to \mathbb{R}^3, \qquad (t, \mathbf{x}) \mapsto \mathbf{x} + \mathbf{u}(t, \mathbf{x}).$$

It is illustratively reasonable to require $\boldsymbol{\chi}$ to be injective to avoid distinct material points to be mapped onto the same point in the deformed body. Additionally, $\boldsymbol{\chi}$ (and thus $\mathbf{u}$) is supposed to be at least twice continuously differentiable. This means in particular that no fractures occur.

It is useful to distinguish between a displacement of the body as a whole and a deformation which affects the shape of the body. Motions which do not modify the internal structure of the body are called *rigid body motions*. They cover translations as well as rotations. Deformations which change the relative position of material points to each other in the body are named *strains*. Strains are of great interest for the investigation of material behavior under external loads. They can be measured using the deformation gradient

$$\mathbf{F}(t,\mathbf{x}) = \frac{\partial \boldsymbol{\chi}}{\partial \mathbf{x}}(t,\mathbf{x})$$

as well as the displacement gradient

$$\mathrm{D}\mathbf{u}(t,\mathbf{x}) = \frac{\partial \mathbf{u}}{\partial \mathbf{x}}(t,\mathbf{x}) = \mathbf{F}(t,\mathbf{x}) - \mathbf{I}.$$

The displacement gradient is also called *distortion tensor*. To represent strains in a solid body, the *Green strain tensor*

$$\mathbf{E} = \frac{1}{2}(\mathbf{F}^\top\mathbf{F} - \mathbf{I}) = \frac{1}{2}(\mathrm{D}\mathbf{u} + (\mathrm{D}\mathbf{u})^\top + (\mathrm{D}\mathbf{u})^\top\mathrm{D}\mathbf{u})$$

can be used. It is designed to be symmetric and vanishes for pure rigid body displacements only. In this work, we restrict ourselves to deformations with small strains, i.e. $\|\mathrm{D}\mathbf{u}\| \ll 1$. Then the geometric linearization

$$\mathbf{E} \approx \frac{1}{2}(\mathrm{D}\mathbf{u} + (\mathrm{D}\mathbf{u})^\top) = \mathrm{sym}(\mathrm{D}\mathbf{u})$$

leads to the *infinitesimal strain tensor*

$$\boldsymbol{\varepsilon} = \mathrm{sym}(\mathrm{D}\mathbf{u}) \ .$$

In many situations, it is convenient to understand the infinitesimal strain tensor as a function of the displacement $\boldsymbol{\varepsilon} = \boldsymbol{\varepsilon}(\mathbf{u})$. We do not distinguish explicitly between tensorial quantities and their matrix representation with respect to the Euclidean standard basis $\mathbf{e}_1, \mathbf{e}_2, \mathbf{e}_3$ and thus write

$$\boldsymbol{\varepsilon} = \begin{pmatrix} \varepsilon_{11} & \varepsilon_{12} & \varepsilon_{13} \\ \varepsilon_{12} & \varepsilon_{22} & \varepsilon_{23} \\ \varepsilon_{13} & \varepsilon_{23} & \varepsilon_{33} \end{pmatrix} \in \mathbb{R}^{3\times 3}.$$

The diagonal entries of $\boldsymbol{\varepsilon}$ correspond to *longitudinal* strains which induce a change in length in the respective direction (Figure 2.1a) and are therefore responsible for a change

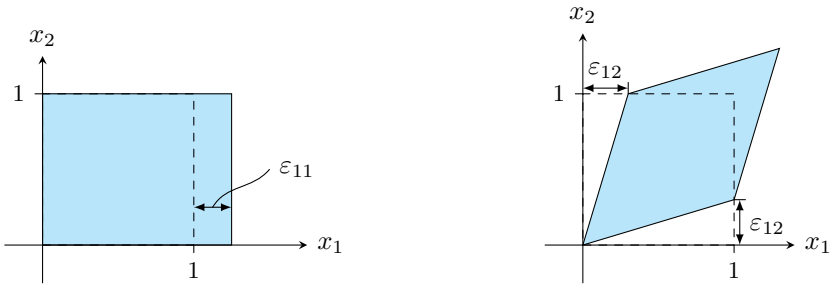

(a) Longitudinal strain (b) Shear strain

Figure 2.1: Illustration of the infinitesimal strain tensor $\boldsymbol{\varepsilon}$

in volume (or dilatation). The remaining components describe *shear* which is a volume preserving deformation resulting from a change in angles, see Figure 2.1b.

2.2 Cauchy stress tensor

Deformation is caused by forces exerted on the body. Volume forces (or body forces), like gravity, act on the whole body $\mathcal{B}$. Forces resulting from a mechanical external load, by contrast, are usually applied on a part of the surface $\partial\mathcal{B}$.

The material response to external forces is stress. It is a measure for forces existing in the interior of the body as a consequence of the externally applied load. Considering an imaginary cut surface with normal $\mathbf{n}$ in $\mathcal{B}$, the stress vector $\mathbf{t}$ describes the force the neighboring parts of $\mathcal{B}$ exert on each other. The stress vector $\mathbf{t}$ in $\mathbf{x} \in \mathcal{B}$ is obtained via the limit case of a resulting force $\mathrm{d}\mathbf{f}$ acting on an infinitesimal area $\mathrm{d}\mathcal{A}$ in the surface as force per area by

$$\mathbf{t}(\mathbf{n}, \mathbf{x}) = \frac{\mathrm{d}\mathbf{f}}{\mathrm{d}\mathcal{A}}.$$

See Figure 2.2 for an illustration of the stress vector $\mathbf{t}$. The stress vectors for all possible cutting planes can be summarized in the *Cauchy stress tensor*

$$\boldsymbol{\sigma} = \begin{pmatrix} \sigma_{11} & \sigma_{12} & \sigma_{13} \\ \sigma_{21} & \sigma_{22} & \sigma_{23} \\ \sigma_{31} & \sigma_{32} & \sigma_{33} \end{pmatrix} \in \mathbb{R}^{3\times 3}$$

such that

$$\mathbf{t}(\mathbf{n}, \mathbf{x}) = \boldsymbol{\sigma}(\mathbf{x})\mathbf{n}\,.$$

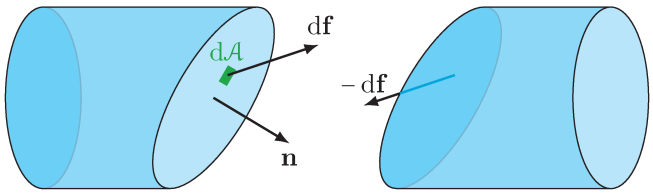

Figure 2.2: Illustration of the stress vector $\mathbf{t} = \frac{\mathrm{d}\mathbf{f}}{\mathrm{d}\mathcal{A}}$

The diagonal entries of the stress tensor are *normal stresses*, i.e. stresses with parallel force and cutting plane normal. For non-diagonal entries the first index gives the normal direction, whereas the second one denotes the force direction. These stresses are called *shear stresses*.

2.3 Balance equations

The physical behavior of solid bodies is usually formulated using balance laws. These postulate that the change in a physical quantity is composed of production in the volume and flux across its boundary. In the context of continuum mechanics the equilibria of mass, impulse, angular momentum and energy are of particular importance.

For an arbitrary volume part $V(t) \subset \boldsymbol{\chi}(\mathcal{B}, t)$ with mass density $\varrho\colon V(t) \to [0, \infty)$ and volume force density $\mathbf{b}_\mathcal{B}\colon V(t) \to \mathbb{R}^3$ the impulse balance is given by

$$\frac{\mathrm{d}}{\mathrm{d}t} \int_{V(t)} \varrho(t,\mathbf{x}) \partial_t \mathbf{u}(t,\mathbf{x}) \,\mathrm{d}\mathbf{x} = \int_{V(t)} \varrho(t,\mathbf{x}) \mathbf{b}_\mathcal{B}(t,\mathbf{x}) \,\mathrm{d}\mathbf{x} + \int_{\partial V(t)} \boldsymbol{\sigma}(t,\mathbf{x}) \mathbf{n} \,\mathrm{d}\mathbf{a}.$$

Using the mass balance and integration by parts, the partial differential equation

$$\varrho(t,\mathbf{x}) \partial_t^2 \mathbf{u}(t,\mathbf{x}) = \varrho(t,\mathbf{x}) \mathbf{b}_\mathcal{B}(t,\mathbf{x}) + \operatorname{div} \boldsymbol{\sigma}(t,\mathbf{x})$$

can be derived. In this work, quasi-static processes are considered. This means that the behavior is time-dependent but inertial effects are neglected, i.e. $\partial_t^2 \mathbf{u}$ is assumed to vanish. Under this assumption the impulse balance law reads

$$-\operatorname{div} \boldsymbol{\sigma}(t,\mathbf{x}) = \varrho(t,\mathbf{x}) \mathbf{b}_\mathcal{B}(t,\mathbf{x}).$$

The equilibrium equation for the angular momentum is

$$\frac{\mathrm{d}}{\mathrm{d}t} \int_{V(t)} \varrho(t,\mathbf{x}) (\mathbf{x} \times \partial_t \mathbf{u}(t,\mathbf{x})) \,\mathrm{d}\mathbf{x} = \int_{V(t)} \varrho(t,\mathbf{x}) (\mathbf{x} \times \mathbf{b}_\mathcal{B}(t,\mathbf{x})) \,\mathrm{d}\mathbf{x} + \int_{\partial V(t)} \mathbf{x} \times (\boldsymbol{\sigma}(t,\mathbf{x}) \mathbf{n}) \,\mathrm{d}\mathbf{a}.$$

It can be shown that the angular momentum balance implies that the Cauchy stress tensor is symmetric, i.e.

$$\boldsymbol{\sigma} = \boldsymbol{\sigma}^\top$$

(Marsden and Hughes, 1994, Theorem 2.10).

2.4 Materials theory

A material model relates the deformation to the material response, i.e. the prevalent stresses. Since rigid body motions do not influence the stress state, it suffices to consider the strains. One distinguishes two fundamental types of material behavior. The material behavior is called *elastic* if only the current strains influence the current stresses and the history of deformation is irrelevant. This implies that an elastic material retains the original shape after unloading. The deformation is said to be *reversible*. If, in contrast, the stresses depend on previous deformations – or equivalently the deformation is *irreversible*, i.e. remains after unloading – the material behavior is called *inelastic*.

Different types of inelastic material behavior are known. In this work, we only consider *plasticity* which will be explained in more detail in the subsequent chapter. Experience has shown that most materials have both elastic and plastic properties. This suggests in the case of small strains an additive decomposition of the distortion tensor into elastic and plastic parts

$$\mathrm{D}\mathbf{u} = \boldsymbol{\beta}^{\mathrm{el}} + \boldsymbol{\beta}^{\mathrm{pl}}$$

which induces the decomposition

$$\boldsymbol{\varepsilon} = \boldsymbol{\varepsilon}^{\mathrm{el}} + \varepsilon^{\mathrm{pl}}, \qquad \boldsymbol{\varepsilon}^{\mathrm{el}} = \mathrm{sym}(\boldsymbol{\beta}^{\mathrm{el}})\,,\ \boldsymbol{\varepsilon}^{\mathrm{pl}} = \mathrm{sym}(\boldsymbol{\beta}^{\mathrm{pl}})$$

for the infinitesimal strain tensor. Then $\boldsymbol{\beta}^{\mathrm{pl}}$ and $\boldsymbol{\varepsilon}^{\mathrm{pl}}$ describe the plastic part of the deformation.

The simplest elastic material law for a homogeneous body is a linear dependence between strains and stresses

$$\boldsymbol{\sigma} = \mathbb{C}[\boldsymbol{\varepsilon}^{\mathrm{el}}] = \mathbb{C}[\boldsymbol{\varepsilon} - \boldsymbol{\varepsilon}^{\mathrm{pl}}]$$

with a fourth order stiffness tensor $\mathbb{C} \in \mathbb{R}^{3\times3\times3\times3}$. This relation is known as *Hooke's law* and is normally sufficient for the description of the elastic behavior of, e.g., metals. For

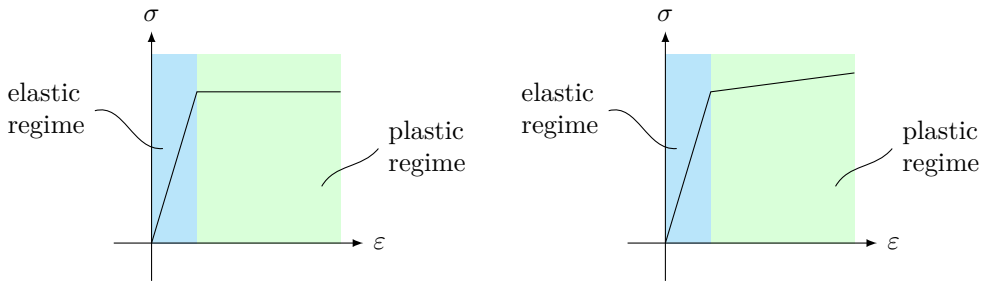

(a) ideal plastic (b) linear hardening

Figure 2.3: Stress-strain curves for linear elastic ideal plastic material behavior and linear elastic material behavior with linear hardening

an isotrope, i.e. direction independent, linear elastic material, it can be described by two constants λ and μ via

$$\boldsymbol{\sigma} = \lambda \operatorname{Tr}(\boldsymbol{\varepsilon})\, \mathbf{I} + 2\mu \boldsymbol{\varepsilon}\,.$$

The material dependent constants λ and μ are called *Lamé parameters*.

Material behavior is often illustrated in stress-strain curves where a scalar stress quantity is depicted in dependence of a scalar strain. For example, a specific component of the stress and the infinitesimal strain tensor is chosen which is of interest for the concrete load state. Such diagrams may result from experimental tests or from numerical simulations. Depending on the material and the test setting (e.g. load or temperature) these diagrams vary greatly. However, different regimes can be identified: usually an elastic regime is followed by a plastic regime. The elastic regime can consist of linear and non-linear elasticity. The plastic regime can be classified according to the slope. In the case of perfect plasticity the stress does not increase in the plastic regime, i.e. the slope vanishes. More typical is a positive slope indicating *hardening*. Thus with increasing plastic deformation, the material strengthens. However, also softening, i.e. a negative slope, can be observed. A schematic depiction of an idealized linear elastoplastic behavior with perfect plasticity and with linear hardening is given in Figure 2.3a and 2.3b.

Classical plasticity theories are built on the observation that plasticity starts when a critical load is applied. Keeping the concept of a stress-strain curve in mind, it is reasonable to model the underlying material behavior via a critical stress and a flow rule which describes the stress-strain behavior when the critical stress is reached. Taking the full Cauchy stress tensor $\boldsymbol{\sigma}$ into account, the critical stress (or the flow condition) can be illustrated as a surface in $\mathbb{R}^3$. The flow rule determines the plastic strain rate $\partial_t \boldsymbol{\varepsilon}^{\mathrm{pl}}$ and is typically supplemented by a hardening rule accounting for a change in the flow condition. Material

laws of this type have in common that they are phenomenological. They are hence based on observations and usually involve parameters which are determined in experiments. The plasticity model which is used in this work is of fundamentally different structure. For this reason we refrain from a detailed description of classical continuum plasticity theories.

2.5 Small strain elastoplasticity

Proceeding from the previous sections, we are now able to state the small strain elastoplasticity problem. For a given plastic strain tensor $\boldsymbol{\varepsilon}^{\mathrm{pl}}$ and a volume force density $\mathbf{b}_{\mathcal{B}}$, we aim to find the displacement $\mathbf{u}$ such that the impulse and angular momentum equilibria

$$\begin{aligned} -\operatorname{div}\boldsymbol{\sigma} &= \mathbf{b}_{\mathcal{B}} && \text{in } \mathcal{B}, \\ \boldsymbol{\sigma} &= \boldsymbol{\sigma}^{\top} && \text{in } \mathcal{B} \end{aligned} \tag{2.1}$$

hold and boundary conditions

$$\begin{aligned} \mathbf{u} &= \mathbf{u}_{\mathrm{D}} && \text{on } \partial_{\mathrm{D}}\mathcal{B}, \\ \boldsymbol{\sigma}\mathbf{n} &= \mathbf{t}_{\mathrm{N}} && \text{on } \partial_{\mathrm{N}}\mathcal{B} \end{aligned} \tag{2.2}$$

are satisfied where $\partial_{\mathrm{D}}\mathcal{B} \cup \partial_{\mathrm{N}}\mathcal{B} = \partial\mathcal{B}$ is a non-overlapping decomposition of the boundary into Dirichlet and Neumann part, respectively. The boundary conditions arise from the load state. The Dirichlet boundary condition covers a prescribed displacement $\mathbf{u}_{\mathrm{D}}$. The Neumann boundary accounts for stresses resulting from prescribed forces (or force densities) acting on the boundary.

The small strain elastoplasticity problem is the basis for the plasticity model which we use in this work. We refer to it as the *macroscopic problem*. To resolve the outstanding issue of how to model the plastic strain $\boldsymbol{\varepsilon}^{\mathrm{pl}}$, we need to regard the material on a smaller scale. By doing so, an evolution equation for $\boldsymbol{\varepsilon}^{\mathrm{pl}}$ accounting for the underlying physical effects can be formulated. The concrete choice of the evolution equation will be discussed in Chapter 4.

CHAPTER 3
Dislocations

This chapter provides a short introduction to the fundamentals of crystallography. Based on a perfect single crystal, different types of defects in the crystalline structure are presented. In particular, the concept of dislocations is introduced. We lay a foundation for the elastoplasticity model presented in Chapter 4 by stating the basics of the geometry and motion of dislocations. An extensive introduction to dislocations can be found, e.g., in Hirth and Lothe (1982) and Hull and Bacon (2011).

3.1 Single crystals

Nature tells us that the most stable solid state of chemical elements is a crystalline structure. Atoms, ions and molecules try to minimize their interacting forces by forming a suitable thermodynamical state. Below a certain temperature, they arrange in periodic structures. This reflects that the particles tend to align their environments. Otherwise an imbalance of energies exists which is thermodynamically not favorable. By this means, a discrete translation invariance is established. Solids with these periodicity properties are called *single crystals*.

Typically, lattices are used to describe crystalline structures. For distinction and characterization of different lattice geometries, a single crystal can be represented by a *unit cell* which reproduces the lattice if it is repeated periodically.

The simplest lattice in three dimensions is determined by the simple cubic unit cell, see Figure 3.1a. However, the *body centered cubic* (bcc), Figure 3.1b, and the *face centered cubic* (fcc) lattices, Figure 3.1c, are more common because of the higher packing density. For example chromium and lithium are bcc materials, and aluminium and copper are fcc materials. Furthermore, various other lattice types occur in nature. They are usually classified by their symmetry properties, i.e. the number of inversion, rotation and translation symmetries.

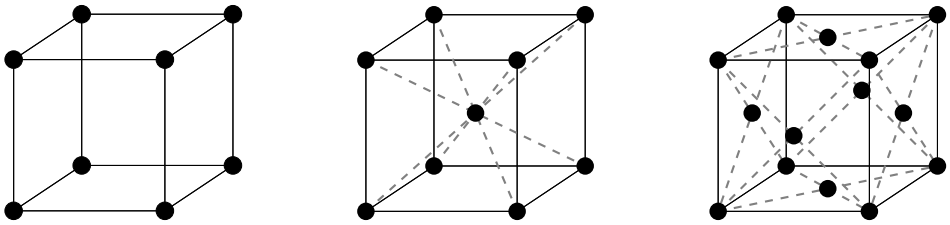

(a) simple cubic (b) body centered cubic (c) face centered cubic

Figure 3.1: Cubic crystal systems

3.2 Lattice defects

Naturally, crystals are rarely perfect but include a large number of defects. This means that the symmetries of the lattice are broken by local irregularities. These can be categorized according to their dimension.

Point defects only affect a single lattice cell. For example a lattice site is vacant, it is occupied by another element or an additional particle is situated between lattice sites on an irregular position.

Line defects occur when lattice bindings are established in an irregular way. Because of the geometry of the lattice, such a defect is repeated through the crystal and a line of defects is observed. They are called *dislocations*.

Two-dimensional crystal defects appear in different forms. When crystals are formed, they often do not have enough time to establish a perfect long-range crystalline structure. In practice, the crystallization starts at several points simultaneously with different crystal orientations. In this way, a material consisting of multiple single crystalline regions is built. Such materials are known as *polycrystals*. Their single crystalline parts are named *grains*. The two-dimensional crystal defects separating two neighboring grains are called *grain boundaries*. Other two-dimensional lattice defects, like stacking faults, antiphase boundaries or twin boundaries, are shifts of single atomic layers in the lattice.

Three-dimensional crystal defects come in the form of inclusions of a different material, precipitates, i.e. inclusions of the same material in a different phase, and voids.

Dislocations are the underlying cause for a crystalline material to show plastic behavior. When external forces are applied to the material, dislocation lines can move due to rearrangement of the lattice bindings. This effect is observed macroscopically as plasticity. For a profound understanding of plasticity it is hence indispensable to investigate dislocation motion.

Other types of crystal defects influence the macroscopic material behavior through their impact on dislocation motion. Point defects as well as two- and three-dimensional crystal defects hinder dislocation motion. For example, grain boundaries affect the material properties. Hall (1951) and Petch (1953) observed a correlation between grain size and hardening known as *Hall-Petch relation*. A small grain size supports hardening. The mechanisms of interactions between dislocations and other crystal defects are not only required to comprehend the macroscopic material behavior. This knowledge can also be exploited in order to design materials of high strength. For example point defects as well as three-dimensional crystal defects can be added artificially to a material. Furthermore, a heat treatment can be used to control the crystallization process and influence the grain size.

3.3 Burgers vector

To obtain a better understanding of dislocation motion and the impact on the overall material behavior, we now take a closer look at the geometry of dislocations. Due to the periodic structure of a single crystal, a single incorrect binding leads to a line of defects through the material. This dislocation line cannot end inside the material. It either ends at a boundary or another crystal defect or it is a closed path.

To describe a dislocation, the *Burgers circuit* is introduced. Starting from a lattice point, a closed path on the lattice around the crystal defect is drawn, see Figure 3.2a. As a consequence of the defect, the same circuit drawn in a perfect crystal is not closed. The vector which closes the path is called *Burgers vector* and denoted with **b**, see Figure 3.2b. Its length indicates the particle spacing in the crystal.

(a) Crystal with line defect (b) Perfect crystal

Figure 3.2: Illustration of the Burgers vector **b**

Dislocations can be characterized by the orientation of the dislocation line direction with respect to the Burgers vector. A dislocation with orthogonal Burgers vector and dislocation line is called *edge dislocation*, see Figure 3.3a. A dislocation with parallel Burgers vector and dislocation line is called *screw dislocation*, see Figure 3.3b. In practice, usually combinations of these two types occur.

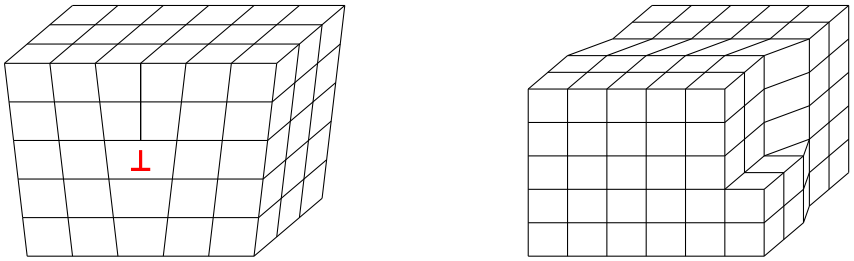

(a) Edge dislocation (b) Screw dislocation

Figure 3.3: Edge and screw dislocations

3.4 Dislocation motion

Dislocations can move due to internal and external stresses. Recalling that a dislocation line is only a practical perception for mislocated lattice bindings, it becomes apparent that its motion is equivalent to a reordering of these bindings. It thus seems natural that dislocation motion is directly related to the crystal lattice structure. Based on the Burgers vector and the dislocation line orientation, different types of dislocation motion can be distinguished.

The most typical behavior is that a dislocation stays on the plane spanned by its line direction and the Burgers vector. The dislocation is said to *glide* on the *slip plane*. Dislocations move perpendicular to their line direction. A dislocation moving towards the boundary exits the volume. When entering or exiting a volume it leaves a step in the surface, see Figure 3.4.

Moreover, other types of dislocation motion can be observed. The movement of a dislocation onto a parallel slip plane directly above or below the current slip plane is called *climbing*. For screw dislocations, the slip plane is not unique since Burgers vector and line direction are parallel. A *cross-slip* is the movement onto an intersecting slip plane which includes the Burgers vector. In this work, dislocation motion is assumed to be restricted to gliding. A brief outlook on generalizations including other types of dislocation motion will be given in Chapter 9.

3.5 Slip systems

Due to the specific crystallographic structure there are preferred directions of dislocation motion inside a grain (or a single crystal). For a given lattice type, an ensemble of a slip plane and a Burgers vector (lying in the plane) is called a *slip system*. A single crystal consists of multiple slip systems. Subsequently, the number of slip systems of a crystalline material is called S.

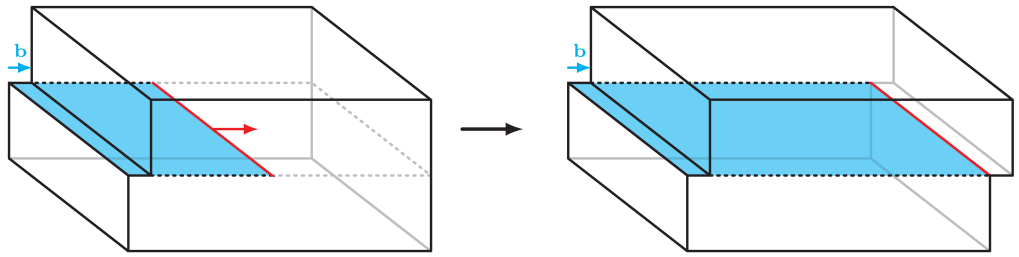

(a) Movement of an edge dislocation entering the volume on the left and leaving on the right

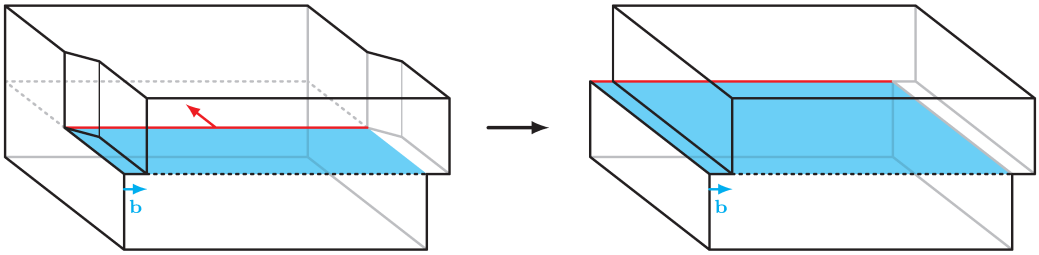

(b) Movement of a screw dislocation entering the volume at the front and leaving at the back

Figure 3.4: Motion of a straight dislocation line

In this work, the following notation for slip systems is used. The Burgers vector of the slip system $s \in \{1, \dots, S\}$ is denoted by $\mathbf{b}_s = b_s \mathbf{d}_s$ with length b_s and Burgers direction $\mathbf{d}_s$, $|\mathbf{d}_s| = 1$. The slip plane is determined by its normal $\mathbf{m}_s$ with $|\mathbf{m}_s| = 1$ and $\mathbf{d}_s \cdot \mathbf{m}_s = 0$. It is denoted by $\Gamma_s = \operatorname{span}\{\mathbf{d}_s, \mathbf{l}_s\}$ where $\mathbf{l}_s = \mathbf{m}_s \times \mathbf{d}_s$. This means in particular that we do not distinguish parallel slip planes, i.e. in each point $\mathbf{p}$ of the lattice we have the slip planes $\mathbf{p} + \Gamma_s$, $s = 1, \dots, S$. We usually determine a slip system s by the right-handed orthonormal system $(\mathbf{d}_s, \mathbf{l}_s, \mathbf{m}_s)$.

Typically, a slip system is not uniquely defined by the slip plane. In other words, there are several slip systems which share the same slip plane but have differing Burgers vectors. For example an fcc crystal has four slip planes, each including three Burgers vectors. Thus in total 12 slip systems exist for fcc materials. In Figure 3.5 the four slip planes are illustrated. Moreover, the 12 slip systems are given in Table 3.1.

3.6 Plastic slip

When multiple dislocations pass through a volume, macroscopically the volume is sheared. In contrast to an elastic shear however, a specimen which is deformed by slipped lattice layers is stress-free. An illustration of both elastic shear and the plastic counterpart is given in Figure 3.6. This motivates the definition of a field quantity describing plastic

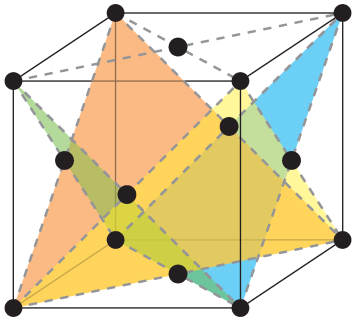

Figure 3.5: Slip planes in an fcc unit cell

s	1	2	3	4	5	6	7	8	9	10	11	12
$\sqrt{3}\,\mathbf{m}_s$	$\begin{pmatrix}1\\1\\1\end{pmatrix}$	$\begin{pmatrix}1\\1\\1\end{pmatrix}$	$\begin{pmatrix}1\\1\\1\end{pmatrix}$	$\begin{pmatrix}-1\\-1\\1\end{pmatrix}$	$\begin{pmatrix}-1\\-1\\1\end{pmatrix}$	$\begin{pmatrix}-1\\-1\\1\end{pmatrix}$	$\begin{pmatrix}1\\-1\\-1\end{pmatrix}$	$\begin{pmatrix}1\\-1\\-1\end{pmatrix}$	$\begin{pmatrix}1\\-1\\-1\end{pmatrix}$	$\begin{pmatrix}-1\\1\\-1\end{pmatrix}$	$\begin{pmatrix}-1\\1\\-1\end{pmatrix}$	$\begin{pmatrix}-1\\1\\-1\end{pmatrix}$
$\sqrt{2}\,\mathbf{d}_s$	$\begin{pmatrix}0\\1\\-1\end{pmatrix}$	$\begin{pmatrix}1\\0\\-1\end{pmatrix}$	$\begin{pmatrix}1\\-1\\0\end{pmatrix}$	$\begin{pmatrix}0\\-1\\-1\end{pmatrix}$	$\begin{pmatrix}-1\\0\\-1\end{pmatrix}$	$\begin{pmatrix}-1\\1\\0\end{pmatrix}$	$\begin{pmatrix}0\\-1\\1\end{pmatrix}$	$\begin{pmatrix}1\\0\\1\end{pmatrix}$	$\begin{pmatrix}1\\1\\0\end{pmatrix}$	$\begin{pmatrix}0\\1\\1\end{pmatrix}$	$\begin{pmatrix}-1\\0\\1\end{pmatrix}$	$\begin{pmatrix}-1\\-1\\0\end{pmatrix}$
$\sqrt{6}\,\mathbf{l}_s$	$\begin{pmatrix}-2\\1\\1\end{pmatrix}$	$\begin{pmatrix}-1\\2\\-1\end{pmatrix}$	$\begin{pmatrix}1\\1\\-2\end{pmatrix}$	$\begin{pmatrix}2\\-1\\1\end{pmatrix}$	$\begin{pmatrix}1\\-2\\-1\end{pmatrix}$	$\begin{pmatrix}-1\\-1\\2\end{pmatrix}$	$\begin{pmatrix}-2\\-1\\-1\end{pmatrix}$	$\begin{pmatrix}-1\\-2\\1\end{pmatrix}$	$\begin{pmatrix}1\\-1\\2\end{pmatrix}$	$\begin{pmatrix}2\\1\\-1\end{pmatrix}$	$\begin{pmatrix}1\\2\\1\end{pmatrix}$	$\begin{pmatrix}-1\\1\\2\end{pmatrix}$

Table 3.1: The 12 slip systems of an fcc crystal

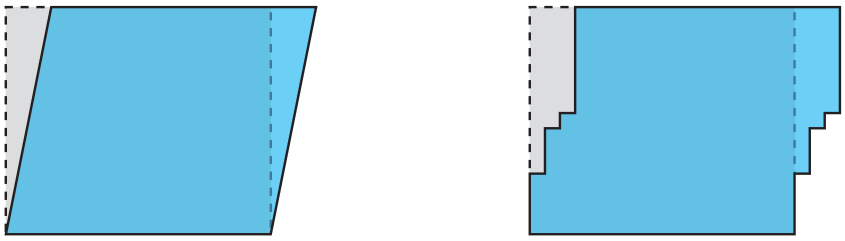

(a) elastic shear (b) plastic slip

Figure 3.6: Elastic shear and plastic slip

deformation similar to the elastic shear strain. The *plastic slip* γ of a single dislocation with Burgers size b and lattice height h is defined as

$$\gamma = \frac{b}{h}$$

and corresponds to the shear angle. For several dislocations of the slip system s lying in a volume V, the (average) plastic slip γ_s is given by

$$\gamma_s = \frac{A_s b_s}{V} \tag{3.1}$$

with A_s denoting the total slipped area in V.

In a crystal with multiple slip systems, the plastic distortion tensor $\boldsymbol{\beta}^{\mathrm{pl}}$ is assumed to be the sum of the scalar plastic slips γ_s of the slip systems $s = 1, \ldots, S$ by

$$\boldsymbol{\beta}^{\mathrm{pl}} = \sum_{s=1}^{S} \gamma_s \mathbf{m}_s \otimes \mathbf{d}_s. \tag{3.2}$$

Consequently, the plastic part of the infinitesimal strain tensor reads

$$\boldsymbol{\varepsilon}^{\mathrm{pl}} = \sum_{s=1}^{S} \gamma_s \operatorname{sym}(\mathbf{m}_s \otimes \mathbf{d}_s)\,.$$

3.7 Eigenstresses

Dislocations invoke a local stress field. The stresses are called *eigenstresses* of the dislocation. Through these stresses, dislocations close to each other can interact. Depending on their relative orientation, the corresponding stress fields can amplify or diminish each other. When their stresses are of opposite sign, dislocations attract each other, whereas for stresses of the same sign repellent forces are present. In the special case of dislocations of opposite direction in the same slip system, the stresses annihilate. Therefore the

eigenstresses are of vital importance for dislocation motion and thus for the macroscopic material behavior.

For straight dislocation lines in infinitely large bodies, the eigenstresses can be specified analytically. The non-vanishing eigenstresses of a pure edge dislocation with slip system $\mathbf{d} = \mathbf{e}_1$, $\mathbf{l} = \mathbf{e}_2$, $\mathbf{m} = \mathbf{e}_3$ and Burgers size b arise as

$$\sigma_{11}^{\mathrm{ana}}(\mathbf{x}) = -\frac{\mu b}{2\pi(1-\nu)} \frac{x_3(3x_1^2 + x_3^2)}{(x_1^2 + x_3^2)^2}, \qquad \sigma_{33}^{\mathrm{ana}}(\mathbf{x}) = \frac{\mu b}{2\pi(1-\nu)} \frac{x_3(x_1^2 - x_3^2)}{(x_1^2 + x_3^2)^2},$$
$$\sigma_{13}^{\mathrm{ana}}(\mathbf{x}) = \frac{\mu b}{2\pi(1-\nu)} \frac{x_1(x_1^2 - x_3^2)}{(x_1^2 + x_3^2)^2}, \qquad \sigma_{22}^{\mathrm{ana}}(\mathbf{x}) = -\frac{\mu b \nu}{\pi(1-\nu)} \frac{x_3}{x_1^2 + x_3^2},$$

see Hirth and Lothe (1982, Chapter 3). Here, ν is the Poisson ratio which can be written in terms of the Lamé constants as

$$\nu = \frac{\lambda}{2(\lambda + \mu)}.$$

In a similar way the stress field of a screw dislocation is obtained. Again for the slip system $\mathbf{d} = \mathbf{e}_1$, $\mathbf{l} = \mathbf{e}_2$ and $\mathbf{m} = \mathbf{e}_3$ the non-vanishing components read

$$\sigma_{12}^{\mathrm{ana}}(\mathbf{x}) = \frac{\mu b}{2\pi} \frac{x_3}{x_2^2 + x_3^2}, \qquad \sigma_{13}^{\mathrm{ana}}(\mathbf{x}) = -\frac{\mu b}{2\pi} \frac{x_2}{x_2^2 + x_3^2}.$$

A dislocation of mixed type can be decomposed into an edge and a screw part. Then its stress field is obtained as linear combination of the individual stress fields in the sense of the superposition principle.

CHAPTER 4
A continuum crystal plasticity model

In the previous chapters, the fundamental concepts of continuum mechanics and of crystalline materials including dislocations have been introduced. In the present chapter, both perceptions of solids are merged into a continuum plasticity theory which accounts for the dislocation microstructure. After briefly mentioning a discrete model for dislocation dynamics, a spatial averaging approach for dislocation ensembles is presented. Based on this, we derive the continuum dislocation dynamics model we use throughout this work in a condensed form. It is complemented by a constitutive mobility law. Altogether, this chapter fills the gap in the elastoplasticity model presented in Chapter 2.

4.1 Discrete dislocation dynamics

The first step towards a continuum theory of crystal plasticity is to consider dislocations as connected curves in $\mathbb{R}^3$ instead of directly regarding line defects on the atomic scale. For a complete description of the pertinent physical effects, not only a representation of the geometry of dislocations but also a mobility law for dislocations comprising their interactions is required.

A widely used method for elastoplasticity including the crystal structure via discrete dislocation lines is the *discrete dislocation dynamics* (DDD) theory; see e.g. Kubin and Canova (1992), Ghoniem and Sun (1999), Weygand et al. (2002) for an introduction to DDD. Dislocation lines are represented by nodes in the volume which are connected by straight lines in DDD. They lie on discrete slip planes embedded in a linear elastic medium. Each line is attributed by a displacement field and a stress field based on the eigenstresses as seen in Section 3.7. These are superposed with the respective macroscopic field. The motion of dislocations is realized in DDD using constitutive mobility laws. The main driving force of dislocation motion is the projection of the Cauchy stress tensor onto the respective slip plane.

DDD meets the needs in many regards. For example, the Hall-Petch relation could be observed in several DDD simulations, e.g. Balint et al. (2008), Kumar et al. (2009) and Ahmed and Hartmaier (2010). However, the resolution of individual dislocation lines comes with the drawback of high computational costs. In particular, the computational effort increases with the number of dislocations in the computational domain. The numerical costs scale quadratically with the number of line segments in the volume. There are attempts to decrease the computational expense by exploiting that the dislocation eigenstresses descend hyperbolically. Nevertheless, the DDD theory is limited in its application. It is e.g. restricted to rather small geometries.

4.2 Dislocation density

In order to avoid the distinction of particular dislocations, it is reasonable to make use of an averaging approach and introduce a *dislocation density*. For this purpose, we assume to have a finite set $\mathcal{C}$ of curves $\mathbf{c}\colon [0, L_\mathbf{c}] \to \mathcal{B}$ parameterized by arc length representing the set of dislocations in a domain $\mathcal{B}$. For a given environment $V(\mathbf{x})$ of $\mathbf{x} \in \mathcal{B}$, we define the dislocation density ρ in $\mathbf{x}$ by

$$\rho(\mathbf{x}) = \frac{1}{|V(\mathbf{x})|} \sum_{\mathbf{c}\in\mathcal{C}} \int_{\mathbf{c}\cap V(\mathbf{x})} 1 \,\mathrm{d}l$$

(Sandfeld et al., 2010). Thus the dislocation density measures the total dislocation line length in a control volume. Due to the periodicity of a crystal lattice, it is convenient to choose the averaging volumes such that $|V(\mathbf{x})| = |V(\mathbf{y})|$ for all $\mathbf{x}, \mathbf{y} \in \mathcal{B}$. The dislocation density ρ is a continuous representation of the discrete dislocation lines and the size of the averaging volumes corresponds to the spatial resolution. In the limit case $|V(\mathbf{x})| \longrightarrow 0$, the discrete dislocation ensemble is recovered.

Owing to the nature of averaging processes, there is a loss of information when considering a dislocation density instead of the discrete dislocation network itself. The dislocation density contains information about the amount of dislocations as well as their location (subject to some uncertainty depending on the averaging volume size). However, information on the dislocation line orientation is lost. This is unsuitable for a comprehensive mobility characterization of dislocations. We have already seen in Section 3.3 that dislocations move perpendicular to their line direction. Therefore, it is essential to retain information on the dislocation line orientation.

For this reason, we define an additional averaged quantity $\boldsymbol{\kappa}\colon \mathcal{B} \to \Gamma$ by

$$\boldsymbol{\kappa}(\mathbf{x}) = \frac{1}{|V(\mathbf{x})|} \sum_{\mathbf{c}\in\mathcal{C}} \int_{\mathbf{c}\cap V(\mathbf{x})} \mathbf{c}'(l) \,\mathrm{d}l. \tag{4.1}$$

with $\mathbf{c}'$ denoting the tangent to the curve $\mathbf{c} \in \mathcal{C}$. By construction, it holds $|\boldsymbol{\kappa}| \leq \rho$. If dislocations of opposite line orientation lie in the same averaging volume, $\boldsymbol{\kappa}$ may vanish for non-vanishing ρ. Hence, in general indeed $|\boldsymbol{\kappa}| \neq \rho$. This motivates to categorize dislocation density dependent on whether the corresponding $\boldsymbol{\kappa}$ vanishes or not. Considering a specific control volume, $\boldsymbol{\kappa}$ can be understood as its net dislocation line orientation. On this account, $|\boldsymbol{\kappa}|$ is called *geometrically necessary dislocation* (GND) density and accordingly $\boldsymbol{\kappa}$ itself is referred to as *GND density vector*. Conversely $\rho - |\boldsymbol{\kappa}|$ is named *statistically stored dislocation* (SSD) density and quantifies the amount of dislocation density whose orientation information is lost in the averaging procedure.

Considering a single crystal with multiple slip systems, it is expedient to define the dislocation density as well as the GND density vector separately for each slip system. Thus for a slip system s, we have the dislocation density ρ_s and the GND density vector $\boldsymbol{\kappa}_s$. Knowing that a dislocation line in the slip system s lies on a slip plane $\mathbf{p} + \Gamma_s$, we deduce $\boldsymbol{\kappa}_s \cdot \mathbf{m}_s = 0$ and thus write

$$\boldsymbol{\kappa}_s = \kappa_s^1 \mathbf{d}_s + \kappa_s^2 \mathbf{l}_s.$$

By definition, κ_s^1 measures the screw part of the dislocation density and κ_s^2 the edge part.

4.3 Classical continuum plasticity

The first efforts to a continuum crystal plasticity theory have been made by Kondo (1952), Nye (1953), Bilby et al. (1955) and Kröner (1958) who presented similar continuum dislocation theories. We briefly repeat Kröner's theory in the following for the single slip case, i.e. $S = 1$.

Based on the formulation of the Burgers vector as closure vector of a Burgers circuit in Section 3.3, a net Burgers vector in a surface $\mathcal{A}$ which includes multiple dislocations can be defined as

$$\mathbf{b}^{\mathrm{net}} = \mathbf{d} \int_{\partial \mathcal{A}} \gamma \, \mathbf{m} \cdot \mathrm{d}\mathbf{s}.$$

Using Stokes' theorem yields

$$\mathbf{b}^{\mathrm{net}} = \mathbf{d} \int_{\partial \mathcal{A}} \gamma \, \mathbf{m} \cdot \mathrm{d}\mathbf{s} = \mathbf{d} \int_{\mathcal{A}} \nabla \times (\gamma \mathbf{m}) \cdot \mathrm{d}\mathbf{a} = \int_{\mathcal{A}} \mathbf{d} \otimes \nabla \times (\gamma \mathbf{m}) \, \mathrm{d}\mathbf{a}.$$

For $S = 1$, the plastic distortion given in Equation (3.2) simplifies to

$$\boldsymbol{\beta}^{\mathrm{pl}} = \gamma \, \mathbf{m} \otimes \mathbf{d}. \tag{4.2}$$

Thus we can write

$$\mathbf{b}^{\mathrm{net}} = \int_{\mathcal{A}} \mathbf{d} \otimes \nabla \times (\gamma \mathbf{m}) \, \mathrm{d}\mathbf{a} = \int_{\mathcal{A}} \left(\nabla \times (\gamma \mathbf{m}) \otimes \mathbf{d}\right)^{\top} \mathrm{d}\mathbf{a} = \int_{\mathcal{A}} \left(\nabla \times \boldsymbol{\beta}^{\mathrm{pl}}\right)^{\top} \mathrm{d}\mathbf{a}.$$

This motivates to define the dislocation density tensor

$$\boldsymbol{\alpha} = \nabla \times \boldsymbol{\beta}^{\mathrm{pl}} \tag{4.3}$$

such that

$$\mathbf{b}^{\mathrm{net}} = \int_{\mathcal{A}} \boldsymbol{\alpha}^{\top} \, \mathrm{d}\mathbf{a}.$$

The tensorial dislocation measure $\boldsymbol{\alpha}$ is usually referred to as *Kröner-Nye tensor*.

The Kröner-Nye tensor $\boldsymbol{\alpha}$ is an averaged dislocation measure. Analogously to the considerations of a scalar dislocation density in the previous section, it can not distinguish between individual dislocations lying in the same averaging surface $\mathcal{A}$. Dislocations of opposite sign in the averaging surface cancel out. In terms of the previous section, the Kröner-Nye tensor for a single slip system can be written as

$$\boldsymbol{\alpha} = \boldsymbol{\kappa} \otimes \mathbf{b}. \tag{4.4}$$

The evolution of the Kröner-Nye tensor $\boldsymbol{\alpha}$ and the plastic distortion $\boldsymbol{\beta}^{\mathrm{pl}}$ are related via Equation (4.3) as

$$\partial_t \boldsymbol{\alpha} = \nabla \times \partial_t \boldsymbol{\beta}^{\mathrm{pl}}$$

which reflects that it is in general not possible to build a closed dislocation theory solely based on the Kröner-Nye tensor. If one assumes, however, that all dislocations share the same orientation or that the spatial resolution is chosen sufficiently high such that each dislocation is resolved, the Kröner-Nye tensor can be used to derive a dislocation evolution theory. Assuming that a velocity vector field $\mathbf{v} \in \Gamma$ which is perpendicular to the dislocation line orientation is given, the relation

$$\partial_t \boldsymbol{\beta}^{\mathrm{pl}} = (\mathbf{v} \times \boldsymbol{\kappa}) \otimes \mathbf{b} = \mathbf{v} \times \boldsymbol{\alpha} \tag{4.5}$$

implies for a purely GND density the evolution equation

$$\partial_t \boldsymbol{\alpha} = \nabla \times (\mathbf{v} \times \boldsymbol{\alpha}) \tag{4.6}$$

(Mura, 1963). Writing $\mathbf{v} = \frac{v}{|\boldsymbol{\kappa}|}\boldsymbol{\kappa}\times\mathbf{m}$ we obtain

$$\partial_t \boldsymbol{\beta}^{\mathrm{pl}} = \frac{v}{|\boldsymbol{\kappa}|}((\boldsymbol{\kappa}\times\mathbf{m})\times\boldsymbol{\kappa}) \otimes \mathbf{b} = v|\boldsymbol{\kappa}|\mathbf{m}\otimes\mathbf{b} = vb|\boldsymbol{\kappa}|\mathbf{m}\otimes\mathbf{d}.$$

Thus with the definition of the single slip plastic distortion (4.2), we see that Equation (4.5) can also be written as scalar equation

$$\partial_t \gamma = v\rho b \tag{4.7}$$

which is known as Orowan equation and can also be deduced directly from the definition of the plastic slip (3.1). In general, however, (i.e. if $\rho \neq |\boldsymbol{\kappa}|$) Equation (4.6) does not hold true (Sandfeld et al., 2010) but it can serve as a prototype for a kinematical dislocation model which does allow for a closed theory.

4.4 Higher-dimensional continuum dislocation dynamics

There have been several attempts to derive a closed dislocation based plasticity theory (e.g. Groma, 1997, El-Azab, 2000, Acharya, 2001, Groma et al., 2003, Arsenlis et al., 2004). They all aim to incorporate the dislocation orientation in some way. However, the theories come along with significant deficiencies restricting their utility. Most are limited to certain line orientations. The model by Groma et al. (2003), for example, only represents straight edge dislocations which are distinguished by their sign. Based on the concept introduced by El-Azab (2000) the development of a theory allowing for curved dislocations has been established.

A major advance has been accomplished by Hochrainer (2007) and Hochrainer et al. (2007) who generalized the idea of the classical dislocation density tensor $\boldsymbol{\alpha}$ by introducing the second order dislocation density tensor $\boldsymbol{\alpha}^{\mathrm{II}}$. The theory is based on the definition of the configuration space $\mathcal{B}\times\mathbb{R}/(2\pi\mathbb{Z})$ which includes the dislocation line orientation with respect to the Burgers direction as additional dimension. Accounting for the artificially added dimension, the theory is named *higher-dimensional continuum dislocation dynamics* (hdCDD). We summarize the basic concept of the hdCDD theory for the single slip case ($S = 1$) in the following. For a formal derivation of the theory we refer to the original work Hochrainer (2007) and Hochrainer et al. (2007). The (less formal) notation used below – which is valid if only dislocation gliding is considered – is based on Sandfeld et al. (2010, 2015).

For a given curve $\mathbf{c} \in \mathcal{C}$ in $\mathcal{B}$, we define a lifted curve in the configuration space

$$\mathbf{C}\colon [0, L_{\mathbf{c}}] \to \mathcal{B}\times[0,2\pi), \qquad l \mapsto (\mathbf{c}(l), \varphi(l))$$

where $\varphi \in [0, 2\pi)$ is the angle between the tangential direction

$$\mathbf{c}'(l) = \cos\varphi\,\mathbf{d} + \sin\varphi\,\mathbf{l}$$

and the Burgers direction $\mathbf{d}$. Then the tangent on the lifted curve $\mathbf{C}$ is given by

$$\mathbf{C}'(l) = (\mathbf{c}'(l), k(l))$$

where $k\colon [0, L_{\mathbf{c}}] \to \mathbb{R}$ denotes the (signed) curvature

$$k(l) = (\mathbf{c}'(l) \times \mathbf{m}) \cdot \mathbf{c}''(l).$$

For a set $\mathcal{C}^{\mathrm{II}}$ of curved dislocations in the configuration space, we can now define a higher-dimensional GND density vector $\boldsymbol{\kappa}^{\mathrm{II}}$ similar to $\boldsymbol{\kappa}$ in Equation (4.1) given by

$$\boldsymbol{\kappa}^{\mathrm{II}}\colon \mathcal{B} \times [0, 2\pi) \to \Gamma \times \mathbb{R}, \qquad (\mathbf{x}, \varphi) \mapsto \frac{1}{|V(\mathbf{x}, \varphi)|} \sum_{\mathbf{C} \in \mathcal{C}^{\mathrm{II}}} \int_{\mathbf{C} \cap V(\mathbf{x}, \varphi)} \mathbf{C}'(l)\,\mathrm{d}l.$$

The averaging is now performed in a volume $V(\mathbf{x}, \varphi) \subset \mathcal{B} \times [0, 2\pi)$ in the configuration space. Therefore we do not need to distinguish GND and SSD density anymore. With projection $\Pi\colon \Gamma \times \mathbb{R} \to \Gamma$ we can thus define a scalar dislocation density ρ^{II} by

$$\rho^{\mathrm{II}}\colon \mathcal{B} \times [0, 2\pi) \to \mathbb{R}, \qquad (\mathbf{x}, \varphi) \mapsto \left|\Pi(\boldsymbol{\kappa}^{\mathrm{II}}(\mathbf{x}, \varphi))\right|.$$

This way, the full orientation information of the discrete dislocations is retained. Based on the tangent $\mathbf{C}'$ we define a generalized line orientation

$$\mathbf{L}\colon \mathcal{B} \times [0, 2\pi) \to \Gamma \times \mathbb{R}, \qquad (\mathbf{x}, \varphi) \mapsto (\cos\varphi\,\mathbf{d} + \sin\varphi\,\mathbf{l}, k^{\mathrm{II}}(\mathbf{x}, \varphi))$$

with k^{II} denoting the averaged curvature

$$k^{\mathrm{II}}(\mathbf{x}, \varphi) = \frac{1}{|V(\mathbf{x}, \varphi)|} \sum_{\mathbf{C} \in \mathcal{C}^{\mathrm{II}}} \int_{\mathbf{C} \cap V(\mathbf{x}, \varphi)} k(l)\,\mathrm{d}l.$$

Now, the second order dislocation density tensor $\boldsymbol{\alpha}^{\mathrm{II}}$ is defined in analogy to the classical one (4.4) as

$$\boldsymbol{\alpha}^{\mathrm{II}}(\mathbf{x}, \varphi) = \rho^{\mathrm{II}}(\mathbf{x}, \varphi)\mathbf{L}(\mathbf{x}, \varphi) \otimes \mathbf{b} = \boldsymbol{\kappa}^{\mathrm{II}}(\mathbf{x}, \varphi) \otimes \mathbf{b}.$$

For a given velocity v, we can define a generalized velocity in the configuration space

$$\mathbf{V}\colon \mathcal{B} \times [0, 2\pi) \to \Gamma \times \mathbb{R}, \qquad (\mathbf{x}, \varphi) \mapsto (v\cos\varphi\,\mathbf{l} - v\sin\varphi\,\mathbf{d}, -\mathbf{L} \cdot \widehat{\nabla} v)$$

with gradient $\widehat{\nabla} = (\partial_{\mathbf{d}}, \partial_{\mathbf{l}}, \partial_{\varphi})$. Then the evolution equation for the second order density tensor $\boldsymbol{\alpha}^{\mathrm{II}}$ is given as

$$\partial_t \boldsymbol{\alpha}^{\mathrm{II}} = \widehat{\nabla} \times (\mathbf{V} \times \boldsymbol{\alpha}^{\mathrm{II}})$$

which is a direct generalization of Equation (4.6). The evolution equation for $\boldsymbol{\alpha}^{\mathrm{II}}$ can be written easier accessibly as system for the dislocation density ρ^{II} and the curvature density $q^{\mathrm{II}} = \rho^{\mathrm{II}} k^{\mathrm{II}}$ as

$$\begin{aligned}
\partial_t \rho^{\mathrm{II}} &= -\widehat{\nabla} \cdot (\rho \mathbf{V}) + qv \\
\partial_t q^{\mathrm{II}} &= -\widehat{\nabla} \cdot (q \mathbf{V}) - \rho(\mathbf{L} \cdot \widehat{\nabla}(\mathbf{L} \cdot \widehat{\nabla} v)).
\end{aligned}$$

Sandfeld et al. (2015) presented a numerical solution method for the hdCDD theory which includes the line orientation as additional computational dimension. Dislocation motion is simulated on representative slip planes belonging to the same slip system.

4.5 Continuum dislocation dynamics

The hdCDD theory fills the gap in the classical continuum dislocation theory based on the Kröner-Nye tensor. The additional dimension of the configuration space, however, limits its application since it significantly increases the computational effort. Hence it is ineligible for a fully three-dimensional setup including multiple slip systems. For this reason, simplifications of the hdCDD theory have been developed which attempt to keep the advantage of a closed theory based on spatial averaging but reduce the numerical expense. The resulting models are known under the name *continuum dislocation dynamics* (CDD).

We have seen that the hdCDD theory can be formulated in two scalar quantities ρ^{II} and q^{II}. A simplified CDD theory can be derived via a multipole series expansion of ρ^{II} and q^{II} (Hochrainer, 2015). Thereby for each variable a series of alignment tensors of increasing order is obtained. In this way, the additional dimension for the line orientation is swapped for a series of further field variables which each involve an additional evolution equation. For a feasible model, the series expansions need to be truncated. Depending on where we cut the expansion, a set of additional variables with corresponding evolution equations is obtained.

It turns out that the terms for q^{II} of order one and higher are redundant and do not need to be included as additional variables (Monavari et al., 2016). In a CDD theory including

the zeroth and first order term for ρ^{II} and the zeroth order term for q^{II}, we find the field variables

$$\rho(\mathbf{x}) = \int_0^{2\pi} \rho^{\mathrm{II}}(\mathbf{x}, \varphi)\,\mathrm{d}\varphi, \qquad \boldsymbol{\kappa}(\mathbf{x}) = \int_0^{2\pi} \boldsymbol{\kappa}^{\mathrm{II}}(\mathbf{x}, \varphi)\,\mathrm{d}\varphi, \qquad q(\mathbf{x}) = \int_0^{2\pi} q^{\mathrm{II}}(\mathbf{x}, \varphi)\,\mathrm{d}\varphi.$$

The dislocation density ρ and the GND density vector $\boldsymbol{\kappa}$ correspond to the respective quantities defined in Section 4.2. The information about the average line curvature in q obtained via the detour through the higher-dimensional framework, however, allows now to complete the kinematic setting. The corresponding evolution equations are

$$\begin{aligned}
\partial_t \rho &= -\nabla \cdot (v\boldsymbol{\kappa} \times \mathbf{m}) + qv \\
\partial_t \boldsymbol{\kappa} &= \nabla \times (v\rho\mathbf{m}) \\
\partial_t q &= \nabla \cdot (v\mathbf{Q} - \mathbf{A}\nabla v)
\end{aligned}$$

where $\mathbf{Q}$ is a first order and $\mathbf{A}$ is a second order tensor which both depend on higher order alignment tensors. Thus for a closed theory they need to be approximated using $\rho, \boldsymbol{\kappa}$ and q. In the special cases of either pure GND or pure SSD density, $\mathbf{A}$ can be expressed exactly in terms of ρ and $\boldsymbol{\kappa}$. Linear interpolation between these two special cases yields the approximation

$$\mathbf{A} \approx \frac{1}{2|\boldsymbol{\kappa}|^2}\big((\rho + |\boldsymbol{\kappa}|)\boldsymbol{\kappa} \otimes \boldsymbol{\kappa} + (\rho - |\boldsymbol{\kappa}|)\boldsymbol{\kappa}^{\perp} \otimes \boldsymbol{\kappa}^{\perp}\big)$$

where $\boldsymbol{\kappa}^{\perp} = \boldsymbol{\kappa} \times \mathbf{m}$ (Hochrainer et al., 2014). It is also possible to find an approximation for $\mathbf{Q}$ which is exact if either GND or SSD density is in place by

$$\mathbf{Q} \approx -\frac{q}{\rho}\boldsymbol{\kappa}^{\perp}$$

(Hochrainer et al., 2014). Using these two closure assumptions, the full system reads

$$\partial_t \rho = -\nabla \cdot (v\boldsymbol{\kappa} \times \mathbf{m}) + qv \tag{4.8a}$$

$$\partial_t \boldsymbol{\kappa} = \nabla \times (v\rho\mathbf{m}) \tag{4.8b}$$

$$\partial_t q = -\nabla \cdot \left(v\frac{q}{\rho}\boldsymbol{\kappa}^{\perp} + \frac{1}{2|\boldsymbol{\kappa}|^2}\big((\rho + |\boldsymbol{\kappa}|)\boldsymbol{\kappa} \otimes \boldsymbol{\kappa} + (\rho - |\boldsymbol{\kappa}|)\boldsymbol{\kappa}^{\perp} \otimes \boldsymbol{\kappa}^{\perp}\big)\nabla v\right). \tag{4.8c}$$

This is the version of the simplified CDD theory which we use subsequently. We therefore refer to Equation (4.8) as *CDD system*.

Other choices for approximations of $\mathbf{Q}$ and $\mathbf{A}$ are possible. A comparison of different closure assumption can be found in Monavari et al. (2014).

The CDD system as presented here covers a wide variety of dislocation structures. However, there are cases where the first order series approximation is not sufficient. We refer to Monavari et al. (2016) for an investigation of the higher order approximation including corresponding closure assumptions.

The CDD system formulated for the single slip case (4.8) serves to complete the macroscopic elastoplasticity model presented in Section 2.5 by introducing $\rho_s, \boldsymbol{\kappa}_s, q_s$ for each slip system $s = 1, \dots, S$ separately. Then the plastic distortion (3.2) is obtained by computing the plastic slips γ_s, $s = 1, \dots, S$, via Orowan's equation (4.7).

4.6 Dislocation velocity

In the previous sections, we have derived a continuum dislocation theory comprising the kinematical relations. In these considerations, the dislocation velocity v_s in the slip system s is always assumed to be a known field quantity. Now we complement the CDD model by a velocity law based on the macroscopic stress state and the dislocation microstructure represented by the CDD variables.

Dislocation motion is driven by the locally present stresses. It is common to assume that the local stress state can be described by an effective stress τ_s^{eff} in the slip system $s = 1, \dots, S$ which is a superposition of several stress terms. In this work, we assume the effective stress to be given as

$$\tau_s^{\mathrm{eff}} = \tau_s^{\mathrm{res}} - \tau_s^{\mathrm{b}}$$

with τ_s^{res} denoting the *resolved shear stress* and τ_s^{b} denoting the *back stress*.

As a consequence of the macroscopic load state, the Cauchy stress tensor $\boldsymbol{\sigma}$ resulting from the balance laws (2.1) is obtained. The resolved shear stress τ_s^{res} responsible for dislocation gliding is given by projection onto the specific glide system

$$\tau_s^{\mathrm{res}} = \mathbb{C}[\boldsymbol{\varepsilon} - \boldsymbol{\varepsilon}^{\mathrm{pl}}] : (\mathbf{m}_s \otimes \mathbf{d}_s).$$

The resolved shear stress in particular comprises the dislocation eigenstresses, cf. Section 3.7.

Additionally, a back stress is included which represents dislocation interactions which cannot be resolved by the macroscopic stress term τ_s^{res}. It is assumed to take the form

$$\tau_s^{\mathrm{b}} = \frac{D\mu b_s}{\rho_s} \nabla \cdot \boldsymbol{\kappa}_s^{\perp}$$

where D is a material parameter (Groma et al., 2003). A way to determine D can be found in Schmitt et al. (2015). The back stress can be evaluated from the plastic shear strain γ_s by

$$\tau_s^{\mathrm{b}} = -\frac{D\mu}{\rho_s}\nabla \cdot \big(\mathbf{m}_s \times (\mathbf{m}_s \times \nabla\gamma_s)\big) = -\frac{D\mu}{\rho_s}\nabla_s \cdot \nabla_s\gamma_s$$

with the projected gradient $\nabla_s = \mathbf{d}_s(\mathbf{d}_s \cdot \nabla) + \mathbf{l}_s(\mathbf{l}_s \cdot \nabla)$.

A common assumption is that dislocation motion only takes place if a critical stress is surpassed on the respective glide system. In analogy to continuum mechanics, this stress is referred to as yield stress τ_s^{y}. Furthermore, the dislocation velocity v_s is assumed to be proportional to the Burgers size b_s and a material constant B known as drag coefficient such that the full velocity law reads

$$v_s = \frac{b_s}{B}\operatorname{sgn}(\tau_s^{\mathrm{eff}})\max\Big\{0, |\tau_s^{\mathrm{eff}}| - \tau_s^{\mathrm{y}}\Big\}. \tag{4.9}$$

The Taylor-type yield stress is given by

$$\tau_s^{\mathrm{y}}(\rho_1, \dots, \rho_S) = \mu b_s a\sqrt{\sum_{n=1}^{S}\rho_n}$$

with a denoting a material parameter (Taylor, 1934). Hence, the yield stress includes the dislocation density of all slip systems. It can be extended if it is known how dislocations on different slip systems interact for a specific crystal system. Then the more detailed yield stress term reads

$$\tau_s^{\mathrm{y}}(\rho_1, \dots, \rho_S) = \mu b_s\sqrt{\sum_{n=1}^{S}a_{sn}\rho_n}. \tag{4.10}$$

(Franciosi et al., 1980) with coefficients a_{sn}, $s, n = 1, \dots, S$, describing the interaction between dislocations located on two slip systems s and n.

The matrix $(a_{sn})_{sn} \in \mathbb{R}^{S\times S}$ of interaction coefficients is symmetric. For fcc crystals, the interaction coefficents have been determined in DDD simulations by Devincre et al. (2006) and Kubin et al. (2008). Due to symmetries of fcc crystals, the interaction matrix can be written using six parameters $a_{\mathrm{h}}, a_{\mathrm{l}}, a_{\mathrm{g}}, a_{\mathrm{c}}, a_{\mathrm{s}}, a_{\mathrm{p}}$ each describing a different type of dislocation interaction. The concrete choice of parameters we use for the numerical tests in Chapter 8 is stated in Table 4.1.

a_h	a_l	a_g	a_c	a_s	a_p
0.07	0.122	0.137	0.625	0.122	0.122
Hirth	Lomer	glissile	collinear	self	coplanar

Table 4.1: Parameters for different types of dislocation interactions in fcc crystals according to Kubin et al. (2008)

The resulting interaction matrix for fcc crystals $\mathbf{A}^\mathrm{fcc} = (a_{sn})_{sn} \in \mathbb{R}^{12\times 12}$ is given by

$$\mathbf{A}^\mathrm{fcc} = \begin{pmatrix}
a_\mathrm{s} & a_\mathrm{p} & a_\mathrm{p} & a_\mathrm{h} & a_\mathrm{l} & a_\mathrm{g} & a_\mathrm{c} & a_\mathrm{g} & a_\mathrm{g} & a_\mathrm{h} & a_\mathrm{g} & a_\mathrm{l} \\
a_\mathrm{p} & a_\mathrm{s} & a_\mathrm{p} & a_\mathrm{l} & a_\mathrm{h} & a_\mathrm{g} & a_\mathrm{g} & a_\mathrm{h} & a_\mathrm{l} & a_\mathrm{g} & a_\mathrm{c} & a_\mathrm{g} \\
a_\mathrm{p} & a_\mathrm{p} & a_\mathrm{s} & a_\mathrm{g} & a_\mathrm{g} & a_\mathrm{c} & a_\mathrm{g} & a_\mathrm{l} & a_\mathrm{h} & a_\mathrm{l} & a_\mathrm{g} & a_\mathrm{h} \\
a_\mathrm{h} & a_\mathrm{l} & a_\mathrm{g} & a_\mathrm{s} & a_\mathrm{p} & a_\mathrm{p} & a_\mathrm{h} & a_\mathrm{g} & a_\mathrm{l} & a_\mathrm{c} & a_\mathrm{g} & a_\mathrm{g} \\
a_\mathrm{l} & a_\mathrm{h} & a_\mathrm{g} & a_\mathrm{p} & a_\mathrm{s} & a_\mathrm{p} & a_\mathrm{g} & a_\mathrm{c} & a_\mathrm{g} & a_\mathrm{g} & a_\mathrm{h} & a_\mathrm{l} \\
a_\mathrm{g} & a_\mathrm{g} & a_\mathrm{c} & a_\mathrm{p} & a_\mathrm{p} & a_\mathrm{s} & a_\mathrm{l} & a_\mathrm{g} & a_\mathrm{h} & a_\mathrm{g} & a_\mathrm{l} & a_\mathrm{h} \\
a_\mathrm{c} & a_\mathrm{g} & a_\mathrm{g} & a_\mathrm{h} & a_\mathrm{g} & a_\mathrm{l} & a_\mathrm{s} & a_\mathrm{p} & a_\mathrm{p} & a_\mathrm{h} & a_\mathrm{l} & a_\mathrm{g} \\
a_\mathrm{g} & a_\mathrm{h} & a_\mathrm{l} & a_\mathrm{g} & a_\mathrm{c} & a_\mathrm{g} & a_\mathrm{p} & a_\mathrm{s} & a_\mathrm{p} & a_\mathrm{l} & a_\mathrm{h} & a_\mathrm{g} \\
a_\mathrm{g} & a_\mathrm{l} & a_\mathrm{h} & a_\mathrm{l} & a_\mathrm{g} & a_\mathrm{h} & a_\mathrm{p} & a_\mathrm{p} & a_\mathrm{s} & a_\mathrm{g} & a_\mathrm{g} & a_\mathrm{c} \\
a_\mathrm{h} & a_\mathrm{g} & a_\mathrm{l} & a_\mathrm{c} & a_\mathrm{g} & a_\mathrm{g} & a_\mathrm{h} & a_\mathrm{l} & a_\mathrm{g} & a_\mathrm{s} & a_\mathrm{p} & a_\mathrm{p} \\
a_\mathrm{g} & a_\mathrm{c} & a_\mathrm{g} & a_\mathrm{g} & a_\mathrm{h} & a_\mathrm{l} & a_\mathrm{l} & a_\mathrm{h} & a_\mathrm{g} & a_\mathrm{p} & a_\mathrm{s} & a_\mathrm{p} \\
a_\mathrm{l} & a_\mathrm{g} & a_\mathrm{h} & a_\mathrm{g} & a_\mathrm{l} & a_\mathrm{h} & a_\mathrm{g} & a_\mathrm{g} & a_\mathrm{c} & a_\mathrm{p} & a_\mathrm{p} & a_\mathrm{s}
\end{pmatrix}. \tag{4.11}$$

Here the slip systems are in the same order as in Table 3.1.

CHAPTER 5
Approximation of the CDD system

In this chapter, a numerical approximation scheme for the CDD system presented in Chapter 4 is developed. For this purpose, a single slip system is considered. We start by reformulating the CDD system in order to employ a splitting scheme. This allows to formulate the CDD system in the form of two conservation laws. After providing a general framework for the space discretization of conservation laws using a discontinuous Galerkin approach, we derive semi-discrete approximations of both problems. Here, we also investigate the choice of the numerical flux functions needed for the discontinuous Galerkin scheme. Moreover, we discuss the definition of appropriate boundary conditions as well as the corresponding numerical fluxes. We conclude this chapter with the time discretization using the implicit midpoint rule. This finally yields a fully discrete formulation of the CDD system.

5.1 Reformulation and splitting of the CDD system

In order to deduce a numerical approximation scheme for the CDD system, we start out with a reformulation which emphasizes the mathematical structure of the problem. To this end, throughout this chapter a single slip system with slip plane $\Gamma = \operatorname{span}\{\mathbf{d}, \mathbf{l}\}$ and given dislocation velocity v is considered. The index s indicating all quantities depending on the slip system is subsequently omitted.

Defining $\mathbf{w} = (\rho, \boldsymbol{\kappa})\colon [0,T] \times \mathcal{B} \to \mathbb{R} \times \Gamma$ allows to rewrite the CDD evolution equations (4.8) as

$$\partial_t \mathbf{w} = -\nabla \cdot \mathbf{F}(\mathbf{w}) + \mathbf{G}(q) \qquad \text{in } [0,T] \times \mathcal{B} \tag{5.1a}$$

$$\partial_t q = -\nabla \cdot (\mathbf{f}(\mathbf{w}, q) + \mathbf{g}(\mathbf{w})) \qquad \text{in } [0,T] \times \mathcal{B} \tag{5.1b}$$

with flux functions $\mathbf{F}$ and $\mathbf{f}$ given by

$$\nabla \cdot \mathbf{F}(\mathbf{w}) = \big(\nabla \cdot (v\boldsymbol{\kappa}^\perp), -\nabla \times (v\rho\mathbf{m})\big) \quad \text{and} \quad \mathbf{f}(\mathbf{w}, q) = \frac{vq}{\rho}\boldsymbol{\kappa}^\perp$$

as well as functions

$$\mathbf{G}(q) = (vq, \mathbf{0}) \quad \text{and} \quad \mathbf{g}(\mathbf{w}) = \frac{1}{2|\boldsymbol{\kappa}|^2}\big((\rho + |\boldsymbol{\kappa}|)\boldsymbol{\kappa}^\perp \otimes \boldsymbol{\kappa}^\perp + (\rho - |\boldsymbol{\kappa}|)\boldsymbol{\kappa} \otimes \boldsymbol{\kappa}\big)\nabla v.$$

This formulation suggests a separate discussion of Equation (5.1a) and (5.1b) for the space discretization. For this purpose, we write the CDD system (5.1) as

$$\partial_t \begin{pmatrix} \mathbf{w} \\ q \end{pmatrix} = \begin{pmatrix} -\nabla \cdot \mathbf{F}(\mathbf{w}) \\ 0 \end{pmatrix} + \begin{pmatrix} \mathbf{G}(q) \\ 0 \end{pmatrix} - \begin{pmatrix} \mathbf{0} \\ \nabla \cdot \mathbf{f}(\mathbf{w}, q) \end{pmatrix} - \begin{pmatrix} \mathbf{0} \\ \nabla \cdot \mathbf{g}(\mathbf{w}) \end{pmatrix}$$

and split into the two sub-problems

$$\begin{aligned} \partial_t \mathbf{w} &= -\nabla \cdot \mathbf{F}(\mathbf{w}) + \mathbf{G}(q) \\ \partial_t q &= 0 \end{aligned} \tag{5.2}$$

and

$$\begin{aligned} \partial_t \mathbf{w} &= \mathbf{0} \\ \partial_t q &= -\nabla \cdot \mathbf{f}(\mathbf{w}, q) - \nabla \cdot \mathbf{g}(\mathbf{w}). \end{aligned} \tag{5.3}$$

For fixed v, the first sub-problem (5.2) is a linear conservation law in $\mathbf{w}$ for given q, whereas the second one (5.3) is a linear conservation law in q for given $\mathbf{w}$. It is more convenient to solve both sub-problems separately and then derive an approximation of the whole system composed of the sub-problem solutions instead of directly solving the nonlinear original problem (5.1).

Suppose that approximated solutions for both sub-problems are known by semi-discrete flow functions

$$\Phi_h \colon [0, T] \times ((\mathbb{R} \times \Gamma) \times \mathbb{R}) \to (\mathbb{R} \times \Gamma) \times \mathbb{R} \quad \text{and} \quad \Psi_h \colon [0, T] \times ((\mathbb{R} \times \Gamma) \times \mathbb{R}) \to (\mathbb{R} \times \Gamma) \times \mathbb{R}$$

respectively. Then we aim for an approximated solution of the CDD system (5.1) based on Φ_h and Ψ_h. There are various ways of how to achieve this. We use the two simplest splitting methods: the first-order Lie splitting and the second-order Strang splitting (Strang, 1968). The Lie splitting means we alternately solve both sub-problems. The Strang splitting is a symmetrized modification of the Lie splitting.

For an equidistant time grid with step size $\triangle t$ given by $t_n = n\triangle t$, $n = 1, \dots, N$, we use the following approximations

$$\text{Lie (WQ)} \qquad \begin{pmatrix} \mathbf{w} \\ q \end{pmatrix}(t_n) \approx \big(\Psi_h(\triangle t, \cdot) \circ \Phi_h(\triangle t, \cdot)\big)^n \begin{pmatrix} \mathbf{w} \\ q \end{pmatrix}(0),$$

$$\text{Lie (QW)} \qquad \begin{pmatrix} \mathbf{w} \\ q \end{pmatrix}(t_n) \approx \big(\Phi_h(\triangle t, \cdot) \circ \Psi_h(\triangle t, \cdot)\big)^n \begin{pmatrix} \mathbf{w} \\ q \end{pmatrix}(0),$$

$$\text{Strang (QWQ)} \qquad \begin{pmatrix} \mathbf{w} \\ q \end{pmatrix}(t_n) \approx \big(\Psi_h(\tfrac{1}{2}\triangle t, \cdot) \circ \Phi_h(\triangle t, \cdot) \circ \Psi_h(\tfrac{1}{2}\triangle t, \cdot)\big)^n \begin{pmatrix} \mathbf{w} \\ q \end{pmatrix}(0),$$

$$\text{Strang (WQW)} \qquad \begin{pmatrix} \mathbf{w} \\ q \end{pmatrix}(t_n) \approx \big(\Phi_h(\tfrac{1}{2}\triangle t, \cdot) \circ \Psi_h(\triangle t, \cdot) \circ \Phi_h(\tfrac{1}{2}\triangle t, \cdot)\big)^n \begin{pmatrix} \mathbf{w} \\ q \end{pmatrix}(0).$$

Corresponding to the order in which the sub-problems for $\mathbf{w}$ and q are solved, subsequently the different splitting schemes are abbreviated by (WQ), (QW), (QWQ) and (WQW), respectively.

It remains to specify how to approximate the solutions to the sub-problems (5.2) and (5.3). We start with the space discretization. For a unified treatment, we show that both sub-problems fit in the same mathematical setting. To this end, we first give the analytical framework and then apply it on both CDD evolution equations.

5.2 A general framework for the space discretization

Let $\mathcal{B} \subset \mathbb{R}^3$ be a bounded Lipschitz domain. We consider a bounded time interval $[0, T]$ for given $T > 0$. In the following, we aim to find a function $\mathbf{v} \in C([0,T], \mathcal{D}(A)) \cap C^1((0,T), L^2(\mathcal{B}, \mathbb{R}^J))$ for given $J \in \mathbb{N}$ such that it solves a first-order partial differential equation of the form

$$\partial_t \mathbf{v}(t, \mathbf{x}) + (A\mathbf{v})(t, \mathbf{x}) = \mathbf{b}(t, \mathbf{x}) \quad \text{for } (t, \mathbf{x}) \in (0,T) \times \mathcal{B} \tag{5.4}$$

where $A \colon \mathcal{D}(A) \to L^2(\mathcal{B}, \mathbb{R}^J)$ is a linear differential operator with densely defined domain $\mathcal{D}(A) \subset L^2(\mathcal{B}, \mathbb{R}^J)$ and $\mathbf{b} \in L^2(\mathcal{B}, \mathbb{R}^J)$ is a given right-hand side. The system is completed by an initial condition

$$\mathbf{v}(0, \mathbf{x}) = \mathbf{v}_0(\mathbf{x}) \quad \text{for } \mathbf{x} \in \mathcal{B}$$

for given initial values $\mathbf{v}_0 \in \mathcal{D}(A)$ as well as a boundary condition prescribed on $\partial\mathcal{B}$ for all $t \in (0, T)$.

We assume that the operator A is of divergence type in the sense that

$$(A\mathbf{v})(\mathbf{x}) = (\nabla \cdot \mathbf{F}(\mathbf{v}))(\mathbf{x}) = \sum_{d=1}^{3} \partial_d(\mathbf{B}_d(\mathbf{x})\mathbf{v}(\mathbf{x})) \quad \text{for } \mathbf{v} \in \mathcal{D}(A)$$

for a flux function $\mathbf{F}(\mathbf{v}) = (\mathbf{B}_1\mathbf{v}, \mathbf{B}_2\mathbf{v}, \mathbf{B}_3\mathbf{v})$ and symmetric matrices $\mathbf{B}_d \in W^{1,\infty}(\mathcal{B}, \mathbb{R}^{J\times J})$, $d = 1, 2, 3$. We note in particular that the matrices $\mathbf{B}_d$ are in general non-constant in space.

For the derivation of the corresponding variational formulation, we multiply with a test function $\boldsymbol{\varphi}$ and integrate over the domain $\mathcal{B}$. For given $t \in [0, T]$, defining the bilinear form

$$a\colon \mathcal{D}(A) \times \mathcal{D}(A) \to \mathbb{R}, \quad a(\mathbf{v}(t), \mathbf{w}(t)) = (A\mathbf{v}(t), \mathbf{w}(t))_{\mathcal{B}}$$

allows to state the variational formulation: Find $\mathbf{v} \in \mathcal{D}(A)$ such that

$$a(\mathbf{v}, \boldsymbol{\varphi}) = (\mathbf{b}, \boldsymbol{\varphi})_{\mathcal{B}} \quad \text{for all } \boldsymbol{\varphi} \in \mathcal{D}(A).$$

Based on the variational formulation, the problem is now transferred to a finite-dimensional setting. In a Galerkin approach, we choose a finite-dimensional space $V_h \subset L^2(\mathcal{B}, \mathbb{R}^J)$ and approximate the variational formulation by a discrete version

$$a_h(\mathbf{v}_h, \boldsymbol{\varphi}_h) = (\mathbf{b}, \boldsymbol{\varphi}_h)_{\mathcal{B}} \quad \text{for all } \boldsymbol{\varphi}_h \in V_h$$

with the approximated bilinear form $a_h\colon V_h \times V_h \to \mathbb{R}$ resulting from the approximated operator A_h. The choice of V_h is essential to obtain a reasonable approximation of the original problem.

In order to define V_h in an adequate way, we assume that the domain $\mathcal{B}$ can be decomposed into polyhedral cells. Let thus a decomposition of $\mathcal{B}$ be given by

$$\overline{\mathcal{B}} = \bigcup_{\tau \in \mathcal{T}} \overline{\tau}$$

with disjoint open and polyhedral cells $\tau \in \mathcal{T}$. The set of faces of a cell $\tau \in \mathcal{T}$ is denoted by $\mathcal{F}_\tau$ and for each cell $\tau \in \mathcal{T}$ and each face $f \in \mathcal{F}_\tau$ the neighbor cell τ_f is determined by $f = \partial\tau \cap \partial\tau_f$.

The fundamental concept of a finite element method is to approximate locally using simple functions and then assemble a global approximation based on these local approximations. For this purpose, in each cell $\tau \in \mathcal{T}$ we consider the space $\mathbb{P}_p(\tau)^J$ of polynomials of degree

less or equal $p \in \mathbb{N}_0$. For a given triangulation $\mathcal{T}$, this allows to define the global ansatz space

$$V_h = \{\boldsymbol{\varphi} \in L^2(\mathcal{B}, \mathbb{R}^J) \colon \boldsymbol{\varphi}\big|_\tau \in \mathbb{P}_p(\tau)^J \ \forall \tau \in \mathcal{T}\}.$$

By construction, it holds $V_h \not\subset \mathcal{D}(A)$. Finite element methods of this type are called *non-conforming*.

Since V_h is discontinuous, we consider a single cell $\tau \in \mathcal{T}$ for the definition of the discrete operator A_h. Multiplication with a test function $\boldsymbol{\varphi}_\tau$ in τ and integration by parts yield

$$(A\mathbf{v}, \boldsymbol{\varphi}_\tau)_\tau = -(\mathbf{F}(\mathbf{v}), \nabla \boldsymbol{\varphi}_\tau)_\tau + \sum_{f \in \mathcal{F}_\tau} (\mathbf{n}_\tau \cdot \mathbf{F}(\mathbf{v}), \boldsymbol{\varphi}_\tau)_f$$

with $\mathbf{n}_\tau$ denoting the outer normal of τ. To extend this approach to $\mathcal{B}$, continuity of the flux on the cell faces is necessary. Therefore numerical flux functions $\mathbf{F}^*_{\tau,f}$ are defined such that for neighboring cells τ and τ_f continuity on the face f is achieved, i.e. it holds

$$\mathbf{n}_\tau \cdot \mathbf{F}^*_{\tau,f}(\mathbf{v}_h) = \mathbf{n}_\tau \cdot \mathbf{F}^*_{\tau_f,f}(\mathbf{v}_h) \quad \text{for all } \mathbf{v}_h \in V_h. \tag{5.5}$$

Furthermore, the numerical flux is required to be consistent such that it corresponds in $\mathcal{D}(A)$ with the original flux, i.e.

$$\mathbf{n}_\tau \cdot \mathbf{F}^*_{\tau,f}(\mathbf{v}) = \mathbf{n}_\tau \cdot \mathbf{F}(\mathbf{v}) \quad \text{for all } \mathbf{v} \in \mathcal{D}(A). \tag{5.6}$$

Given the numerical flux, we can define the discrete operator A_h locally by

$$(A_h\mathbf{v}_h, \boldsymbol{\varphi}_{\tau,h})_\tau = -(\mathbf{F}(\mathbf{v}_h), \nabla \boldsymbol{\varphi}_{\tau,h})_\tau + \sum_{f \in \mathcal{F}_\tau} (\mathbf{n}_\tau \cdot \mathbf{F}^*_{\tau,f}(\mathbf{v}_h), \boldsymbol{\varphi}_{\tau,h})_f \quad \text{for all } \boldsymbol{\varphi}_{\tau,h} \in \mathbb{P}_p(\tau)^J$$

and for $\mathbf{v}_h \in V_h$. By construction of the numerical flux, it then holds

$$(A\mathbf{v}, \boldsymbol{\varphi}_h)_\mathcal{B} = (A_h\mathbf{v}, \boldsymbol{\varphi}_h)_\mathcal{B} \quad \text{for all } \mathbf{v} \in \mathcal{D}(A) \text{ and } \boldsymbol{\varphi}_h \in V_h.$$

This allows to approximate a solution $\mathbf{v}$ of (5.4) by $\mathbf{v}_h \in V_h$ satisfying

$$(\partial_t \mathbf{v}_h, \boldsymbol{\varphi}_h)_\mathcal{B} + \sum_{\tau \in \mathcal{T}} (A_h\mathbf{v}_h, \boldsymbol{\varphi}_h)_\tau = (\mathbf{b}, \boldsymbol{\varphi}_h)_\mathcal{B} \quad \text{for all } \boldsymbol{\varphi}_h \in V_h.$$

The adequate choice of the numerical flux $\mathbf{F}^*_{\tau,f}$ is crucial to obtain a stable numerical scheme. The simplest way to define a numerical flux which satisfies the conditions (5.5) and (5.6) is the *centered flux*. It is obtained by evaluating the flux function at the mean value

of both adjacent values. This method is, however, in general not optimal (e.g. LeVeque, 2011, Chapter 4). It is preferable to use a different approach instead. In this work, an upwind flux is used which is a choice of numerical flux that respects the motion direction of the system. The concrete selection of the numerical flux for both sub-problems will be discussed later.

The discontinuous Galerkin approach is well-established. It has been extensively studied for a variety of problems. We refer to Di Pietro and Ern (2012) and Hesthaven and Warburton (2008) for a detailed explanation of the underlying theoretical concepts including error estimates for the approximated solution. We refrain from performing a problem-specific theoretical examination of the discontinuous Galerkin discretization for the CDD system in this work.

5.3 Space discretization of the first sub-problem

Now we apply the presented space discretization scheme to the first sub-problem (5.2). Thus we aim to solve

$$\partial_t \mathbf{w} = -\nabla \cdot \mathbf{F}(\mathbf{w}) + \mathbf{G}(q)$$

where q is a given field quantity. To this end, we show that this problem fits in the general framework (5.4). We commence by defining the linear operator

$$A\colon C_\mathrm{c}^1(\mathcal{B}, \mathbb{R}\times\Gamma) \to L^2(\mathcal{B}, \mathbb{R}\times\Gamma), \quad (\rho, \boldsymbol{\kappa}) \mapsto (\nabla\cdot(v\boldsymbol{\kappa}\times\mathbf{m}), -\nabla(v\rho)\times\mathbf{m}).$$

for $v \in C^1(\mathcal{B}, \mathbb{R})$.

Remark. Since $\boldsymbol{\kappa}\colon [0,T]\times\mathcal{B} \to \Gamma$ and $\Gamma \cong \mathbb{R}^2$ one can also formulate the first sub-problem as system in $(\rho, \boldsymbol{\kappa}\cdot\mathbf{l}, \boldsymbol{\kappa}\cdot\mathbf{d})\colon [0,T]\times\mathcal{B} \to \mathbb{R}^3$ instead of $\mathbf{w} = (\rho, \boldsymbol{\kappa})\colon [0,T]\times\mathcal{B} \to \mathbb{R}\times\Gamma \subset \mathbb{R}\times\mathbb{R}^3$. Thus this problem corresponds to $J = 3$ in the general setting. Here, we prefer the formulation using $\mathbf{w} = (\rho, \boldsymbol{\kappa})$ because it allows for a more compact notation.

In order to define the domain $\mathcal{D}(A)$ of A, we first derive the Hilbert adjoint operator A^* to A. For $(\rho, \boldsymbol{\kappa}) \in C_\mathrm{c}^1(\mathcal{B}, \mathbb{R}\times\Gamma)$ and a test function $(\varphi, \boldsymbol{\varphi}) \in C_\mathrm{c}^1(\mathcal{B}, \mathbb{R}\times\Gamma)$, we obtain using integration by parts

$$\begin{aligned}
\big(A(\rho, \boldsymbol{\kappa}), (\varphi, \boldsymbol{\varphi})\big)_\mathcal{B} &= \int_\mathcal{B} \varphi\nabla\cdot(v\boldsymbol{\kappa}\times\mathbf{m}) - \boldsymbol{\varphi}\cdot(\nabla(v\rho)\times\mathbf{m})\,\mathrm{d}\mathbf{x} \\
&= \int_\mathcal{B} -\nabla\varphi\cdot(v\boldsymbol{\kappa}\times\mathbf{m}) - (\nabla\times\boldsymbol{\varphi})\cdot(v\rho\mathbf{m})\,\mathrm{d}\mathbf{x} \\
&= \big((\rho, \boldsymbol{\kappa}), A^*(\varphi, \boldsymbol{\varphi})\big)_\mathcal{B}.
\end{aligned}$$

Hence, the adjoint operator A^* to A is given by

$$A^*\colon C_c^1(\mathcal{B}, \mathbb{R}\times\Gamma) \to L^2(\mathcal{B}, \mathbb{R}\times\Gamma), \quad (\varphi, \boldsymbol{\varphi}) \mapsto (-v(\nabla\times\boldsymbol{\varphi})\cdot\mathbf{m}, v\nabla\varphi\times\mathbf{m}).$$

Knowing the adjoint operator A^*, allows to define the space of with respect to A weakly differentiable functions

$$H(A,\mathcal{B}) = \{\mathbf{x}\in L^2(\mathcal{B},\mathbb{R}\times\Gamma)\colon \exists \mathbf{y}\in L^2(\mathcal{B},\mathbb{R}\times\Gamma)\ (\mathbf{y},\mathbf{z})_{\mathcal{B}} = (\mathbf{x}, A^*\mathbf{z})_{\mathcal{B}}\ \forall \mathbf{z}\in C_c^1(\mathcal{B},\mathbb{R}\times\Gamma)\}.$$

$H(A,\mathcal{B})$ is a Hilbert space with respect to the graph norm $\|\cdot\|_A = \sqrt{\|\cdot\|^2 + \|A\cdot\|^2}$ (or more precisely the corresponding inner product). The operator A can be extended in a straightforward way to $H(A,\mathcal{B})$. Since

$$C_c^1(\mathcal{B},\mathbb{R}\times\Gamma) \subset H(A,\mathcal{B}) \subset L^2(\mathcal{B},\mathbb{R}\times\Gamma)$$

the Hilbert space $H(A,\mathcal{B})$ is dense in $L^2(\mathcal{B},\mathbb{R}\times\Gamma)$. Dependent on the boundary condition, the domain of A is chosen densely such that $\mathcal{D}(A)\subset H(A,\mathcal{B})$. Then the first sub-problem fits in the abstract framework and we can hence proceed by stating the corresponding space discretization.

Remark. Given the extension of A to $H(A,\mathcal{B})$, the regularity of the dislocation density v can be lowered. It is sufficient to require $v\in L^\infty(\mathcal{B},\mathbb{R})$.

5.3.1 Discrete operator

In a cell $\tau\in\mathcal{T}$ the polynomial ansatz space

$$V_h(\tau) = \{(\varphi,\boldsymbol{\varphi})\colon \tau\to\mathbb{R}\times\Gamma\colon \varphi, \boldsymbol{\varphi}\cdot\mathbf{d}, \boldsymbol{\varphi}\cdot\mathbf{l}\in\mathbb{P}_p(\tau)\}$$

is considered. For a given mesh $\mathcal{T}$ of $\mathcal{B}$ the discontinuous Galerkin operator A_h for the first sub-problem (5.2) can be derived following the strategy for the general framework. It is given by

$$(A_h\mathbf{w}_h, \boldsymbol{\varphi}_{\tau,h})_\tau = -(\mathbf{F}(\mathbf{w}_h), \nabla\boldsymbol{\varphi}_{\tau,h})_\tau + \sum_{f\in\mathcal{F}_\tau}(\mathbf{n}_\tau\cdot\mathbf{F}^*_{\tau,f}(\mathbf{w}_h), \boldsymbol{\varphi}_{\tau,h})_f \quad \text{for all } \boldsymbol{\varphi}_{\tau,h}\in V_h(\tau)$$

for $\mathbf{w}_h\in V_h(\tau)$ and outer normal $\mathbf{n}_\tau$ on τ. Thus a solution $\mathbf{w}$ of the first sub-problem (5.2) is approximated by $\mathbf{w}_h\in V_h$ fulfilling

$$(\partial_t\mathbf{w}_h, \boldsymbol{\varphi}_h)_{\mathcal{B}} + \sum_{\tau\in\mathcal{T}}(A_h\mathbf{w}_h, \boldsymbol{\varphi}_h)_\tau = (\mathbf{G}(q), \boldsymbol{\varphi}_h)_{\mathcal{B}} \quad \text{for all } \boldsymbol{\varphi}_h\in V_h$$

with V_h denoting the discontinuous Galerkin ansatz space

$$V_h = \{\boldsymbol{\varphi}_h \in L^2(\mathcal{B}, \mathbb{R} \times \Gamma) \colon \boldsymbol{\varphi}_h\big|_\tau \in V_h(\tau)\ \forall \tau \in \mathcal{T}\}.$$

In order to complete the space discretization for the first sub-problem, it remains to compute the upwind flux $\mathbf{F}^*_{\tau,f}$ for $\tau \in \mathcal{T}$ and $f \in \mathcal{F}_\tau$.

5.3.2 Upwind flux on inner faces

The computation of the upwind flux can be related to the solution of an initial value problem. We refer to LeVeque (2011) for an extensive investigation of upwind fluxes for different problems. Here, we roughly follow the derivation of the upwind flux for Maxwell's equations by Schulz (2015).

We start by considering the first sub-problem without the right-hand side $\mathbf{g}$ in the time-space cylinder $\mathcal{B}_t = (0, \infty) \times \mathbb{R}^3$, i.e.

$$\partial_t \mathbf{w} = -\nabla \cdot \mathbf{F}(\mathbf{w}) \qquad \text{in } \mathcal{B}_t,$$

with piecewise constant initial values

$$\mathbf{w}(0, \mathbf{x}) = \begin{cases} \mathbf{w}^- & \mathbf{x} \cdot \mathbf{n} < 0 \\ \mathbf{w}^+ & \mathbf{x} \cdot \mathbf{n} > 0 \end{cases}$$

for a unit vector $\mathbf{n} \in \mathbb{R}^3$. Such an initial value problem with piecewise constant initial values is called *Riemann problem*.

Integration by parts in $\mathcal{B}_t$ yields the corresponding weak formulation

$$(\mathbf{w}, \partial_t \boldsymbol{\varphi})_{\mathcal{B}_t} + (\mathbf{F}(\mathbf{w}), \nabla \boldsymbol{\varphi})_{\mathcal{B}_t} = -(\mathbf{w}(0, \cdot), \boldsymbol{\varphi}(0, \cdot))_{\mathbb{R}^3} \tag{5.7}$$

for all test functions $\boldsymbol{\varphi} \in C^1_c([0, \infty) \times \mathbb{R}^3, \mathbb{R} \times \Gamma)$. Subsequently, we construct a solution $\mathbf{w}$ of (5.7). We will see that it takes the form

$$\mathbf{w}(t, \mathbf{x}) = \begin{cases} \mathbf{w}^- & \mathbf{x} \cdot \mathbf{n} < -c_1 t \\ \mathbf{w}^1 & -c_1 t < \mathbf{x} \cdot \mathbf{n} < 0 \\ \mathbf{w}^2 & 0 < \mathbf{x} \cdot \mathbf{n} < c_2 t \\ \mathbf{w}^+ & c_2 t < \mathbf{x} \cdot \mathbf{n} \end{cases} \tag{5.8}$$

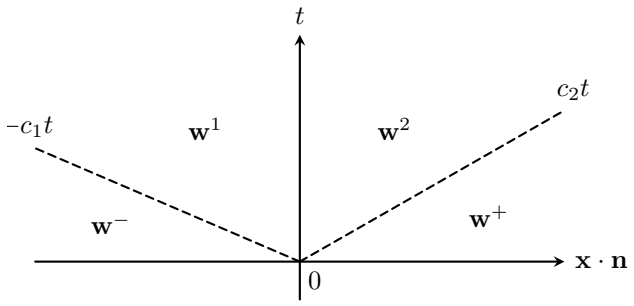

Figure 5.1: Illustration of a Riemann solution with discontinuity in the initial data at $\mathbf{x}\cdot\mathbf{n}=0$ traveling in three directions

where $\mathbf{w}^1, \mathbf{w}^2 \in \mathbb{R}\times\Gamma$ need to fulfill the Rankine-Hugoniot jump conditions

$$\mathbf{n}\cdot\mathbf{F}(\mathbf{w}^1-\mathbf{w}^-) = -c_1(\mathbf{w}^1-\mathbf{w}^-) \tag{5.9a}$$

$$\mathbf{n}\cdot\mathbf{F}(\mathbf{w}^2-\mathbf{w}^1) = \mathbf{0} \tag{5.9b}$$

$$\mathbf{n}\cdot\mathbf{F}(\mathbf{w}^+-\mathbf{w}^2) = c_2(\mathbf{w}^+-\mathbf{w}^2). \tag{5.9c}$$

for $c_1, c_2 > 0$. Thus the solution is piecewise constant and the discontinuity in the initial data moves through the time-space cylinder in three directions, see Figure 5.1.

This allows to define the upwind flux $\mathbf{F}^*_{\tau,f}(\mathbf{w}_h(t,\mathbf{x}))$ on an inner face $f\in\mathcal{F}_\tau$ of a cell $\tau\in\mathcal{T}$ via the following consideration: If we identify the discontinuity in the Riemann problem $\mathbf{x}\cdot\mathbf{n}=0$ with the discontinuity on f by choosing the unit normal $\mathbf{n}=\mathbf{n}_\tau$ as well as the initial values

$$\mathbf{w}^- = \mathbf{w}_h\big|_\tau(t,\mathbf{x}) \qquad \text{and} \qquad \mathbf{w}^+ = \mathbf{w}_h\big|_{\tau_f}(t,\mathbf{x})$$

for $\mathbf{x}\in f$, the Riemann problem corresponds to the local situation in a small environment of $\mathbf{x}$ at time t. With $\mathbf{w}$ denoting a weak solution of the Riemann problem, the upwind flux in $\mathbf{x}$ is given by

$$\mathbf{n}_\tau\cdot\mathbf{F}^*_{\tau,f}(\mathbf{w}_h(t,\mathbf{x})) = \mathbf{n}\cdot\mathbf{F}(\mathbf{w}(t,\mathbf{x}))$$

which is well-defined if the jump condition (5.9b) is fulfilled.

We start by showing that $\mathbf{w}$ of the form (5.8) satisfying the jump conditions (5.9) is indeed a weak solution of the Riemann problem. Afterwards $\mathbf{w}^1, \mathbf{w}^2$ and c_1, c_2 will be constructed such that the jump conditions (5.9) hold.

Let now $c_1, c_2 > 0$ and $\mathbf{w}^1, \mathbf{w}^2 \in \mathbb{R}\times\Gamma$ be given such that the jump conditions are fulfilled. We insert the corresponding $\mathbf{w}$ given by (5.8) into the left-hand side of the weak

formulation (5.7). In order to take advantage of the piecewise constant structure of $\mathbf{w}$, we decompose the time-space cylinder $\mathcal{B}_t$ in consideration of the discontinuities of the ansatz for the Riemann solution (5.8) into

$$\begin{aligned}
\mathcal{B}_t^0 &= \{(t,\mathbf{x}) \in \mathcal{B}_t \colon \mathbf{x}\cdot\mathbf{n} < -c_1 t\},\\
\mathcal{B}_t^1 &= \{(t,\mathbf{x}) \in \mathcal{B}_t \colon -c_1 t < \mathbf{x}\cdot\mathbf{n} < 0\},\\
\mathcal{B}_t^2 &= \{(t,\mathbf{x}) \in \mathcal{B}_t \colon 0 < \mathbf{x}\cdot\mathbf{n} < c_2 t\},\\
\mathcal{B}_t^3 &= \{(t,\mathbf{x}) \in \mathcal{B}_t \colon c_2 t < \mathbf{x}\cdot\mathbf{n}\}.
\end{aligned}$$

With $\widetilde{\nabla} = (\partial_t, \nabla)$ denoting the time-space gradient, we then can split the left-hand side of the weak formulation (5.7). We therefore write

$$(\mathbf{w}, \partial_t \boldsymbol{\varphi})_{\mathcal{B}_t} + (\mathbf{F}(\mathbf{w}), \nabla\boldsymbol{\varphi})_{\mathcal{B}_t} = \sum_{k=0}^{3} \int_{\mathcal{B}_t^k} (\mathbf{w}, \mathbf{F}(\mathbf{w})) \cdot \widetilde{\nabla}\boldsymbol{\varphi} \,\mathrm{d}(t,\mathbf{x}) \tag{5.10}$$

for test functions $\boldsymbol{\varphi} \in C_c^1([0,\infty)\times\mathbb{R}^3, \mathbb{R}\times\Gamma)$. This motivates to investigate the weak formulation in each $\mathcal{B}_t^k$ separately. Exploiting that $\mathbf{w}$ is constant in $\mathcal{B}_t^k$, $k = 0,1,2,3$, integration by parts yields

$$\begin{aligned}
\int_{\mathcal{B}_t^k} (\mathbf{w}, \mathbf{F}(\mathbf{w})) \cdot \widetilde{\nabla}\boldsymbol{\varphi} \,\mathrm{d}(t,\mathbf{x}) &= -\int_{\mathcal{B}_t^k} (\widetilde{\nabla} \cdot (\mathbf{w}, \mathbf{F}(\mathbf{w}))) \cdot \boldsymbol{\varphi} \,\mathrm{d}(t,\mathbf{x}) + \int_{\partial\mathcal{B}_t^k} (\mathbf{w}, \mathbf{F}(\mathbf{w}))\mathbf{n}^k \cdot \boldsymbol{\varphi} \,\mathrm{d}\mathbf{a}\\
&= \int_{\partial\mathcal{B}_t^k} (\mathbf{w}, \mathbf{F}(\mathbf{w}))\mathbf{n}^k \cdot \boldsymbol{\varphi} \,\mathrm{d}\mathbf{a}
\end{aligned}$$

for $k = 0,1,2,3$ with $\mathbf{n}^k$ denoting the outer unit normal on $\mathcal{B}_t^k$. The skeleton $\bigcup_k \partial\mathcal{B}_t^k$ can be decomposed into

$$\bigcup_{k=0}^{3} \partial\mathcal{B}_t^k = \Gamma^0 \cup \Gamma^{0,1} \cup \Gamma^{1,2} \cup \Gamma^{2,3} \cup \Gamma^3$$

given by

$$\begin{aligned}
\Gamma^0 &= (\{0\}\times\mathbb{R}^3) \cap \partial\mathcal{B}_t^0 = \{(0,\mathbf{x}) \in \mathcal{B}_t \colon \mathbf{x}\cdot\mathbf{n} < 0\},\\
\Gamma^{0,1} &= \partial\mathcal{B}_t^0 \cap \partial\mathcal{B}_t^1 = \{(t,\mathbf{x}) \in \mathcal{B}_t \colon \mathbf{x}\cdot\mathbf{n} = -c_1 t\},\\
\Gamma^{1,2} &= \partial\mathcal{B}_t^1 \cap \partial\mathcal{B}_t^2 = \{(t,\mathbf{x}) \in \mathcal{B}_t \colon \mathbf{x}\cdot\mathbf{n} = 0\},\\
\Gamma^{2,3} &= \partial\mathcal{B}_t^2 \cap \partial\mathcal{B}_t^3 = \{(t,\mathbf{x}) \in \mathcal{B}_t \colon \mathbf{x}\cdot\mathbf{n} = c_2 t\},\\
\Gamma^3 &= \partial\mathcal{B}_t^3 \cap (\{0\}\times\mathbb{R}^3) = \{(0,\mathbf{x}) \in \mathcal{B}_t \colon \mathbf{x}\cdot\mathbf{n} > 0\}.
\end{aligned}$$

This allows to calculate the unit normals $\mathbf{n}^k$, $k = 0, 1, 2, 3$. We obtain

$$\begin{aligned}
\mathbf{n}^0|_{\Gamma^0} &= \begin{pmatrix} -1 \\ \mathbf{0} \end{pmatrix}, & \mathbf{n}^0|_{\Gamma^{0,1}} &= \frac{1}{\sqrt{c_1^2+1}} \begin{pmatrix} c_1 \\ \mathbf{n} \end{pmatrix}, \\
\mathbf{n}^1|_{\Gamma^{0,1}} &= \frac{1}{\sqrt{c_1^2+1}} \begin{pmatrix} -c_1 \\ -\mathbf{n} \end{pmatrix}, & \mathbf{n}^1|_{\Gamma^{1,2}} &= \begin{pmatrix} 0 \\ \mathbf{n} \end{pmatrix}, \\
\mathbf{n}^2|_{\Gamma^{1,2}} &= \begin{pmatrix} 0 \\ -\mathbf{n} \end{pmatrix}, & \mathbf{n}^2|_{\Gamma^{2,3}} &= \frac{1}{\sqrt{c_2^2+1}} \begin{pmatrix} -c_2 \\ \mathbf{n} \end{pmatrix}, \\
\mathbf{n}^3|_{\Gamma^{2,3}} &= \frac{1}{\sqrt{c_2^2+1}} \begin{pmatrix} c_2 \\ -\mathbf{n} \end{pmatrix}, & \mathbf{n}^3|_{\Gamma^3} &= \begin{pmatrix} -1 \\ \mathbf{0} \end{pmatrix}.
\end{aligned}$$

Inserting into (5.10) yields

$$\begin{aligned}
(\mathbf{w}, \partial_t \boldsymbol{\varphi})_{\mathcal{B}_t} + (\mathbf{F}(\mathbf{w}), \nabla \boldsymbol{\varphi})_{\mathcal{B}_t} = &\int_{\Gamma^0} -\mathbf{w}^- \cdot \boldsymbol{\varphi} \, \mathrm{d}\mathbf{a} \\
&+ \frac{1}{\sqrt{c_1^2+1}} \int_{\Gamma^{0,1}} (c_1(\mathbf{w}^- - \mathbf{w}^1) + \mathbf{n} \cdot \mathbf{F}(\mathbf{w}^- - \mathbf{w}^1)) \cdot \boldsymbol{\varphi} \, \mathrm{d}\mathbf{a} \\
&+ \int_{\Gamma^{1,2}} (\mathbf{n} \cdot \mathbf{F}(\mathbf{w}^1 - \mathbf{w}^2)) \cdot \boldsymbol{\varphi} \, \mathrm{d}\mathbf{a} \\
&- \frac{1}{\sqrt{c_2^2+1}} \int_{\Gamma^{2,3}} (c_2(\mathbf{w}^2 - \mathbf{w}^+) - \mathbf{n} \cdot \mathbf{F}(\mathbf{w}^2 - \mathbf{w}^+)) \cdot \boldsymbol{\varphi} \, \mathrm{d}\mathbf{a} \\
&+ \int_{\Gamma^3} -\mathbf{w}^+ \cdot \boldsymbol{\varphi} \, \mathrm{d}\mathbf{a}.
\end{aligned}$$

If the Rankine-Hugoniot conditions (5.9) are fulfilled, this simplifies to

$$\begin{aligned}
(\mathbf{w}, \partial_t \boldsymbol{\varphi})_{\mathcal{B}_t} + (\mathbf{F}(\mathbf{w}), \nabla \boldsymbol{\varphi})_{\mathcal{B}_t} &= \int_{\Gamma^0} -\mathbf{w}^- \cdot \boldsymbol{\varphi} \, \mathrm{d}\mathbf{a} + \int_{\Gamma^3} -\mathbf{w}^+ \cdot \boldsymbol{\varphi} \, \mathrm{d}\mathbf{a} \\
&= -(\mathbf{w}(0, \cdot), \boldsymbol{\varphi})_{\mathbb{R}^3}.
\end{aligned}$$

Hence, $\mathbf{w}$ in fact satisfies the weak formulation (5.7).

It remains to find c_1, c_2 and $\mathbf{w}^1, \mathbf{w}^2$ such that the jump conditions (5.9) are fulfilled. For this purpose, we need to solve the eigenvalue problem of the flux matrix

$$\mathbf{B}_\mathbf{n} = \begin{pmatrix} 0 & v(\mathbf{m} \times \mathbf{n})^\top \\ v\mathbf{m} \times \mathbf{n} & \mathbf{0} \end{pmatrix} \in L^\infty(\mathcal{B}, \mathbb{R}^{4\times 4}) \tag{5.11}$$

which is defined such that

$$\mathbf{n}\cdot\mathbf{F}(\mathbf{w}) = \mathbf{B}_\mathbf{n}\begin{pmatrix}\rho\\ \boldsymbol{\kappa}\end{pmatrix} = \begin{pmatrix}\mathbf{n}\cdot(v\boldsymbol{\kappa}\times\mathbf{m})\\ -\mathbf{n}\times(v\rho\mathbf{m})\end{pmatrix} = v\begin{pmatrix}\boldsymbol{\kappa}\cdot(\mathbf{m}\times\mathbf{n})\\ \rho\mathbf{m}\times\mathbf{n}\end{pmatrix}.$$

The flux matrix is symmetric and thus diagonalizable. The eigenvalues of $\mathbf{B}_\mathbf{n}$ are 0 and $\pm c$ with $c = |v\mathbf{m}\times\mathbf{n}|$. We assume $c \neq 0$ in the following because the flux $\mathbf{n}\cdot\mathbf{F}(\mathbf{w})$ vanishes otherwise. Then

$$\mathbf{v}^0 = \begin{pmatrix}0\\ \mathbf{n}\end{pmatrix}, \quad \mathbf{v}^{0,2} = \begin{pmatrix}0\\ \mathbf{m}\end{pmatrix} \qquad \text{and} \qquad \mathbf{v}^\pm = \begin{pmatrix}\pm c\\ v\mathbf{m}\times\mathbf{n}\end{pmatrix}$$

are the corresponding orthogonal eigenvectors.

Remark. If the problem is formulated for $(\rho, \boldsymbol{\kappa}\cdot\mathbf{l}, \boldsymbol{\kappa}\cdot\mathbf{d})\colon [0,T]\times\mathcal{B}\to\mathbb{R}^3$ instead of $\mathbf{w} = (\rho,\boldsymbol{\kappa})\colon [0,T]\times\mathcal{B}\to\mathbb{R}\times\Gamma$ as mentioned previously, then the corresponding flux matrix has values in $\mathbb{R}^{3\times3}$. The eigenvector $\mathbf{v}^{0,2}$ is a consequence of the chosen notation and reflects that no flux perpendicular to the slip plane is possible. For fixed v, the vectors $\mathbf{v}^0$ and $\mathbf{v}^\pm$ are an orthogonal basis of $\mathbb{R}\times\Gamma$ and can be transferred in a straightforward way to an orthogonal basis of $\mathbb{R}^3$ consisting of eigenvectors of the flux matrix in $\mathbb{R}^{3\times3}$.

In general, we have different dislocation velocities v_1 and v_2 for $\mathbf{x}\cdot\mathbf{n} < 0$ and $\mathbf{x}\cdot\mathbf{n} > 0$. The corresponding eigenvalues and eigenvectors are indicated in the following by a lower index 1 and 2, respectively.

For the jump conditions (5.9) to be fulfilled, we need to find coefficients $\zeta,\eta,\xi\in\mathbb{R}$ such that

$$\mathbf{w}^1 - \mathbf{w}^- = \zeta\,\mathbf{v}_1^- \tag{5.12a}$$
$$\mathbf{w}^2 - \mathbf{w}^1 = \eta\,\mathbf{v}^0 \tag{5.12b}$$
$$\mathbf{w}^+ - \mathbf{w}^2 = \xi\,\mathbf{v}_2^+. \tag{5.12c}$$

Inserting Equations (5.12a) and (5.12c) into (5.12b) yields

$$\mathbf{w}^+ - \xi\,\mathbf{v}_2^+ - \mathbf{w}^- - \zeta\,\mathbf{v}_1^- = \eta\,\mathbf{v}^0. \tag{5.13}$$

The eigenvector $\mathbf{v}_2^+$ can be expressed in terms of $\mathbf{v}_1^\pm$ via

$$\mathbf{v}_2^+ = \left(\frac{v_2}{2v_1} + \frac{|v_2|}{2|v_1|}\right)\mathbf{v}_1^+ + \left(\frac{v_2}{2v_1} - \frac{|v_2|}{2|v_1|}\right)\mathbf{v}_1^-.$$

Therefore, Equation (5.13) is equivalent to

$$\mathbf{w}^+ - \mathbf{w}^- - \xi\left(\frac{v_2}{2v_1} + \frac{|v_2|}{2|v_1|}\right)\mathbf{v}_2^+ - \xi\left(\left(\frac{v_2}{2v_1} - \frac{|v_2|}{2|v_1|}\right) + \zeta\right)\mathbf{v}_1^- = \eta\mathbf{v}^0.$$

Equating the coefficients, three scalar equations

$$0 = (\mathbf{w}^+ - \mathbf{w}^-)\cdot\mathbf{v}_1^+ - 2c_1^2\xi\left(\frac{v_2}{2v_1} + \frac{|v_2|}{2|v_1|}\right) \tag{5.14a}$$

$$2\eta = (\mathbf{w}^+ - \mathbf{w}^-)\cdot\mathbf{v}_1^0 \tag{5.14b}$$

$$0 = (\mathbf{w}^+ - \mathbf{w}^-)\cdot\mathbf{v}_1^- - 2c_1^2\xi\left(\left(\frac{v_2}{2v_1} - \frac{|v_2|}{2|v_1|}\right) + \zeta\right) \tag{5.14c}$$

are obtained. We observe that if $\operatorname{sgn}(v_1) \neq \operatorname{sgn}(v_2)$ the first equation (5.14a) does in general not allow for a solution. If $\operatorname{sgn}(v_1) = \operatorname{sgn}(v_2)$ we obtain

$$\zeta = \frac{(\mathbf{w}^+ - \mathbf{w}^-)\cdot\mathbf{v}_1^-}{2c_1^2}$$

$$\xi = \frac{v_1}{v_2}\frac{(\mathbf{w}^+ - \mathbf{w}^-)\cdot\mathbf{v}_1^+}{2c_1^2} = \frac{(\mathbf{w}^+ - \mathbf{w}^-)\cdot\mathbf{v}_2^+}{2c_2^2}.$$

The observation that for different signs of the velocity in two neighboring cells no upwind flux can be defined on the common face, seems reasonable. It reflects that in this case no clear direction of motion can be identified. Thus the fundamental idea underlying the upwind flux is violated. In this case, for example the centered flux could be used.

We solve this problem in a different way: Knowing that the velocity is based on a constitutive equation which takes into account the local stress field, it is likely that it is correlated in some way in a small environment. For this reason, we approximate the – a priori discontinuous – dislocation velocity by computing a smooth counterpart.

For this purpose, we denote by v_h the dislocation velocity in $\mathcal{B}$ which is computed by evaluation of a velocity law based on physical quantities – as e.g. the macroscopic stress – which are approximated in a finite-dimensional setting based on a space grid of mesh width h. Then we compute an averaged velocity $\bar{v}_h$ in a continuous finite element space. More details on how to evaluate the velocity law will follow in Chapter 6. For now, it is sufficient to assume having a continuous averaged dislocation velocity $\bar{v}_h$.

Remark. For the sake of consistency, it is reasonable to use the averaged velocity $\bar{v}_h$ not only for the definition of the upwind flux on cell faces but also for the evaluation of the flux in the inner of a cell $\tau \in \mathcal{T}$. This is what we actually do when evaluating the discrete problem presented in Section 5.3.1.

Equipped with a continuous dislocation velocity, the distinction of v_1 and v_2 is dispensable. Then the Riemann solution is obtained by setting

$$\zeta = \frac{(\mathbf{w}^+ - \mathbf{w}^-)\cdot \mathbf{v}^-}{2c^2} \qquad \text{and} \qquad \xi = \frac{(\mathbf{w}^+ - \mathbf{w}^-)\cdot \mathbf{v}^+}{2c^2}. \tag{5.15}$$

Thus finally we can define the upwind flux on an inner face $f \in \mathcal{F}_\tau$ as

$$\begin{aligned}
\mathbf{n}_\tau \cdot \mathbf{F}^*_{\tau,f}(\mathbf{w}_h) &= \mathbf{n}_\tau \cdot \mathbf{F}(\mathbf{w}_h\big|_\tau + \zeta \mathbf{v}^-) \\
&= \mathbf{n}_\tau \cdot \mathbf{F}(\mathbf{w}_h\big|_\tau) - |\bar{v}_h \mathbf{m}\times\mathbf{n}_\tau| \zeta \begin{pmatrix} -|\bar{v}_h \mathbf{m}\times\mathbf{n}_\tau| \\ \bar{v}_h \mathbf{m}\times\mathbf{n}_\tau \end{pmatrix} \\
&= \mathbf{n}_\tau \cdot \mathbf{F}(\mathbf{w}_h\big|_\tau) - \frac{\bar{v}_h [\boldsymbol{\kappa}_h]\cdot(\mathbf{m}\times\mathbf{n}_\tau) - |\bar{v}_h \mathbf{m}\times\mathbf{n}_\tau|[\rho_h]}{2|\bar{v}_h \mathbf{m}\times\mathbf{n}_\tau|} \begin{pmatrix} -|\bar{v}_h \mathbf{m}\times\mathbf{n}_\tau| \\ \bar{v}_h \mathbf{m}\times\mathbf{n}_\tau \end{pmatrix}
\end{aligned}$$

with $[\,\cdot\,]$ denoting the jump at f given by $[\boldsymbol{\kappa}_h] = \boldsymbol{\kappa}_h\big|_{\tau_f} - \boldsymbol{\kappa}_h\big|_\tau$ and $[\rho_h] = \rho_h\big|_{\tau_f} - \rho_h\big|_\tau$.

5.3.3 Upwind flux on boundary faces

In application, usually bounded geometries $\mathcal{B}$ are of interest. For this reason, in addition to the numerical flux on inner cell interfaces, an appropriate choice of it on boundary faces is required. We note that each choice of numerical flux on the boundary $\partial\mathcal{B}$ implicitly defines a boundary condition. Hence, before discussing a possible choice of the numerical flux, we first need do investigate what kind of boundary conditions are required for the CDD system.

There are basically two physically relevant ways of how a dislocation behaves when facing a boundary. On free surfaces, dislocations are expected to exit the volume and leave a step in the surface. Moreover, a boundary can act as an obstacle impossible to pass for a dislocation. For example, Dirichlet boundaries of the macroscopic problem are usually assumed to limit dislocation motion. We call this case an impenetrable boundary.

For both situations, we need to formulate a corresponding boundary condition for the CDD system. To this end, the physically expected behavior needs to be transferred to conditions for the CDD variables ρ, $\boldsymbol{\kappa}$ and q.

While on a free surface, all CDD quantities are expected to leave the volume in a similar way, the situation on an impenetrable boundary is less clear. An impenetrable boundary condition needs to restrain the dislocation density ρ from passing a surface. Similarly, the motion of the GND density $|\boldsymbol{\kappa}|$ is restricted. If this surface is a straight plane, the curvature density q of the dislocations located directly at the boundary is however supposed to vanish.

The definition of an impenetrable boundary condition is of particular importance because grain boundaries can be understood as such. In this work, we assume that dislocations cannot pass a grain boundary and that the shape of a grain boundary remains the same regardless of the load and the dislocation motion. Actually, grain boundaries are no boundaries of the geometry in the proper sense since they lie inside the volume. However, they are boundaries of the respective single crystalline grains and can be realized in a very similar way.

Robin-type boundary conditions

Before addressing the specific boundary conditions for the first sub-problem which are interesting in applications, a rather general boundary condition of Robin-type is considered. On the boundary

$$\partial\mathcal{B} = \{\mathbf{x} \in \mathbb{R}^3 \colon \mathbf{x} \cdot \mathbf{n} = 0\}$$

of the half space

$$\mathcal{B} = \{\mathbf{x} \in \mathbb{R}^3 \colon \mathbf{x} \cdot \mathbf{n} < 0\}$$

determined by a unit vector $\mathbf{n} \in \mathbb{R}^3$, the boundary condition

$$\vartheta |v\mathbf{m} \times \mathbf{n}| \, \rho(t, \mathbf{x}) + \delta v \mathbf{n} \cdot (\boldsymbol{\kappa}(t, \mathbf{x}) \times \mathbf{m}) = \omega \qquad \text{for } \mathbf{x} \in \partial\mathcal{B} \tag{5.16}$$

for parameters $\vartheta, \delta, \omega \in \mathbb{R}$ with $\vartheta \neq \delta$ is considered.

The Riemann solutions computed in the previous section are helpful for the definition of the numerical flux on boundary faces. For this reason, we calculate the solution in the half-space $\mathcal{B}$ with initial condition $\mathbf{w}(0, \mathbf{x}) = \mathbf{w}^-$ for $\mathbf{x} \cdot \mathbf{n} < 0$. Following the considerations of Section 5.3.2, we assume

$$\mathbf{w}(t, \mathbf{x}) = \mathbf{w}^- + \zeta \mathbf{v}^- \quad \text{for } -ct < \mathbf{x} \cdot \mathbf{n} < 0 \tag{5.17}$$

for some $\zeta \in \mathbb{R}$ and $c = |v\mathbf{m} \times \mathbf{n}|$. Inserting Equation (5.17) into the boundary condition (5.16) yields

$$\zeta = \frac{\omega - \vartheta |v\mathbf{m} \times \mathbf{n}| \rho^- - \delta v \mathbf{n} \cdot (\boldsymbol{\kappa}^- \times \mathbf{m})}{(\vartheta - \delta) |v\mathbf{m} \times \mathbf{n}|^2}. \tag{5.18}$$

Hence we can define the upwind flux on a Robin-type boundary face $f \in \mathcal{F}_\tau \cap \partial\mathcal{B}$ by

$$\begin{aligned}\mathbf{n}_\tau \cdot \mathbf{F}^*_{\tau,f}(\mathbf{w}_h) &= \mathbf{n}_\tau \cdot \mathbf{F}(\mathbf{w}_h\big|_\tau) - |\bar{v}_h \mathbf{m}\times\mathbf{n}_\tau|\zeta \begin{pmatrix} -|\bar{v}_h\mathbf{m}\times\mathbf{n}_\tau| \\ \bar{v}_h\mathbf{m}\times\mathbf{n}_\tau \end{pmatrix} \\ &= \mathbf{n}_\tau \cdot \mathbf{F}(\mathbf{w}_h\big|_\tau) - \frac{\omega - \vartheta|\bar{v}_h\mathbf{m}\times\mathbf{n}_\tau|\rho_h\big|_\tau - \delta\bar{v}_h\mathbf{n}_\tau\cdot(\boldsymbol{\kappa}_h\big|_\tau\times\mathbf{m})}{(\vartheta-\delta)|\bar{v}_h\mathbf{m}\times\mathbf{n}_\tau|} \begin{pmatrix} -|\bar{v}_h\mathbf{m}\times\mathbf{n}_\tau| \\ \bar{v}_h\mathbf{m}\times\mathbf{n}_\tau \end{pmatrix}.\end{aligned}$$

This general formulation serves as a basis for the definition of the numerical flux corresponding to the required boundary conditions.

Free outflow boundary

A free outflow boundary condition needs to represent dislocations leaving the volume without any reflections. In order to understand how this behavior can be formulated in terms of a boundary condition of Robin-type as in Equation (5.16), it is helpful to match this situation in a Riemann problem setting.

The situation of dislocation density crossing a free outflow boundary can be thought of as regarding the considered volume as part of a larger one with the same properties. Then the boundary faces can be identified with inner cell interfaces of the enlarged volume. For such inner faces, we have already derived the upwind flux in the previous section. It seems natural to define the numerical flux on a free outflow boundary in exactly the same way. To this end, we consider a Riemann problem with $\mathbf{w}(0,\mathbf{x}) = \mathbf{w}^-$ for $\mathbf{x}\cdot\mathbf{n} < 0$ representing the inner value and prescribe $\mathbf{w}^+ = \mathbf{0}$ for $\mathbf{x}\cdot\mathbf{n} > 0$. Then the Riemann solution is

$$\mathbf{w} = \mathbf{w}^- + \zeta\mathbf{v}^- \qquad \text{with} \qquad \zeta = \frac{-v\boldsymbol{\kappa}^-\cdot(\mathbf{m}\times\mathbf{n}) + c\rho^-}{2c^2},$$

according to the considerations of Section 5.3.2. By direct comparison with (5.18), we see that this is equivalent to the boundary condition

$$-|v\,\mathbf{m}\times\mathbf{n}|\rho + v\,\mathbf{n}\cdot(\boldsymbol{\kappa}\times\mathbf{m}) = 0. \tag{5.19}$$

Thus a free outflow boundary is in fact a Robin-type boundary condition as in (5.16) with $\vartheta = -1$, $\delta = 1$ and $\omega = 0$. The corresponding upwind flux on a boundary face $f \in \mathcal{F}_\tau$ is therefore given by

$$\begin{aligned}\mathbf{n}_\tau \cdot \mathbf{F}^*_{\tau,f}(\mathbf{w}_h) &= \mathbf{n}_\tau \cdot \mathbf{F}(\mathbf{w}_h\big|_\tau) - |\bar{v}_h \mathbf{m}\times\mathbf{n}_\tau|\zeta \begin{pmatrix} -|\bar{v}_h\mathbf{m}\times\mathbf{n}_\tau| \\ \bar{v}_h\mathbf{m}\times\mathbf{n}_\tau \end{pmatrix} \\ &= \mathbf{n}_\tau \cdot \mathbf{F}(\mathbf{w}_h\big|_\tau) - \frac{|\bar{v}_h\mathbf{m}\times\mathbf{n}_\tau|\rho_h\big|_\tau - \bar{v}_h\mathbf{n}_\tau\cdot(\boldsymbol{\kappa}_h\big|_\tau\times\mathbf{m})}{-2|\bar{v}_h\mathbf{m}\times\mathbf{n}_\tau|} \begin{pmatrix} -|\bar{v}_h\mathbf{m}\times\mathbf{n}_\tau| \\ \bar{v}_h\mathbf{m}\times\mathbf{n}_\tau \end{pmatrix}.\end{aligned}$$

The concept of a free outflow (or transparent) boundary is essential. This motivates a different view. To this end, we deduce an exact solution of the CDD system (5.1) for the simplified situation of a constant dislocation velocity $v \equiv v_0 \in \mathbb{R}$.

If initially only straight dislocation lines are present in $\mathcal{B}$, i.e. $q(0,\cdot) \equiv 0$, and a constant dislocation velocity is assumed, the curvature density source term vanishes since then $\mathbf{g} \equiv 0$. Thus the dislocations move without any change of line orientation through the material and we conclude

$$q(t,\mathbf{x}) = 0 \qquad \text{for all } \mathbf{x} \in \mathcal{B} \text{ and } t \in (0,\infty).$$

In this situation, we can construct solutions of the CDD system by only considering the first equation (5.1a). Assuming that a differentiable amplitude function $P \in C^1(\mathbb{R}, [0,\infty))$ is given which describes the dislocation density motion in direction $\mathbf{e}$ via

$$\rho(t,\mathbf{x}) = P(v_0 t - \mathbf{x}\cdot\mathbf{e}),$$

we construct $\boldsymbol{\kappa}$ such that the first equation (5.1a) is fulfilled. We assume $|\mathbf{e}| = 1$ and since we are interested in dislocation gliding we furthermore assume $\mathbf{e}\cdot\mathbf{m} = 0$. Exploiting

$$\partial_t \rho(t,\mathbf{x}) = v_0 P'(v_0 t - \mathbf{x}\cdot\mathbf{e}) \qquad \text{and} \qquad \nabla\rho(t,\mathbf{x}) = -P'(v_0 t - \mathbf{x}\cdot\mathbf{e})\mathbf{e}$$

yields

$$\partial_t \boldsymbol{\kappa} = \nabla \times (\rho v_0 \mathbf{m}) = -v_0\, \mathbf{m}\times\nabla\rho = \partial_t\rho\, \mathbf{m}\times\mathbf{e}\,.$$

Thus, we choose

$$\boldsymbol{\kappa} = \rho\mathbf{m}\times\mathbf{e}\,, \qquad \boldsymbol{\kappa}^\perp = \boldsymbol{\kappa}\times\mathbf{m} = \rho\mathbf{e}\,,$$

so that

$$-\nabla\cdot(v_0\boldsymbol{\kappa}^\perp) = -v_0\nabla\rho\cdot\mathbf{e} = \partial_t\rho.$$

Together, we obtain a solution of the CDD system with $q \equiv 0$ by

$$\begin{aligned} \rho(t,\mathbf{x}) &= P(v_0 t - \mathbf{x}\cdot\mathbf{e}) && \text{in } (0,\infty)\times\mathcal{B} \\ \boldsymbol{\kappa}(t,\mathbf{x}) &= \rho(t,\mathbf{x})\mathbf{m}\times\mathbf{e}, && \text{in } (0,\infty)\times\mathcal{B} \\ q(t,\mathbf{x}) &= 0 && \text{in } (0,\infty)\times\mathcal{B} \end{aligned} \tag{5.20}$$

with initial values $\rho(0,\cdot), \boldsymbol{\kappa}(0,\cdot)$ and $q(0,\cdot)$.

If $P \in L^2(\mathbb{R}, [0, \infty))$, this is a weak solution of the CDD system satisfying

$$(\partial_t \mathbf{w}, \boldsymbol{\varphi})_{\mathcal{B}} + (A\mathbf{w}, \boldsymbol{\varphi})_{\mathcal{B}} = 0 \qquad \text{for all } \boldsymbol{\varphi} \in C_c^1(\mathcal{B}, \mathbb{R} \times \Gamma).$$

With regard to the fact that in this solution a profile given by the amplitude function P moves without change through the volume, the solution (5.20) is called a *traveling wave* solution.

A traveling wave solution with $\mathbf{e} = \mathbf{n}$ moving towards a boundary with outer normal $\mathbf{n}$ (or $-\mathbf{n}$ for $v_0 < 0$) satisfies the free outflow boundary condition (5.19), i.e., the dislocation density leaves the domain without any reflections at the boundary.

Impenetrable boundary

For the definition of impenetrable boundary conditions, we need do prevent any dislocation density outflow. Hence, we have to ensure that the flux over the boundary vanishes, i.e.

$$\mathbf{n} \cdot \mathbf{F}(\mathbf{w}) = \mathbf{B}_{\mathbf{n}} \begin{pmatrix} \rho \\ \boldsymbol{\kappa} \end{pmatrix} = \begin{pmatrix} \mathbf{n} \cdot (v\boldsymbol{\kappa} \times \mathbf{m}) \\ -\mathbf{n} \times (v\rho\mathbf{m}) \end{pmatrix} = v \begin{pmatrix} \boldsymbol{\kappa} \cdot (\mathbf{m} \times \mathbf{n}) \\ \rho \mathbf{m} \times \mathbf{n} \end{pmatrix} = \mathbf{0}. \tag{5.21}$$

In order to match the Robin-type boundary condition setting (5.16), we split Equation (5.21) into

$$v\boldsymbol{\kappa} \cdot (\mathbf{m} \times \mathbf{n}) = 0 \tag{5.22a}$$

$$v\rho \mathbf{m} \times \mathbf{n} = \mathbf{0}. \tag{5.22b}$$

If $|v\mathbf{m} \times \mathbf{n}| = 0$ the flux vanishes immediately. Otherwise, (5.22a) and (5.22b) are each Robin boundary conditions with

$$\vartheta = 0, \qquad \delta = 1 \qquad \omega = 0$$

and

$$\vartheta = 1, \qquad \delta = 0 \qquad \omega = 0,$$

respectively. The corresponding upwind fluxes are given by

$$\mathbf{n}_\tau \cdot \mathbf{F}^*_{\tau,f}(\mathbf{w}_h) = \mathbf{n}_\tau \cdot \mathbf{F}(\mathbf{w}_h\big|_\tau) - \frac{\bar{v}_h \mathbf{n}_\tau \cdot (\boldsymbol{\kappa}_h\big|_\tau \times \mathbf{m})}{|\bar{v}_h \mathbf{m} \times \mathbf{n}_\tau|} \begin{pmatrix} -|\bar{v}_h \mathbf{m} \times \mathbf{n}_\tau| \\ \bar{v}_h \mathbf{m} \times \mathbf{n}_\tau \end{pmatrix} \quad \text{for (5.22a)}$$

and

$$\mathbf{n}_\tau \cdot \mathbf{F}^*_{\tau,f}(\mathbf{w}_h) = \mathbf{n}_\tau \cdot \mathbf{F}(\mathbf{w}_h\big|_\tau) + \frac{|\bar{v}_h \mathbf{m} \times \mathbf{n}_\tau| \rho_h\big|_\tau}{|\bar{v}_h \mathbf{m} \times \mathbf{n}_\tau|} \begin{pmatrix} -|\bar{v}_h \mathbf{m} \times \mathbf{n}_\tau| \\ \bar{v}_h \mathbf{m} \times \mathbf{n}_\tau \end{pmatrix} \quad \text{for (5.22b).}$$

For

$$\bar{v}_h \mathbf{n}_\tau \cdot (\boldsymbol{\kappa}_h\big|_\tau \times \mathbf{m}) + \rho_h\big|_\tau |\bar{v}_h \mathbf{m} \times \mathbf{n}_\tau| \neq 0$$

these numerical fluxes do not coincide. Thus, in general, we cannot define an upwind flux for impenetrable boundary conditions simultaneously for ρ and $\boldsymbol{\kappa}$. The canonical way to implement this boundary condition by prescribing

$$\mathbf{n}_\tau \cdot \mathbf{F}^*_{\tau,f}(\mathbf{w}_h) = \mathbf{0}.$$

is not an upwind flux and might be unstable.

Depending on the specific application, it may be necessary to include a smoothing in order to obtain a stable solution scheme. This can be achieved by installing a transition zone of width ε, i.e.

$$v^\varepsilon(t,\mathbf{x}) = \lambda^\varepsilon(\mathbf{x}\cdot\mathbf{n})\, v(t,\mathbf{x}) \qquad \text{with} \qquad \lambda^\varepsilon(x) = \begin{cases} 1 & x < -\varepsilon \\ 0 & x > \varepsilon \end{cases}. \tag{5.23}$$

For $-\varepsilon < x < \varepsilon$, a smooth passage is used, e.g. $\lambda^\varepsilon(x) = \frac{1}{2} - \frac{1}{2}\sin\left(\frac{\pi}{2\varepsilon}x\right)$. By this means, the dislocations are decelerated when approaching the boundary. Hence, the jump-like effect of an impenetrable boundary is attenuated.

Remark. The smoothing on an impenetrable boundary should be used carefully. It is an artificial modification of the underlying physical model. If the transition zone is chosen too large, the dislocation motion is manipulated in a physically not reasonable manner. Essential dislocation interactions based on the eigenstresses may be blurred. If the zone is too small, however, the smoothing does not have the desired effect and the resulting scheme may still be unstable. A zone consisting of several cells in a rather fine mesh is recommendable in practice.

Dirichlet and Neumann boundary

In addition to the boundary conditions which directly go along with dislocation density outflow, it may possibly be helpful to use inflow boundary conditions. The definition of an inflow boundary condition can e.g. be of interest for a homogeneous dislocation density distribution when considering a small volume embedded in a larger one. On this account, the upwind flux for a boundary condition prescribing either ρ or $\boldsymbol{\kappa}\cdot(\mathbf{m}\times\mathbf{n})$ is stated in the following. Both types of boundary conditions fit in the general boundary condition setting (5.16).

We choose $\vartheta = 1$ and $\delta = 0$ for a Dirichlet boundary of the form

$$v\rho(t, \mathbf{x}) = \omega \tag{5.24}$$

on $\mathbf{x} \cdot \mathbf{n} = 0$ for $\omega \in \mathbb{R}$. In this case, the respective Riemann solution is obtained from the general formulation by setting

$$\zeta = \frac{\omega - |v\mathbf{m}\times\mathbf{n}|\rho^-}{|v\mathbf{m}\times\mathbf{n}|^2}.$$

This yields the upwind flux on a boundary face f satisfying the Dirichlet boundary (5.24) given by

$$\mathbf{n}_\tau \cdot \mathbf{F}^*_{\tau,f}(\mathbf{w}_h) = \mathbf{n}_\tau \cdot \mathbf{F}(\mathbf{w}_h\big|_\tau) + \frac{\omega - |\bar{v}_h\mathbf{m}\times\mathbf{n}_\tau|\rho_h\big|_\tau}{|\bar{v}_h\mathbf{m}\times\mathbf{n}_\tau|}\begin{pmatrix} -|\bar{v}_h\mathbf{m}\times\mathbf{n}_\tau| \\ \bar{v}_h\mathbf{m}\times\mathbf{n}_\tau \end{pmatrix}.$$

Similarly, a Neumann boundary of the form

$$v\boldsymbol{\kappa} \cdot (\mathbf{m}\times\mathbf{n}) = \omega \tag{5.25}$$

on $\mathbf{x} \cdot \mathbf{n} = 0$ for $\omega \in \mathbb{R}$ can be achieved by choosing $\vartheta = 0$ and $\delta = 1$. With the Riemann solution given by

$$\zeta = \frac{v\mathbf{n} \cdot (\boldsymbol{\kappa}^-\times\mathbf{m}) - \omega}{|v\mathbf{m}\times\mathbf{n}|^2},$$

the upwind flux on a face f with Neumann boundary condition (5.25) is

$$\mathbf{n}_\tau \cdot \mathbf{F}^*_{\tau,f}(\mathbf{w}_h) = \mathbf{n}_\tau \cdot \mathbf{F}(\mathbf{w}_h\big|_\tau) + \frac{\omega - \bar{v}_h\mathbf{n}_\tau \cdot (\boldsymbol{\kappa}_h\big|_\tau\times\mathbf{m})}{-|\bar{v}_h\mathbf{m}\times\mathbf{n}_\tau|}\begin{pmatrix} -|\bar{v}_h\mathbf{m}\times\mathbf{n}_\tau| \\ \bar{v}_h\mathbf{m}\times\mathbf{n}_\tau \end{pmatrix}.$$

Altogether, we now have a space discretization scheme for the first sub-problem (5.2) including the numerical flux on inner and boundary faces.

5.4 Space discretization of the second sub-problem

The space discretization of the second sub-problem (5.3) can be accomplished in a very similar way as for the first sub-problem (5.2). For given $\mathbf{w} \in C^1(\mathcal{B}, \mathbb{R}\times\Gamma)$ and $v \in C^2(\mathcal{B}, \mathbb{R})$ we aim to solve

$$\partial_t q = -\nabla \cdot \mathbf{f}(\mathbf{w}, q) - \nabla \cdot \mathbf{g}(\mathbf{w}).$$

In the following, we define the corresponding differential operator C with dense domain $\mathcal{D}(C) \subset L^2(\mathcal{B}, \mathbb{R})$.

In order to avoid the evaluation of the second derivative of the dislocation velocity v, we impose the production term $-\nabla \cdot \mathbf{g}(\mathbf{w})$ on the right-hand side weakly, i.e. by using integration by parts once. Therefore, we consider the modified weak formulation: Find $q \in \mathcal{D}(C)$ satisfying

$$(\partial_t q, \varphi)_{\mathcal{B}} = -(\nabla \cdot \mathbf{f}(\mathbf{w}, q), \varphi)_{\mathcal{B}} + (\mathbf{g}(\mathbf{w}), \nabla\varphi)_{\mathcal{B}} - (\mathbf{n} \cdot \mathbf{g}(\mathbf{w}), \varphi)_{\partial\mathcal{B}} \quad \text{for all } \varphi \in \mathcal{D}(C).$$

By doing so, it is sufficient to require $v \in C^1(\mathcal{B}, \mathbb{R})$.

This problem fits in the general framework (5.4) for $J = 1$ by defining the linear operator

$$C \colon C_{\mathrm{c}}^1(\mathcal{B}, \mathbb{R}) \to L^2(\mathcal{B}, \mathbb{R}), \quad q \mapsto \nabla \cdot \left(\frac{vq}{\rho} \boldsymbol{\kappa}^{\perp} \right).$$

We deduce the adjoint operator C^* to C by computing

$$(Cq, \varphi)_{\mathcal{B}} = \int_{\mathcal{B}} \varphi \nabla \cdot \left(\frac{vq}{\rho} \boldsymbol{\kappa}^{\perp} \right) \mathrm{d}\mathbf{x} = - \int_{\mathcal{B}} \nabla\varphi \cdot \left(\frac{vq}{\rho} \boldsymbol{\kappa}^{\perp} \right) \mathrm{d}\mathbf{x} = (q, C^*\varphi)_{\mathcal{B}}$$

for test functions $\varphi \in C_{\mathrm{c}}^1(\mathcal{B}, \mathbb{R})$. Therefore, the adjoint operator reads

$$C^* \colon C_{\mathrm{c}}^1(\mathcal{B}, \mathbb{R}) \to L^2(\mathcal{B}, \mathbb{R}), \quad \varphi \mapsto -\nabla\varphi \cdot \left(\frac{v}{\rho} \boldsymbol{\kappa}^{\perp} \right).$$

This allows to define the space

$$H(C, \mathcal{B}) = \{ x \in L^2(\mathcal{B}, \mathbb{R}) \colon \exists y \in L^2(\mathcal{B}, \mathbb{R}) \ \ (y, z)_{\mathcal{B}} = (x, C^* z)_{\mathcal{B}} \ \forall z \in C_{\mathrm{c}}^1(\mathcal{B}, \mathbb{R}) \}.$$

It is complete with respect to the graph norm $\|\cdot\|_C = \sqrt{\|\cdot\|^2 + \|C\cdot\|^2}$ and thus a Hilbert space. Again since

$$C_{\mathrm{c}}^1(\mathcal{B}, \mathbb{R}) \subset H(C, \mathcal{B}) \subset L^2(\mathcal{B}, \mathbb{R}),$$

the Hilbert space $H(C, \mathcal{B})$ is dense in $L^2(\mathcal{B}, \mathbb{R})$. By extending the operator C to $H(C, \mathcal{B})$, we choose the dense domain $\mathcal{D}(C) \subset H(C, \mathcal{B})$ depending on the chosen boundary condition. By doing so, also the second sub-problem fits in the abstract framework. In the L^2-setting, it is sufficient to claim $\frac{1}{\rho}\boldsymbol{\kappa}^{\perp} \in L^\infty(\mathcal{B}, \Gamma)$ and $v \in L^\infty(\mathcal{B}, \mathbb{R})$.

5.4.1 Discrete operator

We proceed by deriving the discrete problem to the second sub-problem (5.3). The corresponding discontinuous Galerkin operator C_h is given by

$$\left(C_h q_h, \varphi_{\tau,h}\right)_\tau = -\left(\mathbf{f}(\mathbf{w}, q_h), \nabla\varphi_{\tau,h}\right)_\tau + \sum_{f\in\mathcal{F}_\tau} \left(\mathbf{n}_\tau \cdot \mathbf{f}^*_{\tau,f}(\mathbf{w}, q_h), \varphi_{\tau,h}\right)_f \quad \text{for all } \varphi_{\tau,h} \in \mathbb{P}_p(\tau)$$

for $q_h \in \mathbb{P}_p(\tau)$.

In order to transfer the weak consideration of the right-hand side in the whole domain $\mathcal{B}$ to a cell-wise relation, we assume $\mathbf{w}$ and the dislocation velocity to be continuous in the following, i.e. $\frac{1}{\rho}\boldsymbol{\kappa}^\perp \in L^\infty(\mathcal{B},\Gamma) \cap C(\mathcal{B},\Gamma)$ and $v \in L^\infty(\mathcal{B},\mathbb{R}) \cap C(\mathcal{B},\mathbb{R})$.

This allows to approximate a solution q of the second sub-problem (5.3) by $q_h \in W_h$ satisfying

$$\left(\partial_t q_h, \varphi_h\right)_\mathcal{B} + \sum_{\tau\in\mathcal{T}} \left(C_h q_h, \varphi_h\right)_\tau = \sum_{\tau\in\mathcal{T}} \Big[\left(\mathbf{g}(\mathbf{w}), \nabla\varphi_h\right)_\tau - \left(\mathbf{n}_\tau \cdot \mathbf{g}(\mathbf{w}), \varphi_h\right)_{\partial\tau}\Big] \text{ for all } \varphi_h \in W_h.$$

Here, the discontinuous Galerkin space used is given by

$$W_h = \{\varphi \in L^2(\mathcal{B},\mathbb{R})\colon \varphi\big|_\tau \in \mathbb{P}_p(\tau)\ \forall\tau\in\mathcal{T}\}.$$

It remains to specify the numerical flux $\mathbf{f}^*_{\tau,f}$ for the space discretization of the second sub-problem (5.3).

5.4.2 Upwind flux on inner faces

For the second sub-problem the upwind flux can be deduced in an analogous manner as for the first sub-problem by solving the Riemann problem to

$$\partial_t q = -\nabla\cdot\mathbf{f}(\mathbf{w}, q) \qquad \text{in } \mathcal{B}_t$$

for given $\mathbf{w}$. In this case, the flux matrix $\mathbf{B}_\mathbf{n}(\mathbf{w}, q) = \mathbf{n}\cdot\mathbf{f}(\mathbf{w}, q)$ is in fact scalar.

We have required that v and $\mathbf{w}$ are continuous. This is a severe limitation since the used splitting method only yields an approximated solution $\mathbf{w}_h$ of the first sub-problem in the respective discontinuous Galerkin space. To overcome this issue, we use a similar approach as for the first sub-problem and compute a continuous approximation of $\mathbf{w}_h$ which we denote by $\bar{\mathbf{w}}_h = (\bar{\rho}_h, \bar{\boldsymbol{\kappa}}_h)$. Besides, we again use the averaged dislocation velocity $\bar{v}_h$.

Then the Riemann solution to initial values q^- for $\mathbf{x}\cdot\mathbf{n} < 0$ and q^+ for $\mathbf{x}\cdot\mathbf{n} > 0$ reads

$$q(t,\mathbf{x}) = \begin{cases} q^- & \mathbf{x}\cdot\mathbf{n} < \dfrac{\bar{v}_h}{\bar{\rho}_h}\bar{\boldsymbol{\kappa}}_h^\perp\cdot\mathbf{n}\,t \\ q^+ & \dfrac{\bar{v}_h}{\bar{\rho}_h}\bar{\boldsymbol{\kappa}}_h^\perp\cdot\mathbf{n}\,t < \mathbf{x}\cdot\mathbf{n}\ . \end{cases} \tag{5.26}$$

This immediately yields the upwind flux on an inner face $f = \partial\tau \cap \partial\tau_f$ by

$$\mathbf{n}_\tau\cdot\mathbf{f}^*_{\tau,f}(\bar{\mathbf{w}}_h, q_h) = \begin{cases} \mathbf{n}_\tau\cdot\mathbf{f}(\bar{\mathbf{w}}_h, q_h|_\tau) & \dfrac{\bar{v}_h}{\bar{\rho}_h}\bar{\boldsymbol{\kappa}}_h^\perp\cdot\mathbf{n} \geq 0 \\ \mathbf{n}_\tau\cdot\mathbf{f}(\bar{\mathbf{w}}_h, q_h|_{\tau_f}) & \dfrac{\bar{v}_h}{\bar{\rho}_h}\bar{\boldsymbol{\kappa}}_h^\perp\cdot\mathbf{n} < 0\ . \end{cases}$$

Remark. As for the first sub-problem, we use the averaged quantities $\bar{v}_h$ and $\bar{\mathbf{w}}_h$ not only for the evaluation of the upwind flux on the cell faces but also in the inner of all cells $\tau \in \mathcal{T}$.

5.4.3 Upwind flux on boundary faces

For the definition of the numerical flux of the second sub-problem on the boundary $\partial\mathcal{B}$ it is helpful to distinguish inflow and outflow boundary

$$\partial_{\text{in}}\mathcal{B}(\bar{\mathbf{w}}_h) = \left\{\mathbf{x}\in\partial\mathcal{B}\colon \frac{\bar{v}_h}{\bar{\rho}_h}\bar{\boldsymbol{\kappa}}_h^\perp\cdot\mathbf{n} < 0\right\}, \qquad \partial_{\text{out}}\mathcal{B}(\bar{\mathbf{w}}_h) = \left\{\mathbf{x}\in\partial\mathcal{B}\colon \frac{\bar{v}_h}{\bar{\rho}_h}\bar{\boldsymbol{\kappa}}_h^\perp\cdot\mathbf{n} > 0\right\}.$$

While a free outflow boundary as well as an impenetrable boundary are conditions on the outflow boundary $\partial_{\text{out}}\mathcal{B}$, a Dirichlet boundary can only be defined on the inflow boundary $\partial_{\text{in}}\mathcal{B}$.

Free outflow boundary

Equation (5.26) shows that on an outflow boundary, the Riemann solution is given by the inner value. Thus a free outflow boundary condition is obtained by setting the numerical flux on an outflow boundary face $f \in \mathcal{F}_\tau$ to

$$\mathbf{n}_\tau\cdot\mathbf{f}^*_{\tau,f}(\bar{\mathbf{w}}_h, q_h) = \mathbf{n}_\tau\cdot\mathbf{f}(\bar{\mathbf{w}}_h, q_h|_\tau) \qquad \text{on } \partial_{\text{out}}\mathcal{B}.$$

Dirichlet boundary

With the same argument as for the free outflow boundary, we can prescribe a Dirichlet value q on an inflow boundary face $f \in \mathcal{F}_\tau$ by setting

$$\mathbf{n}_\tau\cdot\mathbf{f}^*_{\tau,f}(\bar{\mathbf{w}}_h, q_h) = \mathbf{n}_\tau\cdot\mathbf{f}(\bar{\mathbf{w}}_h, q) \qquad \text{on } \partial_{\text{in}}\mathcal{B}.$$

Impenetrable boundary

Before defining an impenetrable boundary condition for the second sub-problem, one first needs to understand what is supposed to happen at an impenetrable boundary for the first sub-problem. The dislocation density accumulates there. Each dislocation line captured by the dislocation density is forced to get aligned with the boundary. If the boundary is straight, the curvature of each dislocation located there is zero. Hence, also the curvature density is supposed to vanish directly at an impenetrable boundary for the first sub-problem.

This relation is represented in the source term $-\nabla \cdot \mathbf{g}$ of the second sub-problem. If different parts of a single dislocation move with different velocity the curvature density increases or decreases. Thus if an impenetrable boundary condition for the first sub-problem is imposed via a smooth passage of the velocity as in (5.23) the corresponding behavior for the curvature density is included through the production term. This mechanism is only valid approximately in the CDD system owing to the truncated series expansion, cf. Section 4.5.

If an impenetrable boundary condition for the first sub-problem is realized directly by setting the numerical flux to zero this physically expected behavior is not included intrinsically in the CDD system. In this case, we circumvent this issue by treating an impenetrable boundary of the first sub-problem as free outflow boundary of the second sub-problem. By this means, we avoid a physically incorrect pile-up behavior of the curvature density.

5.5 Time discretization of the CDD system

Using a discontinuous Galerkin method for the space discretization, we transferred the CDD system (4.8) to the (semi-discrete) approximated weak formulations of the sub-problems (5.2) and (5.3): Find $\mathbf{w}_h \in V_h$ and $q_h \in W_h$ satisfying

$$\begin{aligned}
\left(\partial_t \mathbf{w}_h, \boldsymbol{\varphi}_h\right)_{\mathcal{B}} + \sum_{\tau \in \mathcal{T}} \left(A_h \mathbf{w}_h, \boldsymbol{\varphi}_h\right)_{\tau} &= (\mathbf{G}, \boldsymbol{\varphi}_h)_{\mathcal{B}} && \text{for all } \boldsymbol{\varphi}_h \in V_h \\
\left(\partial_t q_h, \varphi_h\right)_{\mathcal{B}} + \sum_{\tau \in \mathcal{T}} \left(C_h q_h, \varphi_h\right)_{\tau} &= \sum_{\tau \in \mathcal{T}} \Big[(\mathbf{g}, \nabla \varphi_h)_{\tau} - (\mathbf{n}_{\tau} \cdot \mathbf{g}, \varphi_h)_{\partial \tau} \Big] && \text{for all } \varphi_h \in W_h.
\end{aligned}$$

Since we use splitting schemes of order 1 and 2, it is natural to choose a time integration method of order 2 for both sub-problems. We select the implicit midpoint rule which is a stable reversible implicit Runge-Kutta scheme of order 2.

Given an equidistant time grid $t_n = n\triangle t$, $n = 0, \dots, N$, with $N = \frac{T}{\triangle t}$, the approximations in the grid points t_n are denoted by

$$\mathbf{w}_h^n \approx \mathbf{w}_h(t_n) \qquad \text{and} \qquad q_h^n \approx q_h(t_n) \qquad \text{for } n = 0, \dots, N$$

and furthermore the notation

$$\mathbf{w}_h^{n-\frac{1}{2}} = \frac{1}{2}(\mathbf{w}_h^{n-1} + \mathbf{w}_h^n) \qquad \text{and} \qquad q_h^{n-\frac{1}{2}} = \frac{1}{2}(q_h^{n-1} + q_h^n) \qquad \text{for } n = 1, \dots, N$$

is used. Then the implicit midpoint rule on $[t_{n-1}, t_n]$ to approximate $\mathbf{w}_h^n$ and q_h^n, $n = 1, \dots, N$, reads

$$\frac{1}{\triangle t}(\mathbf{w}_h^n - \mathbf{w}_h^{n-1}, \boldsymbol{\varphi}_h)_{\mathcal{B}} + \sum_{\tau \in \mathcal{T}} (A_h \mathbf{w}_h^{n-\frac{1}{2}}, \boldsymbol{\varphi}_h)_\tau = (\mathbf{G}(q_h^{n-1}), \boldsymbol{\varphi}_h)_{\mathcal{B}}$$

and

$$\frac{1}{\triangle t}(q_h^n - q_h^{n-1}, \varphi_h)_{\mathcal{B}} + \sum_{\tau \in \mathcal{T}} (C_h(\bar{\mathbf{w}}_h^{n-1}) q_h^{n-\frac{1}{2}}, \varphi_h)_\tau = \sum_{\tau \in \mathcal{T}} \Big[(\mathbf{g}(\bar{\mathbf{w}}_h^{n-1}), \nabla \varphi_h)_\tau - (\mathbf{n}_\tau \cdot \mathbf{g}(\bar{\mathbf{w}}_h^{n-1}), \varphi_h)_{\partial\tau} \Big].$$

Now, the chosen splitting method is used to merge the approximated solutions of both sub-problems. Examplarily, the resulting discrete approximation scheme for the Strang splitting (QWQ) is given by

$$\begin{aligned}
\frac{2}{\triangle t}(q^{\frac{1}{2}} - q^0, \varphi_h)_{\mathcal{B}} + \sum_{\tau \in \mathcal{T}} (C_h(\bar{\mathbf{w}}_h^0) q_h^{\frac{1}{4}}, \varphi_h)_\tau &= \sum_{\tau \in \mathcal{T}} \Big[(\mathbf{g}(\bar{\mathbf{w}}_h^0), \nabla \varphi_h)_\tau - (\mathbf{n}_\tau \cdot \mathbf{g}(\bar{\mathbf{w}}_h^0), \varphi_h)_{\partial\tau} \Big] \\
\frac{1}{\triangle t}(\mathbf{w}^1 - \mathbf{w}^0, \boldsymbol{\varphi}_h)_{\mathcal{B}} + \sum_{\tau \in \mathcal{T}} (A_h \mathbf{w}_h^{\frac{1}{2}}, \boldsymbol{\varphi}_h)_\tau &= (\mathbf{G}(\mathbf{q}_h^{\frac{1}{2}}), \boldsymbol{\varphi}_h)_{\mathcal{B}} \\
\frac{1}{\triangle t}(q^{\frac{3}{2}} - q^{\frac{1}{2}}, \varphi_h)_{\mathcal{B}} + \sum_{\tau \in \mathcal{T}} (C_h(\bar{\mathbf{w}}_h^1) q_h^1, \varphi_h)_\tau &= \sum_{\tau \in \mathcal{T}} \Big[(\mathbf{g}(\bar{\mathbf{w}}_h^1), \nabla \varphi_h)_\tau - (\mathbf{n}_\tau \cdot \mathbf{g}(\bar{\mathbf{w}}_h^1), \varphi_h)_{\partial\tau} \Big] \\
\frac{1}{\triangle t}(\mathbf{w}^2 - \mathbf{w}^1, \boldsymbol{\varphi}_h)_{\mathcal{B}} + \sum_{\tau \in \mathcal{T}} (A_h \mathbf{w}_h^{\frac{3}{2}}, \boldsymbol{\varphi}_h)_\tau &= (\mathbf{G}(\mathbf{q}_h^{\frac{3}{2}}), \boldsymbol{\varphi}_h)_{\mathcal{B}} \\
&\vdots \\
\frac{1}{\triangle t}(\mathbf{w}^N - \mathbf{w}^{N-1}, \boldsymbol{\varphi}_h)_{\mathcal{B}} + \sum_{\tau \in \mathcal{T}} (A_h \mathbf{w}_h^{N-\frac{1}{2}}, \boldsymbol{\varphi}_h)_\tau &= (\mathbf{G}(\mathbf{q}_h^{N-\frac{1}{2}}), \boldsymbol{\varphi}_h)_{\mathcal{B}} \\
\frac{1}{\triangle t}(q^N - q^{N-\frac{1}{2}}, \varphi_h)_{\mathcal{B}} + \sum_{\tau \in \mathcal{T}} (C_h(\bar{\mathbf{w}}_h^N) q_h^{N-\frac{1}{4}}, \varphi_h)_\tau &= \sum_{\tau \in \mathcal{T}} \Big[(\mathbf{g}(\bar{\mathbf{w}}_h^N), \nabla \varphi_h)_\tau - (\mathbf{n}_\tau \cdot \mathbf{g}(\bar{\mathbf{w}}_h^N), \varphi_h)_{\partial\tau} \Big].
\end{aligned}$$

CHAPTER 6
Approximation of the coupled model

Proceeding from the numerical approximation scheme for the CDD system we provided in Chapter 5, in this chapter a numerical scheme for the approximation of the fully-coupled elastoplasticity model is developed. To this end, first a space discretization of the quasi-static macroscopic problem is presented using a conforming finite element method. Then, in order to solve the fully-coupled model for a single crystal, the CDD evolution and the solution of the macroscopic balance laws are coupled explicitly. For this purpose, the dislocation velocity law needs to be evaluated based on the approximated Cauchy stress tensor and the approximated CDD variables. Finally, the approximation scheme for the dislocation based continuum elastoplasticity model is extended to polycrystals. We conclude the chapter with some remarks on the implementation.

A concise overview of all relevant physical quantities and the governing equations for the fully-coupled model is given in Table 6.1.

6.1 Approximation of the macroscopic problem

We first consider the macroscopic equilibria (2.1) subject to boundary conditions (2.2). The plastic strain tensor $\boldsymbol{\varepsilon}^{\mathrm{pl}}$ is assumed to be given. Thus we aim to find a solution $\mathbf{u} \in C^1(\mathcal{B}, \mathbb{R}^3) \cap C(\overline{\mathcal{B}}, \mathbb{R}^3)$ to

$$-\operatorname{div} \boldsymbol{\sigma}(\mathbf{u}) = \mathbf{b}_{\mathcal{B}} \quad \text{in } \mathcal{B} \qquad \text{and} \qquad \boldsymbol{\sigma}(\mathbf{u}) = \boldsymbol{\sigma}(\mathbf{u})^{\top} \quad \text{in } \mathcal{B} \tag{6.1}$$

satisfying the boundary conditions

$$\mathbf{u} = \mathbf{u}_{\mathrm{D}} \quad \text{on } \partial_{\mathrm{D}}\mathcal{B} \qquad \text{and} \qquad \boldsymbol{\sigma}(\mathbf{u})\mathbf{n} = \mathbf{t}_{\mathrm{N}} \quad \text{on } \partial_{\mathrm{N}}\mathcal{B}$$

for given Dirichlet values $\mathbf{u}_{\mathrm{D}} \colon \partial_{\mathrm{D}}\mathcal{B} \to \mathbb{R}^3$ and surface traction vector $\mathbf{t}_{\mathrm{N}} \colon \partial_{\mathrm{N}}\mathcal{B} \to \mathbb{R}^3$. The stress tensor $\boldsymbol{\sigma}$ is related to the displacement $\mathbf{u}$ via Hooke's law $\boldsymbol{\sigma}(\mathbf{u}) = \mathbb{C}[\boldsymbol{\varepsilon}(\mathbf{u}) - \boldsymbol{\varepsilon}^{\mathrm{pl}}]$.

Primary variables	
displacement	$\mathbf{u}\colon [0,T]\times\overline{\mathcal{B}}\to\mathbb{R}^3$
plastic shear strain	$\gamma_s\colon [0,T]\times\overline{\mathcal{B}}\to\mathbb{R}$
dislocation density	$\rho_s\colon [0,T]\times\overline{\mathcal{B}}\to\mathbb{R}$
GND density vector	$\boldsymbol{\kappa}_s\colon [0,T]\times\overline{\mathcal{B}}\to\Gamma_s$
curvature density	$q_s\colon [0,T]\times\overline{\mathcal{B}}\to\mathbb{R}$
Quantities depending on the primary variables	
infinitesimal strain	$\boldsymbol{\varepsilon}(\mathbf{u})=\operatorname{sym}(\mathrm{D}\mathbf{u})\colon [0,T]\times\overline{\mathcal{B}}\to\mathbb{R}^{3\times3}_{\mathrm{sym}}$
plastic distortion	$\boldsymbol{\beta}^{\mathrm{pl}}(\boldsymbol{\gamma})=\sum_s\gamma_s\mathbf{m}_s\otimes\mathbf{d}_s\colon [0,T]\times\overline{\mathcal{B}}\to\mathbb{R}^{3\times3}$
plastic strain	$\boldsymbol{\varepsilon}^{\mathrm{pl}}(\boldsymbol{\gamma})=\operatorname{sym}(\boldsymbol{\beta}^{\mathrm{pl}}(\boldsymbol{\gamma}))\colon [0,T]\times\overline{\mathcal{B}}\to\mathbb{R}^{3\times3}_{\mathrm{sym}}$
elastic strain	$\boldsymbol{\varepsilon}^{\mathrm{el}}(\mathbf{u},\boldsymbol{\gamma})=\boldsymbol{\varepsilon}(\mathbf{u})-\boldsymbol{\varepsilon}^{\mathrm{pl}}(\boldsymbol{\gamma})\colon [0,T]\times\overline{\mathcal{B}}\to\mathbb{R}^{3\times3}_{\mathrm{sym}}$
Constitutive setting	
Cauchy stress	$\boldsymbol{\sigma}=\mathbb{C}[\boldsymbol{\varepsilon}^{\mathrm{el}}]=\lambda\operatorname{Tr}(\boldsymbol{\varepsilon}^{\mathrm{el}})\mathbf{I}+2\mu\boldsymbol{\varepsilon}^{\mathrm{el}}$
resolved shear stress	$\tau_s^{\mathrm{res}}=\mathbf{d}_s\cdot\boldsymbol{\sigma}\mathbf{m}_s$
back stress	$\tau_s^{\mathrm{b}}=\frac{D\mu b_s}{\rho_s}\nabla\cdot\boldsymbol{\kappa}_s^{\perp}$
effective stress	$\tau_s^{\mathrm{eff}}=\tau_s^{\mathrm{res}}-\tau_s^{\mathrm{b}}$
yield stress	$\tau_s^{\mathrm{y}}=\mu b_s\sqrt{\sum_n a_{sn}\rho_n}$
dislocation velocity	$v_s=\frac{b_s}{B}\operatorname{sgn}(\tau_s^{\mathrm{eff}})\max\left\{0,\lvert\tau_s^{\mathrm{eff}}\rvert-\tau_s^{\mathrm{y}}\right\}$
alignment tensor	$\mathbf{A}_s\approx\frac{1}{2\lvert\boldsymbol{\kappa}_s\rvert^2}\left((\rho_s+\lvert\boldsymbol{\kappa}_s\rvert)\boldsymbol{\kappa}_s\otimes\boldsymbol{\kappa}_s+(\rho_s-\lvert\boldsymbol{\kappa}_s\rvert)\boldsymbol{\kappa}_s^{\perp}\otimes\boldsymbol{\kappa}_s^{\perp}\right)$
Material parameters	
Lamé parameters	μ,λ
drag coefficient	B
yields stress parameters	$a_{sn},\ s,n=1,\dots,S$
back stress parameter	D
Data and initial values	
body load	$\mathbf{b}_{\mathcal{B}}\colon\mathcal{B}\to\mathbb{R}^3$
traction force	$\mathbf{t}_{\mathrm{N}}\colon\partial_{\mathrm{N}}\mathcal{B}\to\mathbb{R}^3$
boundary displacements	$\mathbf{u}_{\mathrm{D}}\colon\partial_{\mathrm{D}}\mathcal{B}\to\mathbb{R}^3$
initial displacement	$\mathbf{u}(0,\cdot)\equiv\mathbf{0}$
initial plastic slip	$\gamma_s(0,\cdot)\colon\mathcal{B}\to\mathbb{R}$
initial dislocation density	$\rho_s(0,\cdot)\colon\mathcal{B}\to\mathbb{R}$
initial GND density vector	$\boldsymbol{\kappa}_s(0,\cdot)\colon\mathcal{B}\to\Gamma_s$
initial curvature density	$q_s(0,\cdot)\colon\mathcal{B}\to\mathbb{R}$
Differential equations	
Stress equilibrium	$-\operatorname{div}\boldsymbol{\sigma}=\mathbf{b}_{\mathcal{B}}$ in $(0,T)\times\mathcal{B}$ for $\boldsymbol{\sigma}=\mathbb{C}[\boldsymbol{\varepsilon}(\mathbf{u})-\boldsymbol{\varepsilon}^{\mathrm{pl}}(\boldsymbol{\gamma})]$
Orowan equation	$\partial_t\gamma_s=b_s\rho_s v_s$ in $(0,T)\times\overline{\mathcal{B}}$,
dislocation density evolution	$\partial_t\begin{pmatrix}\rho_s\\ \boldsymbol{\kappa}_s\end{pmatrix}=\begin{pmatrix}-\nabla\cdot(v_s\boldsymbol{\kappa}_s\times\mathbf{m}_s)\\ \nabla\times(v_s\rho_s\mathbf{m}_s)\end{pmatrix}+\begin{pmatrix}v_sq_s\\ \mathbf{0}\end{pmatrix}$ in $(0,T)\times\mathcal{B}$
curvature density evolution	$\partial_t q_s=-\nabla\cdot\left(v_s\frac{q_s}{\rho_s}\boldsymbol{\kappa}_s^{\perp}+\mathbf{A}_s\nabla v_s\right)$ in $(0,T)\times\mathcal{B}$
Boundary conditions	
displacement	$\mathbf{u}=\mathbf{u}_{\mathrm{D}}$ on $\partial_{\mathrm{D}}\mathcal{B}$
traction force	$\boldsymbol{\sigma}\mathbf{n}=\mathbf{t}_{\mathrm{N}}$ on $\partial_{\mathrm{N}}\mathcal{B}$
free outflow boundary	$-\lvert v_s\mathbf{m}_s\times\mathbf{n}\rvert\rho_s+v_s\mathbf{n}\cdot(\boldsymbol{\kappa}_s\times\mathbf{m}_s)=0$ on $[0,T]\times\partial_{\mathrm{N}}\mathcal{B}\cap\partial\mathcal{B}$
impenetrable boundary	$v_s\begin{pmatrix}\boldsymbol{\kappa}_s\cdot(\mathbf{m}_s\times\mathbf{n})\\ \rho_s\mathbf{m}_s\times\mathbf{n}\end{pmatrix}=\mathbf{0}$ on $[0,T]\times(\partial_{\mathrm{D}}\mathcal{B}\cup\partial_{\mathrm{I}}\mathcal{B})\cap\partial\mathcal{B}$
inflow boundary	$q_s=0$ on $[0,T]\times\partial_{\mathrm{in}}\mathcal{B}$

Table 6.1: Fully-coupled dislocation based quasi-static elastoplasticity

For the derivation of the corresponding variational formulation, we multiply (6.1) with a test function $\boldsymbol{\varphi} \in U(\mathbf{0})$ where $U = H^1(\mathcal{B}, \mathbb{R}^3)$ and

$$U(\mathbf{0}) = \{\mathbf{u} \in U \colon \mathbf{u} = \mathbf{0} \text{ on } \partial_{\mathrm{D}}\mathcal{B}\}.$$

By integrating over the domain $\mathcal{B}$ and using integration by parts, we obtain

$$(\boldsymbol{\sigma}, \nabla\boldsymbol{\varphi})_{\mathcal{B}} - (\mathbf{t}_{\mathrm{N}}, \boldsymbol{\varphi})_{\partial_{\mathrm{N}}\mathcal{B}} = (\mathbf{b}_{\mathcal{B}}, \boldsymbol{\varphi})_{\mathcal{B}}.$$

Now exploiting the symmetry of the stress tensor by

$$\boldsymbol{\sigma} : \nabla\boldsymbol{\varphi} = \boldsymbol{\sigma} : \operatorname{sym}(\nabla\boldsymbol{\varphi}) \; = \boldsymbol{\sigma} : \boldsymbol{\varepsilon}(\boldsymbol{\varphi})$$

and inserting Hooke's law yield the resulting weak formulation: Find $\mathbf{u} \in \mathbf{u}_{\mathrm{D}} + U(\mathbf{0})$ such that

$$(\mathbb{C}[\boldsymbol{\varepsilon}(\mathbf{u}) - \boldsymbol{\varepsilon}^{\mathrm{pl}}], \boldsymbol{\varepsilon}(\boldsymbol{\varphi}))_{\mathcal{B}} = (\mathbf{b}_{\mathcal{B}}, \boldsymbol{\varphi})_{\mathcal{B}} + (\mathbf{t}_{\mathrm{N}}, \boldsymbol{\varphi})_{\partial_{\mathrm{N}}\mathcal{B}} \quad \text{for all} \quad \boldsymbol{\varphi} \in U(\mathbf{0})\,.$$

We define the bilinear form

$$b \colon U \times U \to \mathbb{R}, \quad b(\mathbf{u}, \mathbf{v}) = (\mathbb{C}[\boldsymbol{\varepsilon}(\mathbf{u})], \boldsymbol{\varepsilon}(\mathbf{v}))_{\mathcal{B}}$$

and rewrite the weak formulation: Find $\mathbf{u} \in \mathbf{u}_{\mathrm{D}} + U(\mathbf{0})$ such that

$$b(\mathbf{u}, \boldsymbol{\varphi}) = (\mathbf{b}_{\mathcal{B}}, \boldsymbol{\varphi})_{\mathcal{B}} + (\mathbb{C}[\boldsymbol{\varepsilon}^{\mathrm{pl}}], \boldsymbol{\varepsilon}(\boldsymbol{\varphi}))_{\mathcal{B}} + (\mathbf{t}_{\mathrm{N}}, \boldsymbol{\varphi})_{\partial_{\mathrm{N}}\mathcal{B}} \quad \text{for all} \quad \boldsymbol{\varphi} \in U(\mathbf{0})\,. \tag{6.2}$$

With Korn's inequalities (e.g. Ern and Guermond, 2004, Theorem 3.77 and 3.78) it can be shown that the bilinear form b is coercive. This property given, the Lax-Milgram lemma (e.g. Ern and Guermond, 2004, Lemma 2.2) yields the well-posedness of the weak formulation (6.2) for $\mathbf{b}_{\mathcal{B}} \in L^2(\mathcal{B}, \mathbb{R}^3)$, $\mathbb{C}[\boldsymbol{\varepsilon}^{\mathrm{pl}}] \in L^2(\mathcal{B}, \mathbb{R}^{3\times3})$ and $\mathbf{t}_{\mathrm{N}} \in L^2(\partial_{\mathrm{N}}\mathcal{B}, \mathbb{R}^3)$.

We use a conforming finite element approximation for the space discretization. Thus we choose a finite-dimensional space $U_h \subset U$ for the approximation. As for the space discretization of the CDD system in the previous chapter, the domain $\mathcal{B}$ is assumed to be polyhedral and decomposed into a finite number of open polyhedrons $\tau \in \mathcal{T}$ such that $\overline{\mathcal{B}} = \bigcup_{\tau\in\mathcal{T}} \overline{\tau}$. Furthermore, the Dirichlet boundary $\partial_{\mathrm{D}}\mathcal{B}$ is assumed to be composed of cell faces. We use the same mesh for the solution of the CDD system and the macroscopic problem in the fully-coupled model.

On each cell $\tau \in \mathcal{T}$ the solution $\mathbf{u}$ to (6.2) is approximated by a polynomial of degree less or equal one. Unlike the discontinuous Galerkin approach for the CDD system, we choose

a continuous ansatz space U_h here. Thus in a Galerkin approach the finite-dimensional space

$$U_h = \{\mathbf{u} \in C(\overline{\mathcal{B}}, \mathbb{R}^3) \cap H^1(\mathcal{B}, \mathbb{R}^3) \colon \mathbf{u}\big|_\tau \in \mathbb{P}_1(\tau)^3 \ \forall \tau \in \mathcal{T}\} \subset U.$$

is defined. In order to account for the Dirichlet boundary values, we moreover define

$$U_h(\mathbf{u}_\mathrm{D}) = \{\mathbf{u} \in U_h \colon \mathbf{u}(\mathbf{z}) = \mathbf{u}_\mathrm{D}(\mathbf{z}) \ \text{ for all nodal points } \mathbf{z} \in \partial_\mathrm{D}\mathcal{B}\}.$$

Then the solution $\mathbf{u} \in \mathbf{u}_\mathrm{D} + U(\mathbf{0})$ of the weak formulation (6.2) is approximated by $\mathbf{u}_h \in U_h(\mathbf{u}_\mathrm{D})$ satisfying

$$\big(\mathbb{C}[\boldsymbol{\varepsilon}(\mathbf{u}_h) - \boldsymbol{\varepsilon}^\mathrm{pl}], \boldsymbol{\varepsilon}(\boldsymbol{\varphi}_h)\big)_\mathcal{B} = (\mathbf{b}_\mathcal{B}, \boldsymbol{\varphi}_h)_\mathcal{B} + (\mathbf{t}_\mathrm{N}, \boldsymbol{\varphi}_h)_{\partial_\mathrm{N}\mathcal{B}} \quad \text{for all} \quad \boldsymbol{\varphi}_h \in U_h(\mathbf{0})\,.$$

Remark. The numerical approximation can be directly transferred to polynomials of higher degree by simply modifying the definition of the ansatz space U_h. Throughout this work, however, we limit ourselves to trilinear shape functions.

6.2 Approximation of the fully-coupled model

While we use a conforming ansatz space U_h for the approximation of the macroscopic problem, the ansatz spaces V_h and W_h for the approximation of the CDD system are discontinuous. For the coupling of both solution schemes, we define a transfer operator mapping from W_h to

$$\widetilde{U}_h = \{u \in C(\overline{\mathcal{B}}, \mathbb{R}) \cap H^1(\mathcal{B}, \mathbb{R}) \colon u\big|_\tau \in \mathbb{P}_1(\tau) \ \forall \tau \in \mathcal{T}\}.$$

Let $y_h \in W_h$. Given the set of mesh corners $\{\mathbf{c}_h^1, \dots, \mathbf{c}_h^H\}$ and the finite element basis $\{\phi_h^1, \dots, \phi_h^H\}$ of $\widetilde{U}_h$ satisfying $\phi_h^i(\mathbf{c}_h^j) = \delta_{ij}$, we compute coefficients

$$\alpha_h^i(y_h) = \Big(\int_\mathcal{B} \phi_h^i(\mathbf{x})\,\mathrm{d}\mathbf{x}\Big)^{-1} \int_\mathcal{B} y_h(\mathbf{x})\phi_h^i(\mathbf{x})\,\mathrm{d}\mathbf{x} \qquad \text{for } i = 1, \dots, H$$

by convolution with the ansatz functions ϕ_h^i. This allows to define the transfer operator

$$\langle\cdot\rangle_h \colon W_h \to \widetilde{U}_h, \qquad y_h \mapsto \sum_{i=1}^{H} \alpha_h^i(y_h)\phi_h^i.$$

The transfer operator describes an averaging in the support of the finite element basis functions ϕ_h^i which is by construction related to the mesh width h.

6.2.1 Evaluation of the velocity law

In order to approximate the coupled model, we need to evaluate the velocity law (4.9) for each slip system $s = 1, \dots, S$ based on an approximation $\mathbf{u}_h \in U_h(\mathbf{u}_\mathrm{D})$ of the displacement function and approximations $(\rho_{s,h}, \boldsymbol{\kappa}_{s,h}) \in V_h$ of the dislocation densities.

Using the transfer operator $\langle \cdot \rangle_h$, we compute $\bar{\mathbf{w}}_{s,h} = (\bar{\rho}_{s,h}, \bar{\boldsymbol{\kappa}}_{s,h})$ by

$$\bar{\rho}_{s,h} = \langle \rho_{s,h} \rangle_h \qquad \text{and} \qquad \bar{\boldsymbol{\kappa}}_{s,h} = \langle \boldsymbol{\kappa}_{s,h} \cdot \mathbf{d}_s \rangle_h \mathbf{d}_s + \langle \boldsymbol{\kappa}_{s,h} \cdot \mathbf{l}_s \rangle_h \mathbf{l}_s .$$

This allows to evaluate the yield stress (4.10) by

$$\bar{\tau}^\mathrm{y}_{s,h}(\bar{\rho}_{1,h}, \dots, \bar{\rho}_{S,h}) = \mu b_s \sqrt{\sum_{n=1}^{S} a_{sn} \bar{\rho}_{n,h}} \, .$$

For the evaluation of the back stress, we need to compute $\nabla \cdot \boldsymbol{\kappa}^\perp_{s,h}$, $s = 1, \dots, S$. Using the continuous approximation $\bar{\boldsymbol{\kappa}}^\perp_{s,h} = \bar{\boldsymbol{\kappa}}_{s,h} \times \mathbf{m}_s$ we can cell-wise evaluate $\nabla \cdot \bar{\boldsymbol{\kappa}}^\perp_{s,h}|_\tau$ for $\tau \in \mathcal{T}$. This allows to approximate the back stress $\bar{\tau}^\mathrm{b}_{s,h} \in \widetilde{U}_h$ via

$$\bar{\tau}^\mathrm{b}_{s,h} = (D \mu b_s) \Big\langle (\bar{\rho}_{s,h})^{-1} \nabla \cdot \bar{\boldsymbol{\kappa}}^\perp_{s,h} \Big\rangle_h .$$

For a given plastic slip $\bar{\gamma}_{s,h} \in \widetilde{U}_h$, the approximated plastic part of the strain tensor is obtained by

$$\bar{\boldsymbol{\varepsilon}}^\mathrm{pl}_h = \sum_{s=1}^{S} \bar{\gamma}_{s,h} \operatorname{sym}(\mathbf{m}_s \otimes \mathbf{d}_s) \, .$$

By construction, $\mathbf{u}_h\big|_\tau \in C^1(\tau, \mathbb{R}^3)$. Hence, locally we can compute the approximated infinitesimal strain tensor $\boldsymbol{\varepsilon}_h\big|_\tau \in C(\tau, \mathbb{R}^{3\times 3})$ by

$$\boldsymbol{\varepsilon}_h\big|_\tau = \operatorname{sym}(\nabla \mathbf{u}_h\big|_\tau) \, .$$

The extension $\boldsymbol{\varepsilon}_h \colon \mathcal{B} \to \mathbb{R}^{3\times 3}$ is in general discontinuous on the cell interfaces $\mathcal{F}_\tau$ and so is the approximated shear stress

$$\tau^\mathrm{res}_{s,h} = \mathbb{C}[\boldsymbol{\varepsilon}_h - \bar{\boldsymbol{\varepsilon}}^\mathrm{pl}_h] : (\mathbf{m}_s \otimes \mathbf{d}_s).$$

We compute the effective stress in the slip system s by

$$\tau^\mathrm{eff}_{s,h} = \tau^\mathrm{res}_{s,h} - \bar{\tau}^\mathrm{b}_{s,h}.$$

Finally, the approximated dislocation velocity $\bar{v}_{s,h} \in \widetilde{U}_h$ is obtained by

$$\bar{v}_{s,h} = \frac{b_s}{B} \Big\langle \operatorname{sgn}(\tau^{\text{eff}}_{s,h}) \max\left\{0, |\tau^{\text{eff}}_{s,h}| - \tau^{\text{y}}_{s,h}\right\} \Big\rangle_h .$$

Remark. The driving forces for dislocation density mobility can be approximated by a spatial averaging of the elastic energy of the discrete dislocation system (Zaiser, 2015). Thus this kind of averaging process for the evaluation of the velocity law is physically reasonable.

6.2.2 Coupling

For the approximation of the fully-coupled model, the macroscopic problem and the CDD evolution are coupled explicitly. In the macroscopic problem the external load – i.e. body force $\mathbf{b}_{\mathcal{B}}$, traction $\mathbf{t}_{\text{N}}$ and Dirichlet boundary values $\mathbf{u}_{\text{D}}$ – is imposed gradually by introducing a virtual time t

$$-\operatorname{div} \boldsymbol{\sigma}(\mathbf{u}) = \mathbf{b}_{\mathcal{B}}(t) \;\text{ in } \mathcal{B}, \qquad \mathbf{u} = \mathbf{u}_{\text{D}}(t) \;\text{ on } \partial_{\text{D}}\mathcal{B}, \qquad \boldsymbol{\sigma}(\mathbf{u})\mathbf{n} = \mathbf{t}_{\text{N}}(t) \;\text{ on } \partial_{\text{N}}\mathcal{B}. \tag{6.3}$$

We usually apply the external load linearly, i.e.

$$\mathbf{b}_{\mathcal{B}}(t) = t\,\mathbf{b}_{\mathcal{B}}, \qquad \mathbf{u}_{\text{D}}(t) = t\,\mathbf{u}_{\text{D}}, \qquad \text{and} \qquad \mathbf{t}_{\text{N}} = t\,\mathbf{t}_{\text{N}},$$

and consider a time interval $[0, T]$ discretized into equidistant time steps $[t_n, t_{n+1}]$ with $t_n = n\triangle t$, $n = 0, \ldots, N$, $\triangle t = \frac{T}{N}$.

For time $t = t_n$ the macroscopic problem (6.3) is solved approximately using the method presented in Section 6.1. Thereafter the dislocation velocity $\bar{v}^n_{s,h}$ at time t_n is evaluated as described in Section 6.2.1.

If $\bar{v}^n_{s,h}$ vanishes, we can skip the CDD evolution. Otherwise the velocity $\bar{v}^n_{s,h}$ is fixed and we perform M time steps with step size $\triangle t_{\text{cdd}} = \frac{\triangle t}{M}$ on $[t_n, t_{n+1}]$ of the CDD evolution for each slip system computing averaged approximations

$$\bar{\rho}^{\,n+\frac{m}{M}}_{s,h} \approx \rho_s(t_n + m\triangle t_{\text{cdd}}) \qquad \text{for } m = 1, \ldots, M.$$

This allows to evaluate the plastic slip via Orowan's equation (4.7). For each slip system $s = 1, \ldots, S$ we compute the plastic slip $\bar{\gamma}_{s,h}$ explicitly by

$$\bar{\gamma}^{\,n+\frac{m}{M}}_{s,h} = \bar{\gamma}^n_{s,h} + \triangle t_{\text{cdd}} b_s \bar{v}^n_{s,h} \bar{\rho}^{\,n+\frac{m}{M}}_{s,h} \qquad \text{for } m = 1, \ldots, M.$$

Based on $\bar{\gamma}_{s,h}^{n+1}$, $s = 1, \ldots, S$, the plastic part of the strain tensor is updated. With $\bar{\varepsilon}^{\mathrm{pl},n+1}$ we restart by solving (6.3) for $t = t_{n+1}$, i.e. find $\mathbf{u}_h^{n+1} \in U_h(\mathbf{u}_{\mathrm{D}}(t_{n+1}))$ such that

$$\left(\mathbb{C}[\boldsymbol{\varepsilon}(\mathbf{u}_h^{n+1}) - \boldsymbol{\varepsilon}_h^{\mathrm{pl},n+1}], \boldsymbol{\varepsilon}(\boldsymbol{\varphi}_h)\right)_{\mathcal{B}} = (\mathbf{b}_{\mathcal{B}}(t_{n+1}), \boldsymbol{\varphi}_h)_{\mathcal{B}} + (\mathbf{t}_{\mathrm{N}}(t_{n+1}), \boldsymbol{\varphi}_h)_{\partial_{\mathrm{D}}\mathcal{B}} \quad \text{for all } \boldsymbol{\varphi}_h \in U_h(\mathbf{0}).$$

A flow chart summarizing the full algorithm is depicted in Figure 6.1.

Remark. Since the explicit coupling limits the time step size, an implicit coupling is often used for similar elastoplasticity formulations. For our purposes, the limitation is not an issue because we anyway use rather small time steps.

6.3 Extension to polycrystals

The numerical solution method for single crystals can be extended in a straightforward way to polycrystals. For this purpose, we consider a polycrystal $\mathcal{B}$ consisting of G (disjoint) single-crystalline grains $\mathcal{B}_g$, $g = 1, \ldots, G$, i.e.

$$\overline{\mathcal{B}} = \bigcup_{g=1}^{G} \overline{\mathcal{B}}_g.$$

The grains are assumed to be bounded Lipschitz domains. They are each determined by slip systems $(\mathbf{d}_{g,s}, \mathbf{l}_{g,s}, \mathbf{m}_{g,s})$ with Burgers size $b_{g,s}$ for $s = 1, \ldots, S$.

The skeleton of the polycrystal $\partial\mathcal{B} = \partial_{\mathrm{D}}\mathcal{B} \cup \partial_{\mathrm{N}}\mathcal{B} \cup \partial_{\mathrm{I}}\mathcal{B}$ consists of the Dirichlet and Neumann parts $\partial_{\mathrm{D}}\mathcal{B} \cup \partial_{\mathrm{N}}\mathcal{B} = \partial\overline{\mathcal{B}}$ of the domain boundary and the interfaces $\partial_{\mathrm{I}}\mathcal{B} = \bigcup_{g<g'} \partial\mathcal{B}_g \cap \partial\mathcal{B}_{g'}$. The interfaces $\partial_{\mathrm{I}}\mathcal{B}$ correspond to the grain boundaries. We choose the mesh for the space discretization such that $\partial_{\mathrm{I}}\mathcal{B}$ consists of mesh faces. Hence, there is a set of faces $\mathcal{F}_{\mathrm{I}} \subset \bigcup_{\tau\in\mathcal{T}} \mathcal{F}_\tau$ such that

$$\partial_{\mathrm{I}}\mathcal{B} = \bigcup_{f\in\mathcal{F}_{\mathrm{I}}} f.$$

Consequently, each grain $\mathcal{B}_g$, $g = 1, \ldots, G$, consists of mesh cells. Thus there exist subsets $\mathcal{T}_g \subset \mathcal{T}$ of the grid such that

$$\overline{\mathcal{B}}_g = \bigcup_{\tau\in\mathcal{T}_g} \overline{\tau}$$

for $g = 1, \ldots, G$.

This allows to formulate (and discretize) the CDD system in each grain and each slip system separately. The approximations of $\rho_{g,s}$, $\boldsymbol{\kappa}_{g,s}$ and $q_{g,s}$ in $[0,T] \times \mathcal{B}_g$ for $g = 1, \ldots, G$ and $s = 1, \ldots, S$ are computed following the strategies presented in Chapter 5. The grain

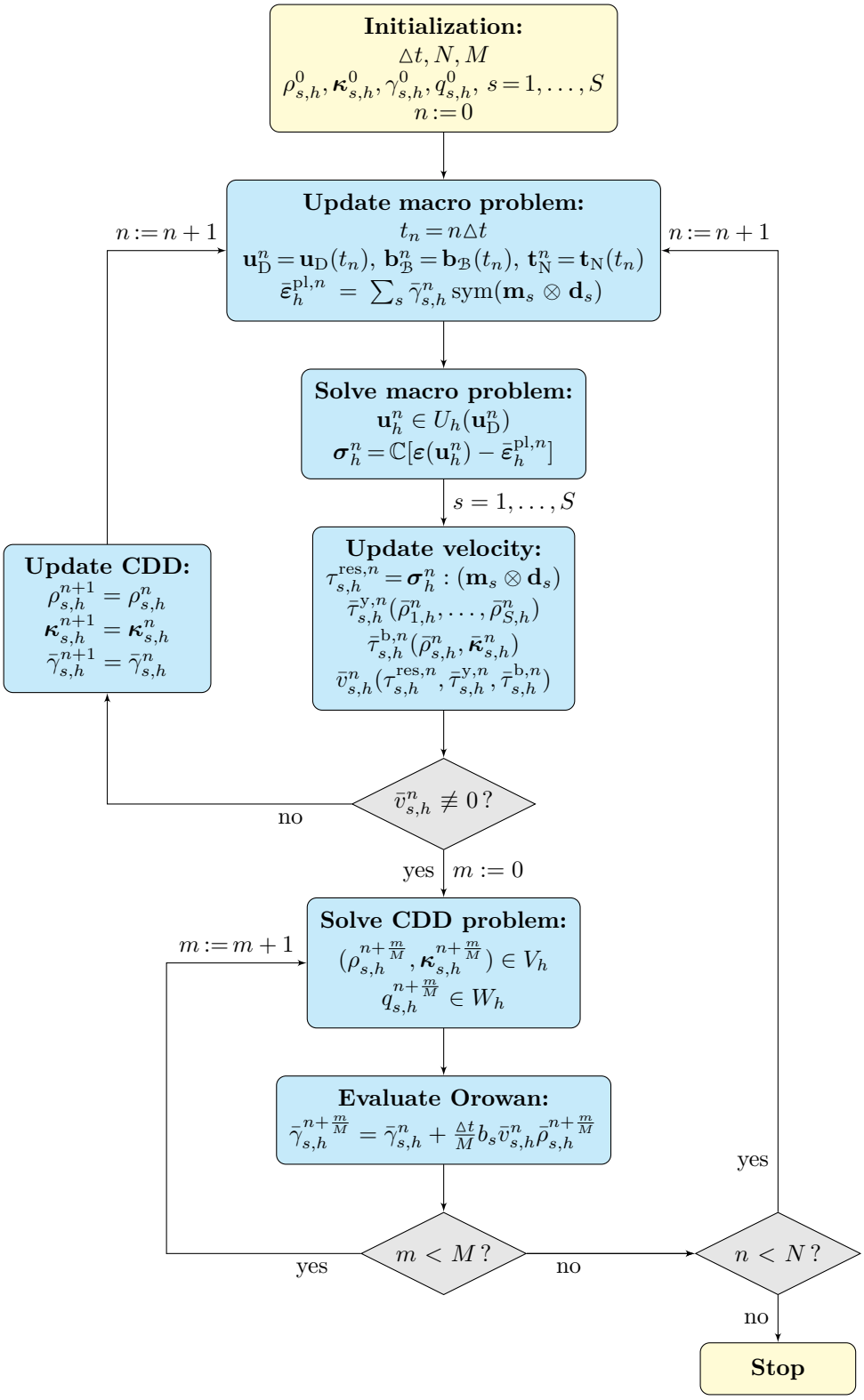

Figure 6.1: Algorithm for the fully-coupled elastoplasticity model

boundaries are realized by specifying impenetrable boundary condition on $\partial\mathcal{B}_g \cap \partial_1\mathcal{B}$ for each grain $\mathcal{B}_g$, cf. Section 5.3.3 and 5.4.3.

Using Orowan's equation (4.7), in each grain $\mathcal{B}_g$, $g = 1, \ldots, G$, the plastic slip $\bar{\gamma}_{g,s}$ is obtained for $s = 1, \ldots, S$. Then the plastic part of the strain tensor is evaluated in each grain $\mathcal{B}_g$ by

$$\bar{\varepsilon}^{\mathrm{pl}}\big|_{\mathcal{B}_g} = \sum_{s=1}^{S} \bar{\gamma}_{g,s}\, \mathrm{sym}(\mathbf{m}_{g,s} \otimes \mathbf{d}_{g,s})\,.$$

Thereafter it can be proceeded as previously to solve the macroscopic problem. Then again the velocity law can be evaluated in each grain and slip system separately.

Altogether the strategies presented here give a numerical approximation scheme for the fully-coupled elastoplasticity model in a polycrystal where the plastic slip is computed by solving the corresponding CDD system in each grain and slip system independently.

6.4 Implementation

For the implementation of the solution method for the fully-coupled model the parallel finite element system M++ (Wieners, 2005, 2010) has been used. M++ is a C++ library allowing for a flexible realization of finite element methods. It includes a wide range of linear solvers, preconditioners, time integrators and quadrature formulae.

In the following, we give some remarks concerning the implementation which we deem noteworthy.

6.4.1 Parallelization

The M++ library includes a parallel programming model which allows to distribute the working load to multiple processes which can be performed in parallel. The communication between different processes is realized using the MPI standard.

The parallelization is based on a distribution of the spatial mesh cells to different cores which is obtained using a recursive coordinate bisection. By this means, to each process a (connected) set of mesh cells is allocated.

The evaluation of numerical fluxes within a discontinuous Galerkin method requires the access to values in adjacent cells. If a neighboring cell is allocated on a different process these are not available on the current process. The implementation of the discontinuous Galerkin method included in M++ resolves this issue by adding virtual cells which are copies of the cells located directly at a process boundary.

6.4.2 Linear solver

Writing the searched quantities and the test functions as linear combination of the basis functions of the respective finite element ansatz space, the weak formulations of the macroscopic as well as of the CDD problem can be formulated as systems of linear equations. The corresponding matrices are by construction sparse. We solve the systems of linear equations iteratively using the GMRES method (Saad and Schultz, 1986). We use a block-diagonal preconditioning based on the Jacobi method.

6.4.3 Avoidance of physically unreasonable values

In order to obtain physically meaningful quantities, it is recommendable to supplement the solution scheme for the CDD system by minor adjustments. Neither the (truncated) CDD evolution equations theirselves nor the (non-monotone) discontinuous Galerkin method guarantee that the physically natural conditions

$$\rho \geq 0 \qquad \text{and} \qquad \rho \geq |\boldsymbol{\kappa}|$$

are satisfied. To be physically correct one might set

$$\begin{aligned} \rho_h &:= \max\{\rho_h, 0\} \\ \boldsymbol{\kappa}_h &:= \min\left\{1, \frac{\rho_h}{|\boldsymbol{\kappa}_h|}\right\}\boldsymbol{\kappa}_h, \end{aligned}$$

e.g. after every time step.

6.4.4 Upwind flux

In the following, we give a practical advice for the implementation of the upwind flux for the first sub-problem (5.2) of the CDD system as presented in Section 5.3.2.

The flux matrix $\mathbf{B_n}$ defined in Equation (5.11) can be written in terms of the corresponding eigenvectors as

$$\mathbf{B_n} = \mathbf{B_n^+} + \mathbf{B_n^-}$$

with the matrices

$$\mathbf{B_n^+} = \frac{1}{2c}\mathbf{v}^+ \otimes \mathbf{v}^+ \qquad \text{and} \qquad \mathbf{B_n^-} = -\frac{1}{2c}\mathbf{v}^- \otimes \mathbf{v}^-.$$

Using this decomposition, we obtain

$$\begin{aligned}\mathbf{B_n}(\mathbf{w}^- + \zeta\mathbf{v}^-) &= \mathbf{B_n^+}\mathbf{w}^- + \mathbf{B_n^-}\mathbf{w}^- + \zeta\mathbf{B_n^-}\mathbf{v}^- \\ &= \mathbf{B_n^+}\mathbf{w}^- + \mathbf{B_n^-}\mathbf{w}^- - \zeta c\mathbf{v}^-.\end{aligned}$$

Inserting ζ from Equation (5.15) gives

$$\begin{aligned}\mathbf{B_n}(\mathbf{w}^- + \zeta\mathbf{v}^-) &= \mathbf{B_n^+}\mathbf{w}^- + \mathbf{B_n^-}\mathbf{w}^- - \frac{1}{2c}(\mathbf{w}^+ - \mathbf{w}^-)\cdot\mathbf{v}^-\mathbf{v}^- \\ &= \mathbf{B_n^+}\mathbf{w}^- + \mathbf{B_n^-}\mathbf{w}^+.\end{aligned}$$

This expression is convenient to implement the upwind flux on inner faces and can be used as well on boundary faces. For the free outflow boundary we obtain e.g. directly

$$\mathbf{B_n}(\mathbf{w}^- + \zeta\mathbf{v}^-) = \mathbf{B_n^+}\mathbf{w}^-$$

by setting $\mathbf{w}^+ = \mathbf{0}$.

CHAPTER 7
Validation of the approximation scheme

This chapter is dedicated to the numerical validation of the approximation scheme presented in Chapter 5 and 6. For this purpose, we investigate the approximation of the CDD system and of the macroscopic problem separately. For some special situations, analytical solutions of the CDD system can be derived. We provide two solutions of the CDD evolution equations and specify numerical test configurations for both. These are used to examine the convergence behavior of the space and the time discretization. The numerical approximation method for the macroscopic problem is validated using the analytical eigenstresses of straight discrete dislocations of pure screw or edge type given in Section 3.7. We show how the stress fields of discrete dislocations can be transferred to the continuum framework. Then we define numerical test settings for the macroscopic problem and give a comparison of the numerical results with reference data based on the known eigenstresses.

7.1 CDD system

Analytical solutions of the CDD system (4.8) can be derived for simplified velocity laws. For a numerical convergence analysis of the approximation method, the special cases of in space constant and in space linear dislocation velocity are examined. We analyze the convergence behavior in time for the different splittings presented in Section 5.1. For the convergence in space, the numerical solutions in the discontinuous Galerkin ansatz spaces with polynomial degrees $0, 1$ and 2 are compared.

All numerical tests in this section are executed for a single slip system. Accordingly, the index s denoting the slip system is omitted throughout this section.

We need to specify an error measure for the comparison of our numerical results with exact solutions of the CDD system. Given an analytical solution u and a numerical approximation u_h in a discontinuous Galerkin space based on a triangulation $\mathcal{T}$ of $\mathcal{B}$, we use the L^2-norm as

error measure. It is approximated numerically using a Gaussian quadrature rule $(\boldsymbol{\xi}_n, w_n)_n$ in a reference cell by

$$\begin{aligned}\|u - u_h\| &= \Big(\sum_{\tau \in \mathcal{T}} \int_\tau (u(\mathbf{x}) - u_h(\mathbf{x}))^2 \,\mathrm{d}\mathbf{x} \Big)^{\frac{1}{2}} \\ &\approx \Big(\sum_{\tau \in \mathcal{T}} \sum_n w_n \det(\mathbf{J}^\tau(\boldsymbol{\xi}_n)) (u(\mathbf{x}^\tau(\boldsymbol{\xi}_n)) - u_h(\mathbf{x}^\tau(\boldsymbol{\xi}_n)))^2 \Big)^{\frac{1}{2}}\end{aligned}$$

with $\mathbf{x}^\tau$ denoting the coordinate transformation from the reference cell to the cell $\tau \in \mathcal{T}$ and $\mathbf{J}^\tau$ being its Jacobian.

7.1.1 Constant velocity

In Section 5.3.3 a traveling wave solution for constant velocity $v \equiv v_0$ and vanishing curvature density $q \equiv 0$ has been given. Using a similar approach, radial traveling wave solutions with non-zero curvature density can be deduced.

Let for this purpose $\mathbf{r} = (\mathbf{x} \cdot \mathbf{d})\mathbf{d} + (\mathbf{x} \cdot \mathbf{l})\mathbf{l}$ be the projection of a point $\mathbf{x} \in \mathcal{B}$ onto the slip plane $\Gamma = \operatorname{span}\{\mathbf{d}, \mathbf{l}\}$ and $r = |\mathbf{r}|$ denote the radial distance from the origin. Let furthermore $z = \mathbf{x} \cdot \mathbf{m}$ denote the deviation in slip normal direction, and let $P \colon \mathbb{R}^3 \to [0, \infty)$ be a given amplitude function satisfying

$$\partial_t P(t, r, z) = -v_0 \, \partial_r P(t, r, z) \qquad \text{for all } (t, r, z) \in \mathbb{R}^3 \tag{7.1}$$

where $v_0 \in \mathbb{R}$ is given. We show that then a solution of the CDD system (4.8) with constant velocity v_0 is given by

$$\rho(t, \mathbf{x}) = P(t, r, z) \tag{7.2a}$$

$$\boldsymbol{\kappa}(t, \mathbf{x}) = \rho(t, \mathbf{x}) \mathbf{m} \times \frac{\mathbf{r}}{r} \tag{7.2b}$$

$$q(t, \mathbf{x}) = \frac{1}{r} \rho(t, \mathbf{x}) \tag{7.2c}$$

with initial values $\rho(0, \cdot\,)$, $\boldsymbol{\kappa}(0, \cdot\,)$ and $q(0, \cdot\,)$.

We verify that (7.2) is a solution by inserting into the right-hand side of the CDD system (4.8) and exploiting

$$\nabla \cdot \left(\frac{\mathbf{r}}{r} \right) = \frac{1}{r} \quad \text{and} \quad \nabla \cdot \left(\frac{\mathbf{r}}{r^2} \right) = 0$$

as well as the relation (7.1).

For the first equation (4.8a), we obtain

$$\begin{aligned}-\nabla\cdot(v_0\boldsymbol{\kappa}^\perp)+v_0q &= -\nabla\cdot\left(v_0\left(P\mathbf{m}\times\frac{\mathbf{r}}{r}\right)\times\mathbf{m}\right)+v_0\frac{P}{r} = -\nabla\cdot\left(v_0P\frac{\mathbf{r}}{r}\right)+v_0\frac{P}{r}\\ &= -v_0\left(\nabla P\cdot\frac{\mathbf{r}}{r}+P\nabla\cdot\frac{\mathbf{r}}{r}\right)+v_0\frac{P}{r} = -v_0\left(\partial_rP+\frac{P}{r}\right)+v_0\frac{P}{r}\\ &= \partial_tP=\partial_t\rho.\end{aligned}$$

Inserting into the second equation (4.8b) yields

$$\begin{aligned}\nabla\times(v_0\rho\mathbf{m}) &= -v_0\,\mathbf{m}\times\nabla\rho = -v_0\,\mathbf{m}\times\left(\partial_rP\frac{\mathbf{r}}{r}+\partial_zP\mathbf{m}\right)\\ &= -v_0\partial_rP\,\mathbf{m}\times\frac{\mathbf{r}}{r} = \partial_tP\,\mathbf{m}\times\frac{\mathbf{r}}{r} = \partial_t\boldsymbol{\kappa}.\end{aligned}$$

Finally, the third equation (4.8c) gives

$$\begin{aligned}-\nabla\cdot\left(v_0\frac{q}{\rho}\boldsymbol{\kappa}^\perp\right) &= -\nabla\cdot\left(\frac{v_0}{r}\left(P\mathbf{m}\times\frac{\mathbf{r}}{r}\right)\times\mathbf{m}\right) = -\nabla\cdot\left(v_0\frac{P}{r^2}\mathbf{r}\right)\\ &= -v_0\left(\nabla\cdot\left(\frac{\mathbf{r}}{r^2}\right)P+\nabla P\cdot\frac{\mathbf{r}}{r^2}\right) = -v_0\nabla P\cdot\frac{\mathbf{r}}{r^2}\\ &= -v_0\left(\partial_rP\frac{\mathbf{r}}{r}+\partial_zP\mathbf{m}\right)\cdot\frac{\mathbf{r}}{r^2} = -v_0\frac{\partial_rP}{r} = \frac{\partial_tP}{r} = \partial_tq.\end{aligned}$$

Hence, for an appropriate choice of P, Equation (7.2) is indeed a solution of the CDD system with constant dislocation velocity v_0. Unlike the traveling wave solution (5.20) this solution involves a non-vanishing curvature density. It is therefore more suitable for a benchmark test.

For the amplitude function P we choose a normal distribution in $\mathbf{r}$- and $\mathbf{m}$-direction

$$P(t,r,z)=\frac{1}{2\pi s_rs_z}\exp\!\left(-\frac{1}{2s_r^2}(r-R(t))^2-\frac{1}{2s_z^2}z^2\right)$$

with radius $R(t)=R_0+v_0t$ and standard deviations $s_r,s_z>0$. The required relation $\partial_tP=-v_0\partial_rP$ is fulfilled for this choice of P. Thus (7.2) solves the CDD system for initial values $\rho(0,\cdot)$, $\boldsymbol{\kappa}(0,\cdot)$ and $q(0,\cdot)$.

This is a continuum formulation of a perfectly circular dislocation loop with initial radius R_0. In the limit case $s_r,s_z\longrightarrow 0$ the discrete representation of a dislocation loop is obtained. Since dislocations move perpendicular to their line direction, a dislocation loop subject to a constant stress expands or shrinks. By prescribing a constant dislocation velocity v_0 and a linear dependence in time of the loop radius R, this behavior is captured. A change in the radius induces a change in the total line length of the dislocation. This mechanism is represented in the CDD system by the dislocation density production term v_0q. When

increasing or decreasing the radius, a decreased or increased curvature is obtained since the definition of the curvature density q scales with $\frac{1}{r}$. The described behavior is illustrated in Figure 7.1.

Altogether, this choice of P yields a physical meaningful benchmark test for the approximation of the CDD evolution equations. In the following, a numerical analysis of the time and space convergence is performed. We investigate the time and space convergence separately by either fixing the space mesh width or the time step size and varying the respective other value. For the time convergence, we need a space discretization which is accurate enough that the time error dominates. Therefore, a two-dimensional configuration representing a single slip plane is considered in this case. The space convergence is investigated in a three-dimensional setting.

In both tests, the slip system determined by $\mathbf{d} = \mathbf{e}_1$, $\mathbf{l} = \mathbf{e}_2$ and $\mathbf{m} = \mathbf{e}_3$ is considered. The initial radius is set to $R_0 = 1\,\mu\text{m}$. We compute the numerical solution in the time interval $t \in [0\,\text{ns}, 1\,\text{ns}]$ and compare the L^2-error in ρ and q at $T = 1\,\text{ns}$. The dislocation velocity is chosen to be $v_0 = 1\frac{\mu\text{m}}{\text{ns}}$.

Convergence in time

For the convergence in time, a square geometry

$$\mathcal{B} = [-5\,\mu\text{m}, 5\,\mu\text{m}] \times [-5\,\mu\text{m}, 5\,\mu\text{m}]$$

is considered. It is discretized using an equidistant square grid with mesh width $h = 0.02\,\mu\text{m}$. This corresponds to a total of 250 000 spatial cells. The discontinuous Galerkin ansatz spaces V_h and W_h with polynomial degree $p = 2$ are chosen.

The standard deviation in radial direction $s_r = 0.125\,\mu\text{m}$ is used. In order to reduce the three-dimensional formulation of the dislocation loop to two dimensions we set $s_z = 1\,\mu\text{m}$. We compare the Lie and Strang splitting methods (WQ), (QW), (QWQ) and (WQW) presented in Chapter 5 for time step sizes $\triangle t = 2^{-n}\,\mu\text{m}$ with $n = 4, \ldots, 10$. The resulting convergence plots are shown in Figure 7.2. The corresponding data is summarized in Table 7.1.

We observe that the Strang splittings (QWQ) and (WQW) reproduce the optimal order 2 in a very satisfying way for ρ and q. For the Lie splittings (WQ) and (QW) the order in which the sub-problems are solved has an impact on the observed convergence behavior. Once again the expected order is observed. In summary, the time convergence analysis clearly demonstrates that the Strang splittings are preferable to the lower order Lie splittings.

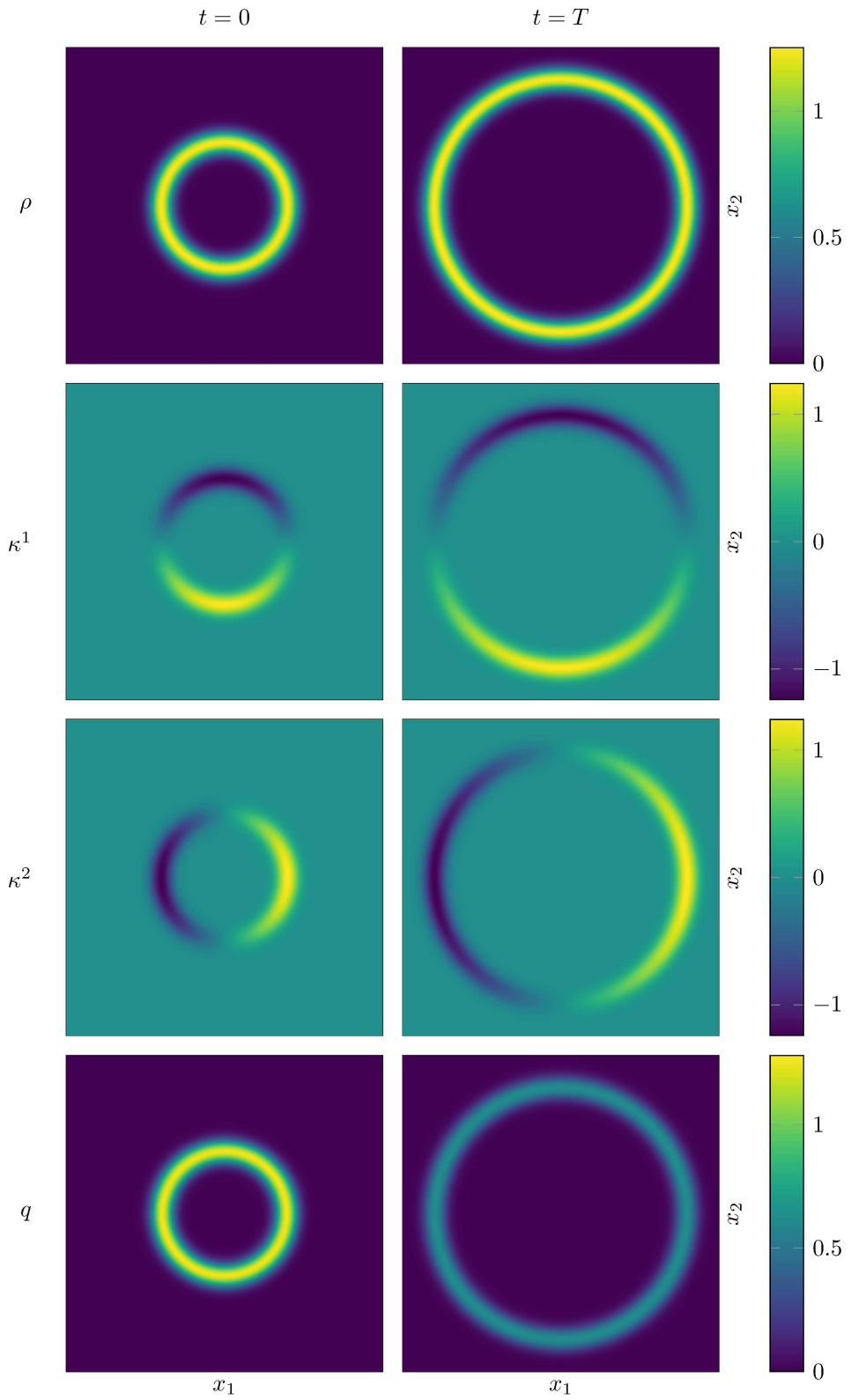

Figure 7.1: Expanding dislocation loop

splitting	N	$\|\rho - \rho_h\|$	rate	$\|q - q_h\|$	rate
(WQ)	16	$4.7830 \cdot 10^{-1}$	–	$2.2537 \cdot 10^{-1}$	–
(WQ)	32	$1.6009 \cdot 10^{-1}$	2.9877	$5.7720 \cdot 10^{-2}$	3.9046
(WQ)	64	$5.3521 \cdot 10^{-2}$	2.9911	$1.4815 \cdot 10^{-2}$	3.8960
(WQ)	128	$1.9941 \cdot 10^{-2}$	2.6839	$3.9779 \cdot 10^{-3}$	3.7243
(WQ)	256	$8.3325 \cdot 10^{-3}$	2.3932	$1.2905 \cdot 10^{-3}$	3.0825
(WQ)	512	$3.7817 \cdot 10^{-3}$	2.2034	$5.3881 \cdot 10^{-4}$	2.3951
(WQ)	1024	$1.8049 \cdot 10^{-3}$	2.0952	$2.5486 \cdot 10^{-4}$	2.1141
(QW)	16	$3.4375 \cdot 10^{-1}$	–	$2.3914 \cdot 10^{-1}$	–
(QW)	32	$8.6478 \cdot 10^{-2}$	3.9750	$7.6479 \cdot 10^{-2}$	3.1269
(QW)	64	$1.9764 \cdot 10^{-2}$	4.3755	$2.4408 \cdot 10^{-2}$	3.1333
(QW)	128	$8.1693 \cdot 10^{-3}$	2.4193	$8.7014 \cdot 10^{-3}$	2.8051
(QW)	256	$4.8299 \cdot 10^{-3}$	1.6914	$3.5346 \cdot 10^{-3}$	2.4618
(QW)	512	$2.6954 \cdot 10^{-3}$	1.7919	$1.6041 \cdot 10^{-3}$	2.2035
(QW)	1024	$1.4149 \cdot 10^{-3}$	1.9050	$7.9507 \cdot 10^{-4}$	2.0175
(QWQ)	16	$4.0391 \cdot 10^{-1}$	–	$2.0974 \cdot 10^{-1}$	–
(QWQ)	32	$1.1626 \cdot 10^{-1}$	3.4743	$5.7240 \cdot 10^{-2}$	3.6642
(QWQ)	64	$3.0024 \cdot 10^{-2}$	3.8721	$1.4876 \cdot 10^{-2}$	3.8478
(QWQ)	128	$7.5813 \cdot 10^{-3}$	3.9603	$3.8090 \cdot 10^{-3}$	3.9055
(QWQ)	256	$1.9172 \cdot 10^{-3}$	3.9544	$1.0095 \cdot 10^{-3}$	3.7732
(QWQ)	512	$4.9661 \cdot 10^{-4}$	3.8605	$3.0574 \cdot 10^{-4}$	3.3018
(QWQ)	1024	$1.4255 \cdot 10^{-4}$	3.4838	$1.3583 \cdot 10^{-4}$	2.2508
(WQW)	16	$3.9035 \cdot 10^{-1}$	–	$2.1670 \cdot 10^{-1}$	–
(WQW)	32	$1.1405 \cdot 10^{-1}$	3.4226	$5.8336 \cdot 10^{-2}$	3.7146
(WQW)	64	$2.9701 \cdot 10^{-2}$	3.8399	$1.4994 \cdot 10^{-2}$	3.8907
(WQW)	128	$7.5292 \cdot 10^{-3}$	3.9448	$3.8147 \cdot 10^{-3}$	3.9305
(WQW)	256	$1.9083 \cdot 10^{-3}$	3.9455	$1.0089 \cdot 10^{-3}$	3.7811
(WQW)	512	$4.9491 \cdot 10^{-4}$	3.8558	$3.0527 \cdot 10^{-4}$	3.3049
(WQW)	1024	$1.4217 \cdot 10^{-4}$	3.4812	$1.3568 \cdot 10^{-4}$	2.2499

Table 7.1: L^2-error data for ρ and q for the expanding loop in dependence of the number of time steps N for different splitting methods

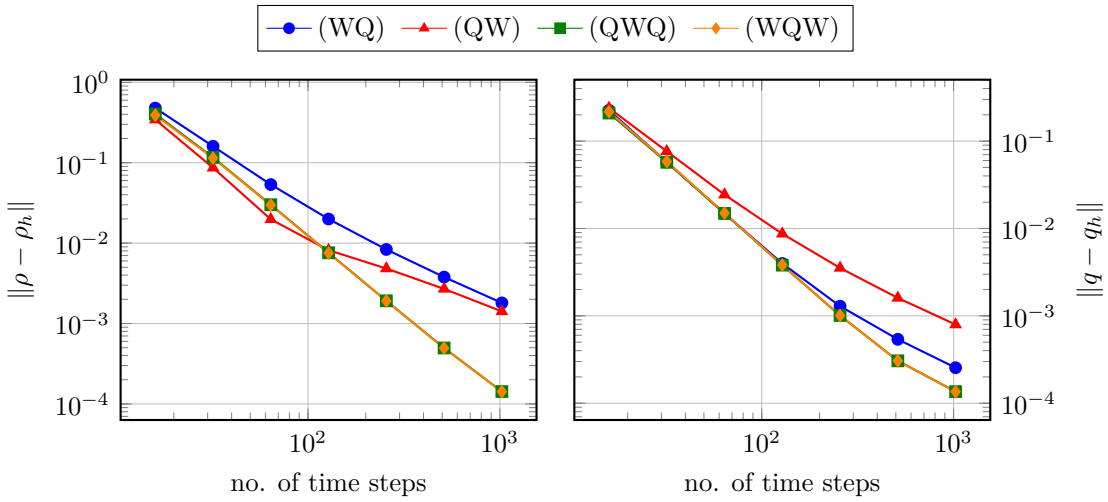

Figure 7.2: L^2-error plot for ρ and q for the expanding loop in dependence of the number of time steps for different splitting methods

Hence, the observations are in excellent accordance with the theoretically expected time convergence behavior.

Convergence in space

For the convergence in space, a cuboid geometry

$$\mathcal{B} = [-2.5\,\mu\text{m}, 2.5\,\mu\text{m}] \times [-2.5\,\mu\text{m}, 2.5\,\mu\text{m}] \times [-1\,\mu\text{m}, 1\,\mu\text{m}]$$

is used. The time discretization is done using the Strang splitting (QWQ) with step size $\triangle t = 2^{-8}$ ns. This means 256 time steps are performed.

We use the standard deviations $s_r = 0.125\,\mu\text{m}$ and $s_z = 0.125\,\mu\text{m}$. We compare the polynomial degrees $p = 0, 1, 2$ for equidistant cubic space grids with mesh widths $h = 2^{-n}\,\mu\text{m}$ for $n \in \mathbb{N}_0$. The resulting convergence plots are given in Figure 7.3. Here, the L^2-error in ρ and q is depicted in dependence of the number of the degrees of freedom in x_1-direction. The corresponding data is specified in Table 7.2.

The observed convergence behavior is very similar for both ρ and q. It is clearly apparent that a higher polynomial degree results in a faster convergence. The respective convergence order which can be deduced from the numerical experiments is slightly lower than the theoretical optimum. With regard to the separate solution of two sub-problems via the splitting and the averaging procedures which we carried out in order to compute the upwind flux, the observed order reduction is not surprising. In any case, this convergence

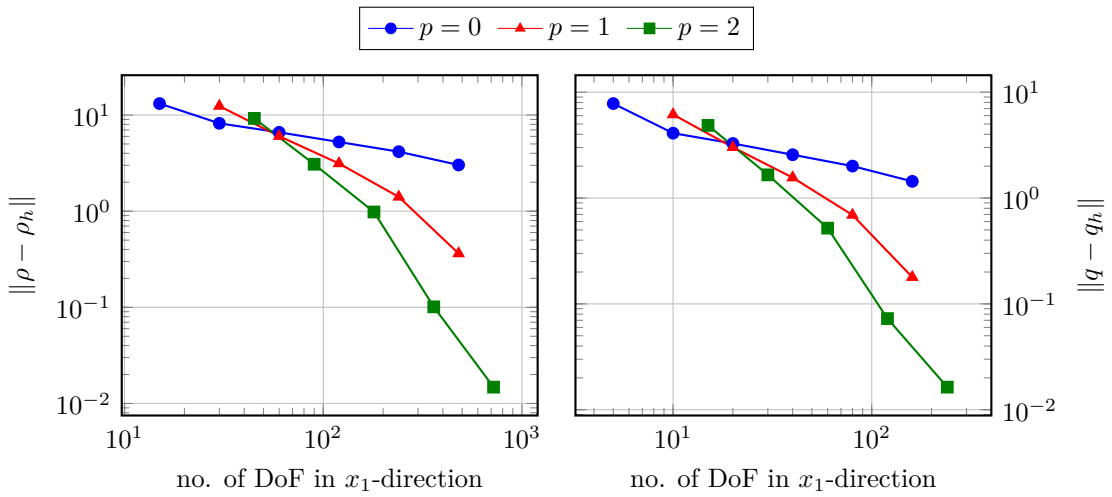

Figure 7.3: L^2-error plot for ρ and q for the expanding loop setting in dependence of the number of degrees of freedom for different polynomial degrees p

p	n	$\|\rho - \rho_h\|$	rate	$\|q - q_h\|$	rate
0	0	$1.3158 \cdot 10^{1}$	–	$7.8082 \cdot 10^{0}$	–
0	1	$8.1954 \cdot 10^{0}$	1.6056	$4.1004 \cdot 10^{0}$	1.9043
0	2	$6.6089 \cdot 10^{0}$	1.2401	$3.2758 \cdot 10^{0}$	1.2517
0	3	$5.2429 \cdot 10^{0}$	1.2605	$2.5651 \cdot 10^{0}$	1.2771
0	4	$4.1566 \cdot 10^{0}$	1.2613	$2.0035 \cdot 10^{0}$	1.2803
0	5	$3.0240 \cdot 10^{0}$	1.3745	$1.4370 \cdot 10^{0}$	1.3942
1	0	$1.2396 \cdot 10^{1}$	–	$6.1545 \cdot 10^{0}$	–
1	1	$6.0261 \cdot 10^{0}$	2.0570	$3.0174 \cdot 10^{0}$	2.0397
1	2	$3.1336 \cdot 10^{0}$	1.9231	$1.5587 \cdot 10^{0}$	1.9358
1	3	$1.4072 \cdot 10^{0}$	2.2268	$6.9140 \cdot 10^{-1}$	2.2544
1	4	$3.6280 \cdot 10^{-1}$	3.8787	$1.7881 \cdot 10^{-1}$	3.8666
2	0	$9.2215 \cdot 10^{0}$	–	$4.8560 \cdot 10^{0}$	–
2	1	$3.0770 \cdot 10^{0}$	2.9969	$1.6561 \cdot 10^{0}$	2.9321
2	2	$9.8082 \cdot 10^{-1}$	3.1372	$5.1950 \cdot 10^{-1}$	3.1879
2	3	$1.0114 \cdot 10^{-1}$	9.6981	$7.2658 \cdot 10^{-2}$	7.1500
2	4	$1.4781 \cdot 10^{-2}$	6.8423	$1.6348 \cdot 10^{-2}$	4.4444

Table 7.2: L^2-error data for ρ and q for the expanding loop setting in dependence of the number of degrees of freedom for different polynomial degrees p with mesh width $h = 2^{-n}$ µm

test demonstrates that discontinuous Galerkin methods with polynomial degree $p > 0$ outperform the classical finite volume method ($p = 0$).

7.1.2 Linear velocity

If the dislocation velocity is constant in space as in the previous section, the curvature density production term $\mathbf{g}(\mathbf{w})$ vanishes for any $\mathbf{w}$. Therefore, the expanding dislocation loop does not incorporate the whole CDD system and is thus not sufficient for a rigorous convergence analysis of the introduced solution method.

For this reason, we subsequently derive an analytical solution of the CDD system (4.8) for a non-constant dislocation velocity v. To this end, a slightly more complicated situation with linear velocity of the form $v = v_0(\mathbf{x} \cdot \mathbf{e})$ with fixed $v_0 > 0$ and $\mathbf{e} \in \mathbb{R}^3$, i.e. $\nabla v = v_0\mathbf{e}$, is considered. We assume $|\mathbf{e}| = 1$ and $\mathbf{e} \cdot \mathbf{m} = 0$.

In order to find a solution of the CDD system with linear velocity, the ansatz

$$\rho(t, \mathbf{x}) = (\mathbf{x} \cdot \mathbf{e})^k \exp(-ct), \qquad k \in \mathbb{N}, c > 0,$$

is used. It yields the relations

$$\partial_t \rho = -c\rho \qquad \text{and} \qquad v\nabla\rho = kv_0\rho\mathbf{e}.$$

Considering the second equation of the CDD system (4.8b), we obtain

$$\begin{aligned}\partial_t \boldsymbol{\kappa} &= \nabla\times(\rho v\mathbf{m}) = -\mathbf{m}\times\nabla(v\rho) = -\mathbf{m}\times(\rho\nabla v + v\nabla\rho)\\ &= -(k+1)v_0\rho\mathbf{m}\times\mathbf{e} = \frac{v_0}{c}(k+1)\partial_t\rho\mathbf{m}\times\mathbf{e}.\end{aligned}$$

Hence, we choose the GND density vector

$$\boldsymbol{\kappa} = \frac{v_0}{c}(k+1)\rho\mathbf{m}\times\mathbf{e}.$$

Consequently, it holds $\boldsymbol{\kappa}^\perp = \boldsymbol{\kappa}\times\mathbf{m} = \frac{v_0}{c}(k+1)\rho\mathbf{e}$. Inserting the definitions for ρ and $\boldsymbol{\kappa}$ into the first equation of the CDD system (4.8a) gives

$$\begin{aligned}vq &= \partial_t\rho + \nabla\cdot(v\boldsymbol{\kappa}^\perp)\\ &= \partial_t\rho + \nabla v\cdot\boldsymbol{\kappa}^\perp + v\nabla\cdot\boldsymbol{\kappa}^\perp\\ &= -c\rho + \frac{v_0^2}{c}(k+1)\rho + \frac{v_0^2}{c}k(k+1)\rho\\ &= \frac{(k+1)^2v_0^2 - c^2}{c}\rho\end{aligned}$$

and induces the choice of the curvature density q. It remains to examine the third equation (4.8c). We obtain for the curvature density production function

$$\begin{aligned}\mathbf{g}(\mathbf{w}) &= \frac{1}{2|\boldsymbol{\kappa}|^2}\Big((\rho+|\boldsymbol{\kappa}|)\boldsymbol{\kappa}\otimes\boldsymbol{\kappa}+(\rho-|\boldsymbol{\kappa}|)\boldsymbol{\kappa}^\perp\otimes\boldsymbol{\kappa}^\perp\Big)v_0\mathbf{e}\\ &= \frac{1}{2|\boldsymbol{\kappa}|^2}\Big((\rho-|\boldsymbol{\kappa}|)\boldsymbol{\kappa}^\perp\otimes\boldsymbol{\kappa}^\perp\Big)v_0\mathbf{e}\\ &= \frac{v_0}{2}(\rho-|\boldsymbol{\kappa}|)\mathbf{e}\\ &= \frac{v_0}{2c}\rho(c-v_0(k+1))\mathbf{e}\,.\end{aligned}$$

Finally, we have

$$\begin{aligned}&v\Big(\partial_t q+\nabla\cdot\Big(\frac{q}{\rho}v\boldsymbol{\kappa}^\perp+\mathbf{g}(\mathbf{w})\Big)\Big)\\ &\quad= v\partial_t q+v\nabla\cdot\left(\frac{(k+1)^2v_0^2-c^2}{c}\boldsymbol{\kappa}^\perp+\frac{cv_0-(k+1)v_0^2}{2c}\rho\mathbf{e}\right)\\ &\quad= \frac{(k+1)^2v_0^2-c^2}{c}\partial_t\rho+\frac{(k+1)^2v_0^2-c^2}{c}v\nabla\cdot\boldsymbol{\kappa}^\perp+\frac{cv_0-(k+1)v_0^2}{2c}v\nabla\rho\cdot\mathbf{e}\\ &\quad= (c^2-(k+1)^2v_0^2)\rho+\frac{(k+1)^2v_0^2-c^2}{c}\frac{v_0}{c}(k+1)kv_0\rho+\frac{v_0c-(k+1)v_0^2}{2c}kv_0\rho\\ &\quad= \frac{\rho}{2c^2}(2c^4-c^2v_0^2(4k^2+5k+2)+2(k+1)^3v_0^4k-cv_0^3(k+1)k)\\ &\quad= \frac{\rho}{2c^2}(c-(k+1)v_0)(2c^3+2c^2(k+1)v_0-c(2k^2v_0^2+kv_0^2)-2v_0^3(k^3+2k^2+k)).\end{aligned}$$

If $v(\partial_t q+\nabla\cdot(\frac{q}{\rho}v\boldsymbol{\kappa}^\perp+\mathbf{g}(\mathbf{w})))=0$ we obtain a solution of the CDD system. In the case $c=(k+1)v_0$ again $\mathbf{g}(\mathbf{w})$ vanishes, for this reason we need to choose c such that

$$2c^3+2c^2(k+1)v_0-c(2k^2v_0^2+kv_0^2)-2v_0^3(k^3+2k^2+k)=0.$$

For the numerical tests, we choose $k=4$ and obtain

$$c=\frac{1}{3}\left(-5+\sqrt[3]{820-3\sqrt{19929}}+\sqrt[3]{820+3\sqrt{19929}}\right)v_0\approx 4.3666\,v_0\,.$$

Note that

$$|\boldsymbol{\kappa}|=\frac{2v_0}{c}(k+1)\rho>\rho$$

which contradicts the definition of the GND density vector $\boldsymbol{\kappa}$. This means this test setting has no physical interpretation. However, it still solves the CDD system and is thus – from a mathematical point of view – interesting as a benchmark test.

As previously for the expanding dislocation loop, we investigate the time and space convergence behavior separately. The square geometry

$$\mathcal{B} = [-1\,\mu\text{m}, 1\,\mu\text{m}]^2$$

is considered for both numerical tests. The slip system determined by $\mathbf{d} = \mathbf{e}_1$, $\mathbf{l} = \mathbf{e}_2$ and $\mathbf{m} = \mathbf{e}_3$ is chosen. We use the dislocation velocity $v = v_0(\mathbf{x} \cdot \mathbf{e})$ with $v_0 = 1\frac{\mu\text{m}}{\text{ns}}$ and $\mathbf{e} = \frac{1}{\sqrt{1.04}}(1, 0.2, 0)^\top$.

See Figure 7.4 for an illustration of the test setting. In order to account for the bounded geometry, a boundary condition on $\partial\mathcal{B}$ needs to be specified. To this end, we prescribe $\mathbf{n} \cdot (\boldsymbol{\kappa} \times \mathbf{m})$ as shown in Section 5.3.3.

Remark. It is clear that a routine ensuring $\rho_h \geq |\boldsymbol{\kappa}_h|$ as proposed in Section 6.4.3 needs to be switched off for this numerical test.

Convergence in time

The geometry is discretized into 262 144 congruent square cells with $h = 2^{-8}\,\mu\text{m}$ for the time convergence analysis. The discontinuous Galerkin ansatz spaces V_h and W_h with polynomial degree $p = 2$ are chosen.

We compute the numerical solutions in the time intervall $[0, 0.5\,\text{ns}]$ and evaluate the L^2-errors for ρ and q at the final time $T = 0.5\,\text{ns}$. We compare the Lie and Strang splitting methods (WQ), (QW), (QWQ) and (WQW) for time step sizes $\triangle t = 2^{-n}\,\text{ns}$ with $n = 3, \ldots, 8$. The resulting L^2-error plots are given in Figure 7.5. The corresponding data is summarized in Table 7.3.

We observe that both the Lie splittings (WQ) and (QW) and the Strang splittings (QWQ) and (WQW) show the respective optimal order 1 and 2 for ρ and q. In comparison to the results for the expanding loop, the difference between the Lie splittings (WQ) and (QW) is smaller. For ρ and q, (QW) gives a slightly smaller error than (WQ). Overall, the time convergence investigation for the linear velocity test confirms the observations for the expanding loop with constant velocity.

Convergence in space

For the convergence in space, the time discretization is done using the Strang splitting (QWQ) where the time interval $[0, 1\,\text{ns}]$ is discretized into 2 048 equidistant time steps with step size $\triangle t = 2^{-11}\,\text{ns}$.

We compare the polynomial degrees $p = 0, 1, 2$ for equidistant square space grids with mesh widths $h = 2^{-n}\,\mu\text{m}$ for $n \in \mathbb{N}, n \geq 3$. The resulting convergence plots are given in

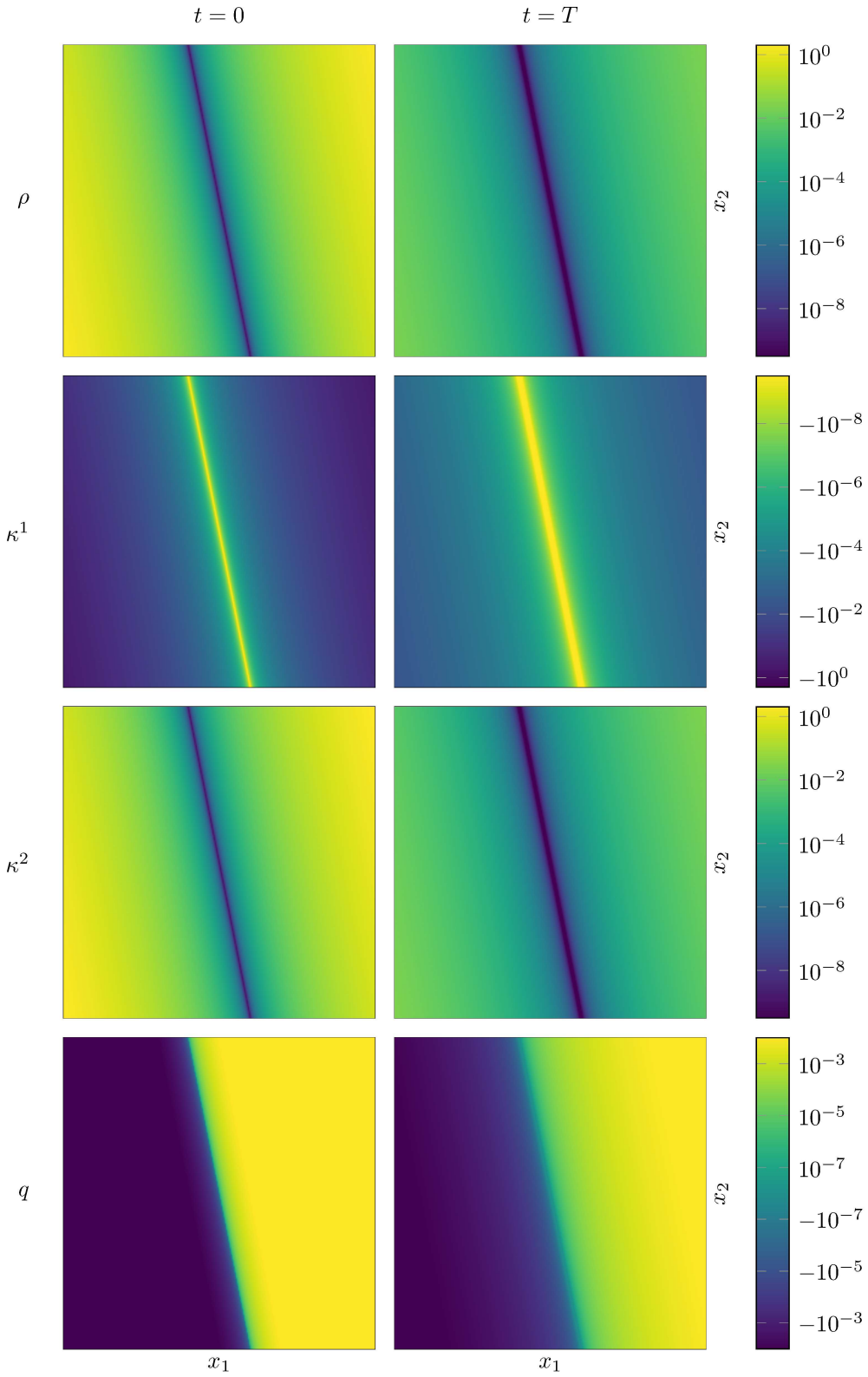

Figure 7.4: Linear velocity setting

splitting	N	$\|\rho - \rho_h\|$	rate	$\|q - q_h\|$	rate
(WQ)	8	$3.1440 \cdot 10^{-2}$	–	$2.8805 \cdot 10^{-2}$	–
(WQ)	16	$1.3966 \cdot 10^{-2}$	2.2512	$1.2084 \cdot 10^{-2}$	2.3837
(WQ)	32	$6.5698 \cdot 10^{-3}$	2.1258	$5.6375 \cdot 10^{-3}$	2.1435
(WQ)	64	$3.1860 \cdot 10^{-3}$	2.0621	$2.7152 \cdot 10^{-3}$	2.0763
(WQ)	128	$1.5687 \cdot 10^{-3}$	2.0310	$1.3308 \cdot 10^{-3}$	2.0403
(WQ)	256	$7.7808 \cdot 10^{-4}$	2.0161	$6.5849 \cdot 10^{-4}$	2.0210
(QW)	8	$2.0222 \cdot 10^{-2}$	–	$1.8421 \cdot 10^{-2}$	–
(QW)	16	$1.1055 \cdot 10^{-2}$	1.8292	$8.8509 \cdot 10^{-3}$	2.0813
(QW)	32	$5.8357 \cdot 10^{-3}$	1.8944	$4.7835 \cdot 10^{-3}$	1.8503
(QW)	64	$3.0032 \cdot 10^{-3}$	1.9432	$2.4986 \cdot 10^{-3}$	1.9145
(QW)	128	$1.5242 \cdot 10^{-3}$	1.9704	$1.2769 \cdot 10^{-3}$	1.9567
(QW)	256	$7.6814 \cdot 10^{-4}$	1.9842	$6.4552 \cdot 10^{-4}$	1.9781
(QWQ)	8	$7.7216 \cdot 10^{-3}$	–	$1.0896 \cdot 10^{-2}$	–
(QWQ)	16	$1.9991 \cdot 10^{-3}$	3.8625	$2.2429 \cdot 10^{-3}$	4.8581
(QWQ)	32	$5.0750 \cdot 10^{-4}$	3.9391	$5.9712 \cdot 10^{-4}$	3.7561
(QWQ)	64	$1.2695 \cdot 10^{-4}$	3.9976	$1.5398 \cdot 10^{-4}$	3.8778
(QWQ)	128	$3.1055 \cdot 10^{-5}$	4.0880	$3.8541 \cdot 10^{-5}$	3.9953
(QWQ)	256	$7.0448 \cdot 10^{-6}$	4.4082	$1.0091 \cdot 10^{-5}$	3.8193
(WQW)	8	$7.7713 \cdot 10^{-3}$	–	$8.9851 \cdot 10^{-3}$	–
(WQW)	16	$2.1537 \cdot 10^{-3}$	3.6084	$2.4826 \cdot 10^{-3}$	3.6193
(WQW)	32	$5.6685 \cdot 10^{-4}$	3.7994	$6.6928 \cdot 10^{-4}$	3.7093
(WQW)	64	$1.4460 \cdot 10^{-4}$	3.9200	$1.7291 \cdot 10^{-4}$	3.8706
(WQW)	128	$3.5811 \cdot 10^{-5}$	4.0380	$4.3413 \cdot 10^{-5}$	3.9830
(WQW)	256	$8.2621 \cdot 10^{-6}$	4.3343	$1.1261 \cdot 10^{-5}$	3.8550

Table 7.3: L^2-error data for ρ and q for the linear velocity setting in dependence of the number of time steps N for different splitting methods

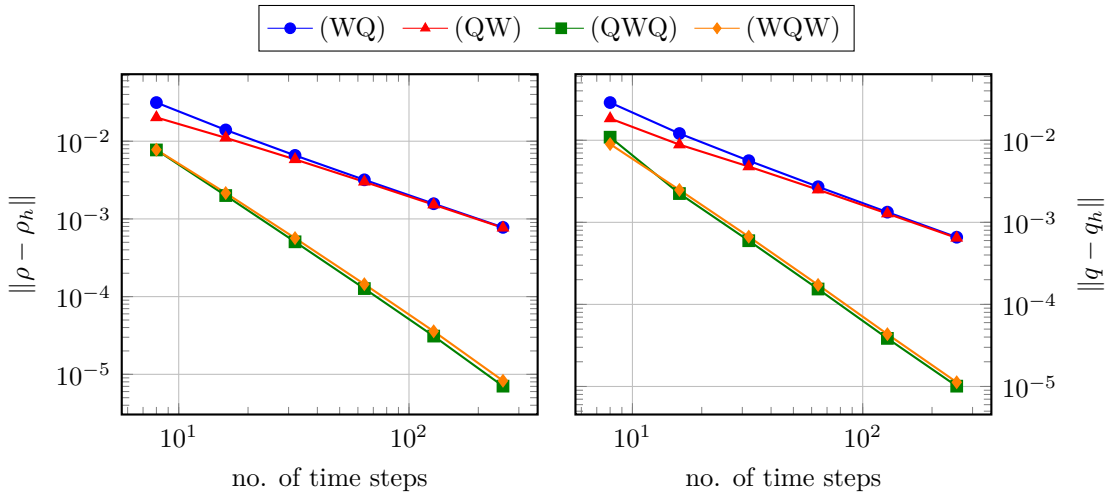

Figure 7.5: L^2-error plot for ρ and q for the linear velocity setting in dependence of the number of time steps for different splitting methods

Figure 7.6. Here, the L^2-error in ρ and q is depicted in dependence of the number of the degrees of freedom in x_1-direction. The corresponding data is specified in Table 7.4.

As for the numerical test with constant velocity, the observed convergence behavior is very similar for both ρ and q. The polynomial degrees $p > 0$ again yield much better results than the finite volume method with $p = 0$. It is conspicuous that the degree $p = 1$ has a remarkably good convergence behavior in comparison to $p = 2$. As expected, the absolute L^2-error, however, is smaller for $p = 2$.

7.2 Dislocation eigenstresses

Dislocation interactions are induced by the local stress fields of dislocations. Thus, a precise evaluation of the dislocation eigenstresses is indispensable for a reliable approximation of the fully-coupled system. For straight discrete dislocation lines with pure edge or screw character in an isotrope, infinitely large body, the analytical eigenstresses are known, cf. Section 3.7. They are used in the following to validate the computation of the stress field caused by a single dislocation line. This is a common test setting for the numerical approximation of the macroscopic problem in dislocation based plasticity (e.g. Sandfeld, 2010, Appendix B).

Since the focus lies on the dislocation eigenstresses, a macroscopic configuration without any outer forces is considered, i.e. $\mathbf{t}_{\mathrm{N}} \equiv \mathbf{0}$ and $\mathbf{b}_{\mathcal{B}} \equiv \mathbf{0}$. Then the macroscopic problem (6.1) together with Hooke's law allows to evaluate the eigenstresses numerically. We examine the stress fields of both screw and edge dislocations to validate the macroscopic solution method presented in Section 6.1.

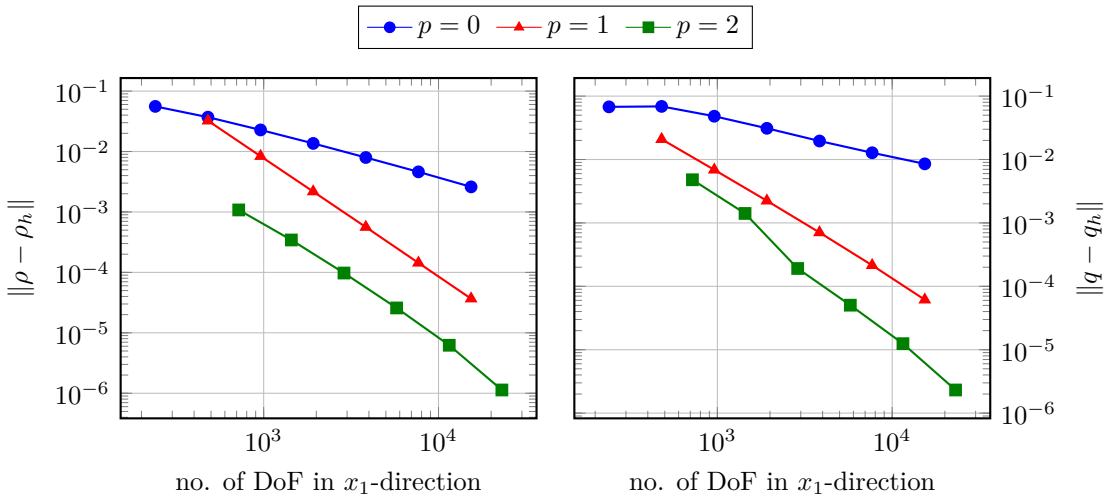

Figure 7.6: L^2-error plot for ρ and q for the linear velocity setting in dependence of the number of degrees of freedom for different polynomial degrees p

p	n	$\|\rho - \rho_h\|$	rate	$\|q - q_h\|$	rate
0	3	$5.5813 \cdot 10^{-2}$	–	$6.7652 \cdot 10^{-2}$	–
0	4	$3.7030 \cdot 10^{-2}$	1.5072	$6.8805 \cdot 10^{-2}$	0.9832
0	5	$2.2759 \cdot 10^{-2}$	1.6270	$4.8154 \cdot 10^{-2}$	1.4288
0	6	$1.3627 \cdot 10^{-2}$	1.6702	$3.1068 \cdot 10^{-2}$	1.5499
0	7	$7.9648 \cdot 10^{-3}$	1.7109	$1.9581 \cdot 10^{-2}$	1.5867
0	8	$4.6091 \cdot 10^{-3}$	1.7281	$1.2775 \cdot 10^{-2}$	1.5327
0	9	$2.6007 \cdot 10^{-3}$	1.7723	$8.5396 \cdot 10^{-3}$	1.4960
1	3	$3.2351 \cdot 10^{-2}$	–	$2.0871 \cdot 10^{-2}$	–
1	4	$8.3683 \cdot 10^{-3}$	3.8659	$6.8787 \cdot 10^{-3}$	3.0341
1	5	$2.1738 \cdot 10^{-3}$	3.8496	$2.2350 \cdot 10^{-3}$	3.0778
1	6	$5.6145 \cdot 10^{-4}$	3.8718	$7.0576 \cdot 10^{-4}$	3.1667
1	7	$1.4373 \cdot 10^{-4}$	3.9063	$2.1460 \cdot 10^{-4}$	3.2888
1	8	$3.6742 \cdot 10^{-5}$	3.9118	$6.1400 \cdot 10^{-5}$	3.4950
2	3	$1.0800 \cdot 10^{-3}$	–	$4.7941 \cdot 10^{-3}$	–
2	4	$3.4384 \cdot 10^{-4}$	3.1411	$1.4100 \cdot 10^{-3}$	3.4000
2	5	$9.7575 \cdot 10^{-5}$	3.5238	$1.9109 \cdot 10^{-4}$	7.3787
2	6	$2.5796 \cdot 10^{-5}$	3.7825	$5.0396 \cdot 10^{-5}$	3.7918
2	7	$6.2277 \cdot 10^{-6}$	4.1422	$1.2460 \cdot 10^{-5}$	4.0448
2	8	$1.1323 \cdot 10^{-6}$	5.5003	$2.3163 \cdot 10^{-6}$	5.3790

Table 7.4: L^2-error data for ρ and q for the linear velocity setting in dependence of the number of degrees of freedom for different polynomial degrees p with mesh width $h = 2^{-n}$ µm

7.2.1 Edge dislocation

For the numerical computation of the stress field of a single line defect, we need to transfer the discrete setting to the continuum framework. A discrete edge dislocation line gliding with constant velocity v_0 on a slip plane $\Gamma = \operatorname{span}\{\mathbf{d}, \mathbf{l}\}$ can be modeled in the context of the CDD theory by a normally distributed dislocation density distribution with vanishing curvature density of the form

$$\begin{aligned}
\rho(t, \mathbf{x}) &= \frac{1}{2\pi\tilde{s}^2} \exp\Big(-\frac{1}{2\tilde{s}^2}\Big(\big((\mathbf{x} - \mathbf{x}_0(t)) \cdot \mathbf{d}\big)^2 + \big((\mathbf{x} - \mathbf{x}_0(t)) \cdot \mathbf{m}\big)^2\Big)\Big) \\
\boldsymbol{\kappa}(t, \mathbf{x}) &= \rho(\mathbf{x}, 0)\mathbf{l} \\
q(t, \mathbf{x}) &= 0
\end{aligned}$$

with $\mathbf{x}_0(t) = \mathbf{x}_0(0) + v_0 t\,\mathbf{d}$ denoting the current position of the dislocation line and $\tilde{s}$ being the standard deviation. This is a traveling wave solution of the CDD system (4.8) with initial values $\rho(0, \cdot\,)$, $\boldsymbol{\kappa}(0, \cdot\,)$ and $q(0, \cdot\,)$.

Via Orowan's equation (4.7), the corresponding plastic slip γ representing the previous motion of the dislocation line in an infinitely large geometry arises as

$$\begin{aligned}
\gamma(t, \mathbf{x}) &= \int_{-\infty}^{t} \rho(\hat{t}, \mathbf{x}) b v_0 \,\mathrm{d}\hat{t} \\
&= \frac{b v_0}{2\pi\tilde{s}^2} \int_{-\infty}^{t} \exp\Big(-\frac{1}{2\tilde{s}^2}\Big(\big((\mathbf{x} - \mathbf{x}_0(\hat{t})) \cdot \mathbf{d}\big)^2 + \big((\mathbf{x} - \mathbf{x}_0(\hat{t})) \cdot \mathbf{m}\big)^2\Big)\Big)\mathrm{d}\hat{t} \\
&= \frac{b v_0}{2\pi\tilde{s}^2} \int_{-\infty}^{t} \exp\Big(-\frac{1}{2\tilde{s}^2}\big((\mathbf{x} - \mathbf{x}_0(\hat{t})) \cdot \mathbf{d}\big)^2\Big)\,\mathrm{d}\hat{t}\ \exp\Big(-\frac{1}{2\tilde{s}^2}\big((\mathbf{x} - \mathbf{x}_0(0)) \cdot \mathbf{m}\big)^2\Big) \\
&= \frac{b}{2}\left(1 - \operatorname{erf}\Big(\frac{1}{\sqrt{2}\tilde{s}}\big((\mathbf{x} - \mathbf{x}_0(t)) \cdot \mathbf{d}\big)\Big)\right) \frac{1}{\sqrt{2\pi}\tilde{s}} \exp\Big(-\frac{1}{2\tilde{s}^2}\big((\mathbf{x} - \mathbf{x}_0(0)) \cdot \mathbf{m}\big)^2\Big).
\end{aligned}$$

By choosing γ in this way and omitting any external forces, we can numerically compute the eigenstress field of an edge dislocation.

For the numerical tests, we use the slip system with coordinate basis $\mathbf{d} = \mathbf{e}_1$, $\mathbf{l} = \mathbf{e}_2$, $\mathbf{m} = \mathbf{e}_3$ and Burgers size $b = 0.256\,\mathrm{nm}$ as well as the Lamé constants $\lambda = 54.721\,\mathrm{GPa}$, $\mu = 24.1277\,\mathrm{GPa}$. The dislocation line is supposed to lie in the center of a cube

$$\mathcal{B} = [-2.5\,\mu\mathrm{m}, 2.5\,\mu\mathrm{m}]^3,$$

i.e. $\mathbf{x}(t) = \mathbf{0}$.

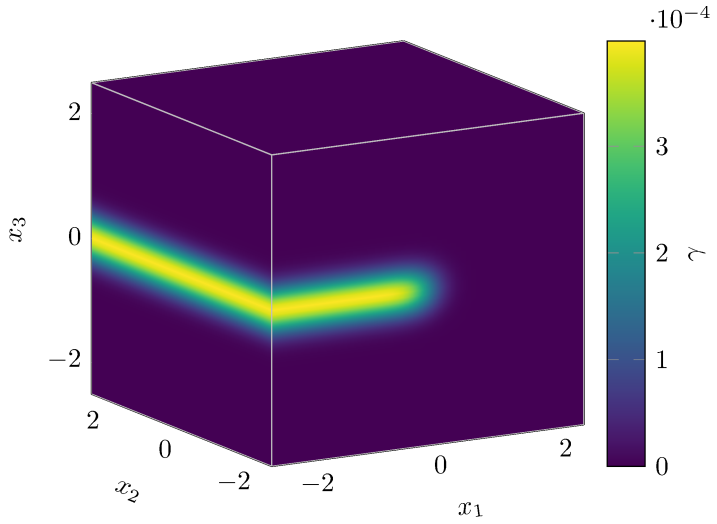

Figure 7.7: Plastic slip reflecting the motion history of a single edge dislocation line lying in the center of a cube

The resulting plastic slip for the standard deviation $\tilde{s} = 0.25\,\mu\text{m}$ is shown in Figure 7.7. The geometry is discretized into hexahedral cells with mesh width $h = 5 \cdot 2^{-6}\,\mu\text{m}$. We use the solution scheme for the macroscopic problem presented in Section 6.1 with trilinear ansatz functions and perform a single time step. The corresponding non-vanishing components of the Cauchy stress tensor in a cross-section perpendicular to the line direction are illustrated in Figure 7.8.

In order to compare the numerically computed stresses and the analytical stresses, the discrete stresses are transferred to the continuum context. Based on the discrete stresses σ^{ana}, we derive reference stresses σ^{ref} for the continuous formulation by convolution with the dislocation density

$$\sigma^{\text{ref}}(\mathbf{x}) = (\rho * \sigma^{\text{ana}})(\mathbf{x}) = \int_{\mathbb{R}^2} \rho(\hat{\mathbf{x}}) \sigma^{\text{ana}}(\mathbf{x} - \hat{\mathbf{x}})\, \mathrm{d}(\hat{x}_1, \hat{x}_3)$$

(e.g. Groma et al., 2003).

The comparison is given for different standard deviations $\tilde{s}$ in Figure 7.9 together with the discrete stresses. Close to the dislocation location, we observe a satisfactory agreement between all numerical stresses and the corresponding reference stresses. Though near the boundary of the geometry, there is a discrepancy observable. However, since the numerical test is limited to a bounded geometry, whereas the reference stresses are based on the analytical dislocation eigenstresses in an unbounded body, a better accordance is not expectable.

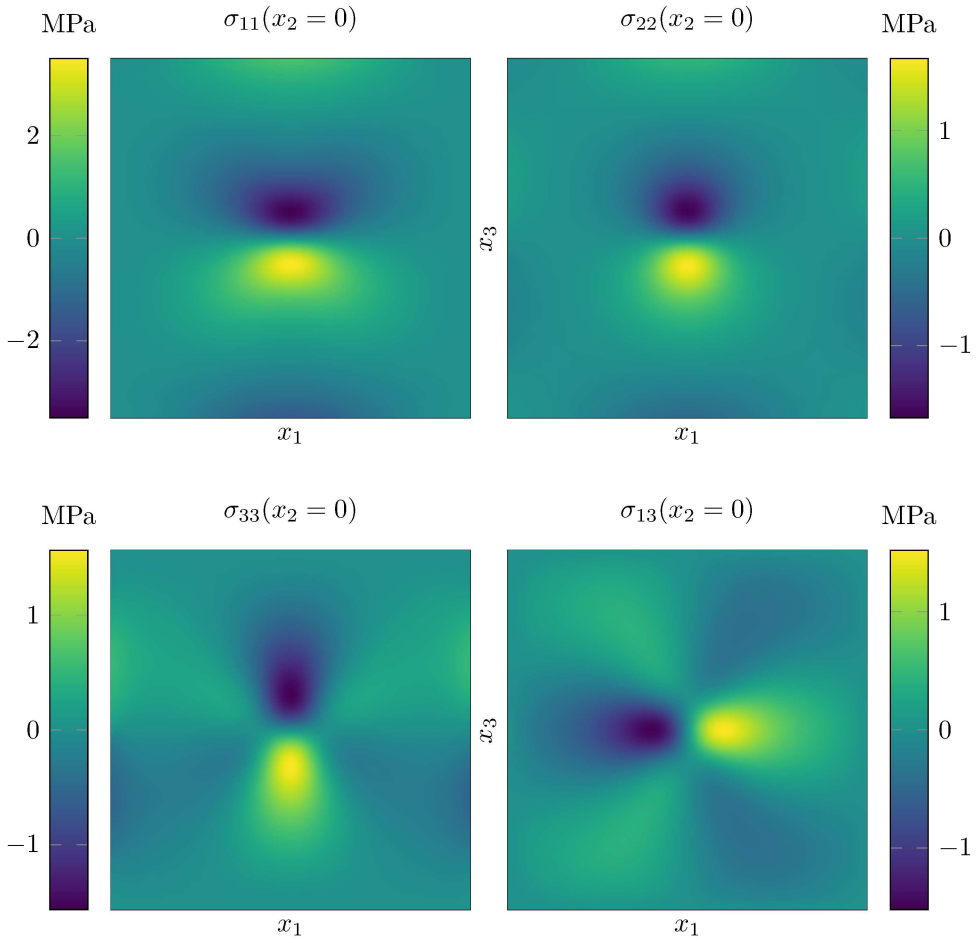

Figure 7.8: Non-zero stress components of an edge dislocation with standard deviation $\tilde{s} = 0.25\,\mu\text{m}$ and Burgers size $b = 0.256\,\text{nm}$ in a cross-section perpendicular to the dislocation line

Furthermore, the dependence on the standard deviation $\tilde{s}$ is displayed. For a good representation of the singularity in the stress field of a discrete dislocation line, a small blurring width $\tilde{s}$ is necessary.

7.2.2 Screw dislocation

By analogy, we can approximate the stress field of screw dislocations by considering a dislocation density distribution of the form

$$\begin{aligned}\rho(t,\mathbf{x}) &= \frac{1}{2\pi\tilde{s}^2}\exp\Big(-\frac{1}{2\tilde{s}^2}\left((\mathbf{x}-\mathbf{x}_0(t))\cdot\mathbf{l}\right)^2-\frac{1}{2\tilde{s}^2}\left((\mathbf{x}-\mathbf{x}_0(t))\cdot\mathbf{m}\right)^2\Big)\\ \boldsymbol{\kappa}(t,\mathbf{x}) &= \rho(0,\mathbf{x})\mathbf{d}\\ q(t,\mathbf{x}) &= 0\end{aligned}$$

with standard deviation $\tilde{s}$ and $\mathbf{x}_0(t)=\mathbf{x}_0(0)-v_0t\mathbf{l}$. The corresponding plastic shear strain γ is given by

$$\begin{aligned}\gamma(t,\mathbf{x}) &= \int_{-\infty}^{t}\rho(\hat{t},\mathbf{x})bv_0\,\mathrm{d}\hat{t}\\ &= \frac{bv_0}{2\pi\tilde{s}^2}\int_{-\infty}^{t}\exp\Big(-\frac{1}{2\tilde{s}^2}\Big((\mathbf{x}-\mathbf{x}_0(\hat{t}))\cdot\mathbf{l}\Big)^2-\frac{1}{2\tilde{s}^2}\Big((\mathbf{x}-\mathbf{x}_0(\hat{t}))\cdot\mathbf{m}\Big)^2\Big)\,\mathrm{d}\hat{t}\\ &= \frac{bv_0}{2\pi\tilde{s}^2}\int_{-\infty}^{t}\exp\Big(-\frac{1}{2\tilde{s}^2}\Big((\mathbf{x}-\mathbf{x}_0(\hat{t}))\cdot\mathbf{l}\Big)^2\Big)\,\mathrm{d}\hat{t}\,\exp\Big(-\frac{1}{2\tilde{s}^2}\left((\mathbf{x}-\mathbf{x}_0(0))\cdot\mathbf{m}\right)^2\Big)\\ &= \frac{b}{2}\Big(1-\operatorname{erf}\Big(\frac{1}{\sqrt{2}\tilde{s}}\left(-(\mathbf{x}-\mathbf{x}_0(t))\cdot\mathbf{l}\right)\Big)\Big)\frac{1}{\sqrt{2\pi}\tilde{s}}\exp\Big(-\frac{1}{2\tilde{s}^2}\left((\mathbf{x}-\mathbf{x}_0(0))\cdot\mathbf{m}\right)^2\Big).\end{aligned}$$

Again the slip system $\mathbf{d}=\mathbf{e}_1$, $\mathbf{l}=\mathbf{e}_2$, $\mathbf{m}=\mathbf{e}_3$ with Burgers size $b=0.256\,\mathrm{nm}$ together with Lamé parameters $\lambda=54.721\,\mathrm{GPa}$, $\mu=24.1277\,\mathrm{GPa}$ is chosen for the numerical tests. We consider the same geometry, mesh and discretization as previously for the edge dislocation. The numerical approximations of the non-vanishing stress components of a screw dislocation line with $\tilde{s}=0.25\,\mu\mathrm{m}$ lying in $\mathbf{x}(t)=\mathbf{0}$ are displayed in Figure 7.10.

The comparison of the numerical stress components with reference stresses

$$\sigma^{\mathrm{ref}}(\mathbf{x}) = (\rho * \sigma^{\mathrm{ana}})(\mathbf{x}) = \int_{\mathbb{R}^2}\rho(\hat{\mathbf{x}})\sigma^{\mathrm{ana}}(\mathbf{x}-\hat{\mathbf{x}})\,\mathrm{d}(\hat{x}_2,\hat{x}_3).$$

is shown in Figure 7.11.

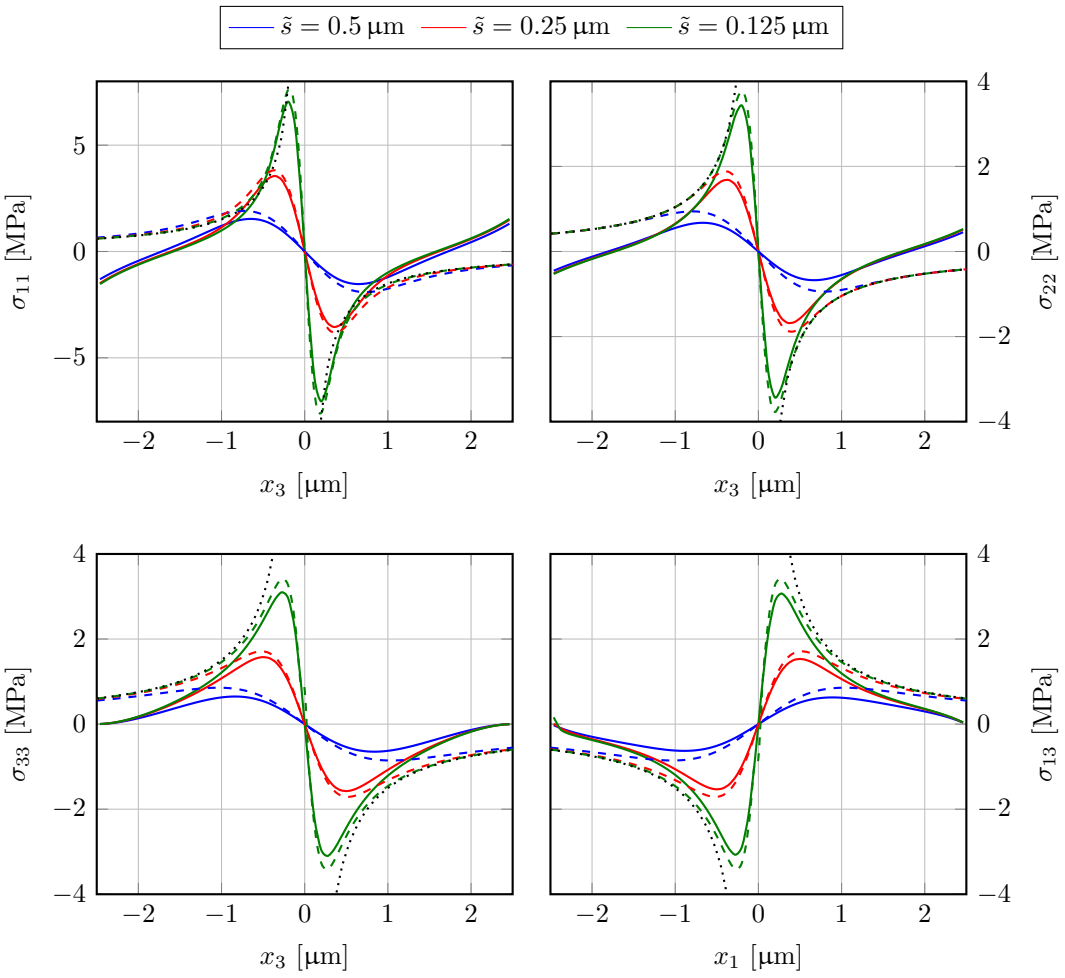

Figure 7.9: Non-zero stress components of an edge dislocation with varying standard deviation $\tilde{s}$ and Burgers size $b = 0.256\,\text{nm}$ along one axis perpendicular to the dislocation line (solid) in comparison with the reference (dashed) and analytical stresses (dotted)

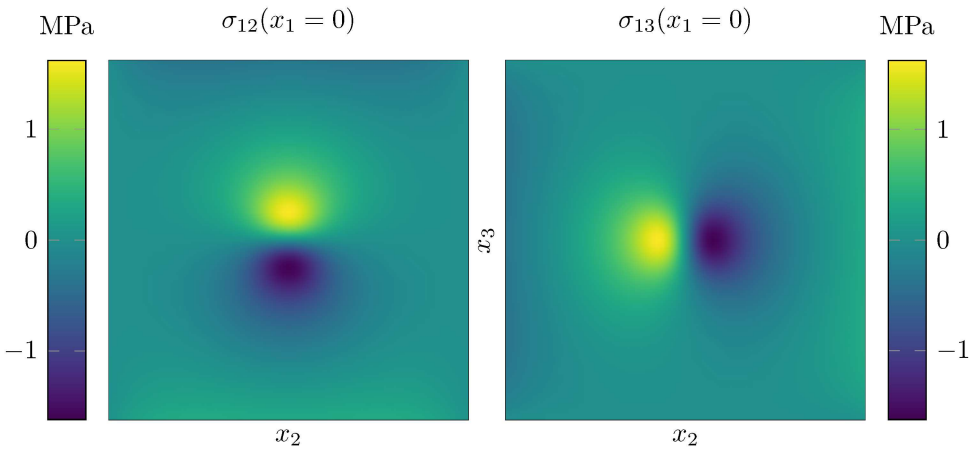

Figure 7.10: Non-zero stress components of a screw dislocation with standard deviation $\tilde{s} = 0.25\,\mu\text{m}$ and Burgers size $b = 0.256\,\text{nm}$ in a cross-section perpendicular to the dislocation line

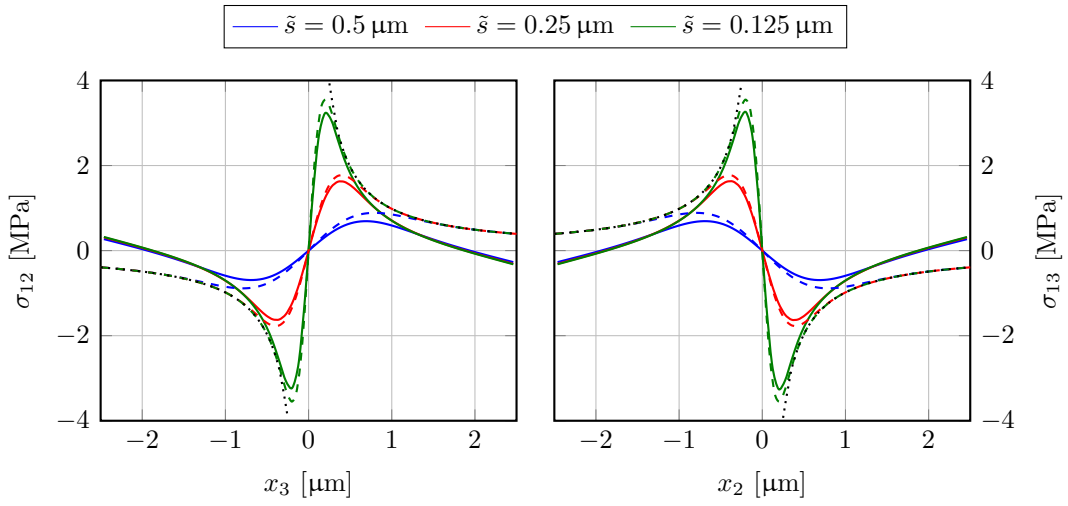

Figure 7.11: Non-zero stress components of a screw dislocation with varying standard deviation $\tilde{s}$ and Burgers size $b = 0.256\,\text{nm}$ along one axis perpendicular to the dislocation line (solid) in comparison with the reference (dashed) and analytical stresses (dotted)

The numerical results are very similar to those for the edge dislocation. We observe a very good accordance with the reference stresses. Overall the eigenstresses for both edge and screw dislocations are reproduced satisfactorily. This is fundamental for the representation of dislocation interaction in a continuum framework. Together with the validation of the numerical solution scheme for the CDD system in Section 7.1, it is now possible to examine the fully-coupled model.

CHAPTER 8
A tricrystal under tensile loading

In Chapter 5 and 6, a numerical approximation scheme for the fully-coupled elastoplasticity model presented in Chapter 4 has been derived. The numerical solution of the CDD system and of the macroscopic problem have been validated in various benchmark tests in Chapter 7. In this chapter, we investigate the approximation scheme for the fully-coupled model. We start by examining a simplified setting with one single slip system in a bicrystalline geometry. This allows to analyze dislocation interactions induced by the eigenstresses across the grain boundary. After ensuring that these physical effects are represented correctly, we are ready to tackle a configuration incorporating a full fcc crystal structure. We consider a tensile test of a geometry consisting of three cubic fcc grains arranged in a row. The numerical results are compared to DDD data from the literature. We conclude this chapter with a discussion of the results for the tricrystal.

The results presented in this chapter have been published in Schulz et al. (2019).

8.1 A single slip bicrystal

Before considering a full fcc system, we commence with a simplified single slip configuration. The goal is to demonstrate the dislocation interaction across a grain boundary caused by the eigenstress fields of the dislocations in the adjacent grains.

Dislocations moving towards an impenetrable boundary, as e.g. a grain boundary, are supposed to build a pile-up due to their interfering stress fields. If dislocations in two neighboring grains move towards the common grain boundary, the pile-up behavior inside one grain is influenced by the dislocations in the facing grain. The stress fields invoked by the dislocation motion in both neighboring grains are superposed. Thereby, according to the velocity law, dislocations have an impact on the dislocation motion in a neighboring grain. The concrete interaction effects depend significantly on the relative orientation of

the interacting slip systems. This dependency has been investigated in DDD simulations (Kapoor and Verdhan, 2017).

We analyze the dislocation interactions by considering a bicrystal and varying the orientation of the adjacent grains.

8.1.1 System setup

We regard a bicrystalline ($G = 2$) geometry

$$\overline{\mathcal{B}} = [0, l]^2 \times [0, w]$$

with length and height $l = 1.5\,\mu\text{m}$ and width $w = 1.11\,\mu\text{m}$. It consists of two grains

$$\mathcal{B}_1 = (0, \tfrac{l}{2}) \times (0, l) \times (0, w) \qquad \text{and} \qquad \mathcal{B}_2 = (\tfrac{l}{2}, l) \times (0, l) \times (0, w)$$

separated by an impenetrable grain boundary at $x_1 = \frac{l}{2}$. The boundary $\partial\mathcal{B}$ is chosen to be a free outflow boundary. Notably, the boundaries on the outer left ($x_1 = 0$) and outer right ($x_1 = l$) surface are free. Hence the dislocation density can move out of the system there.

In each grain a reduced crystal structure consisting of a single slip system ($S = 1$) is considered. The slip systems in both grains are tilted by an angle α around the x_3-axis. They are given by

$$\mathbf{d}_1 = \begin{pmatrix} \cos\alpha \\ -\sin\alpha \\ 0 \end{pmatrix}, \quad \mathbf{l}_1 = \begin{pmatrix} 0 \\ 0 \\ -1 \end{pmatrix}, \quad \mathbf{m}_1 = \begin{pmatrix} \sin\alpha \\ \cos\alpha \\ 0 \end{pmatrix} \qquad \text{in } \mathcal{B}_1$$

and

$$\mathbf{d}_2 = \begin{pmatrix} \cos\alpha \\ \sin\alpha \\ 0 \end{pmatrix}, \quad \mathbf{l}_2 = \begin{pmatrix} 0 \\ 0 \\ -1 \end{pmatrix}, \quad \mathbf{m}_2 = \begin{pmatrix} -\sin\alpha \\ \cos\alpha \\ 0 \end{pmatrix} \qquad \text{in } \mathcal{B}_2,$$

respectively. The geometry of the bicrystal including the slip systems is depicted in Figure 8.1a.

We prescribe an initial distribution of dislocation density which is normally distributed in Burgers direction $\mathbf{d}_g$ by

$$\rho_g(0, \mathbf{x}) = \frac{\tilde{\rho}}{\sqrt{2\pi}\tilde{s}} \exp\!\left(-\frac{1}{2\tilde{s}^2}\left((\mathbf{x} - \mathbf{x}_g) \cdot \mathbf{d}_g\right)^2\right)$$

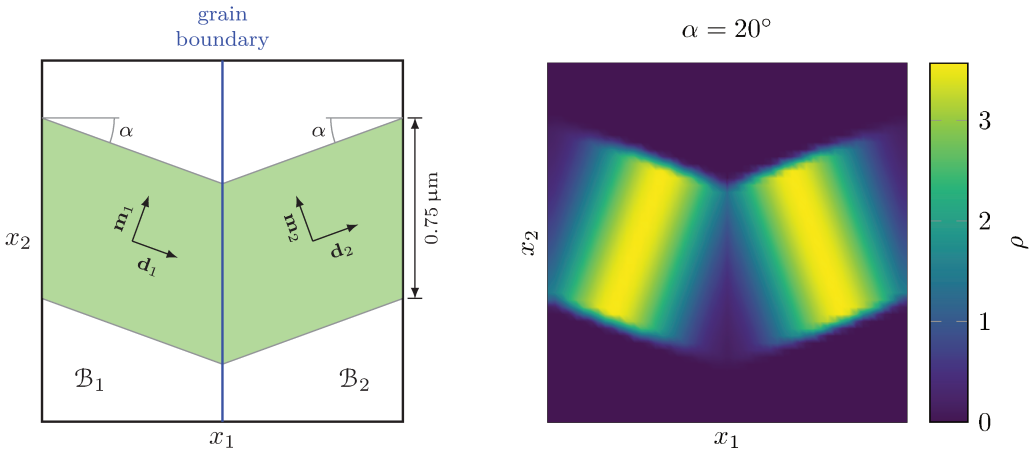

(a) Geometry (b) Initial dislocation density for $\alpha = 20°$

Figure 8.1: Geometry and initial data for the single slip bicrystal setting

for each grain $g = 1, 2$ with

$$\mathbf{x}_1 = \frac{l}{4}\begin{pmatrix}1\\1\\0\end{pmatrix} \qquad \text{and} \qquad \mathbf{x}_2 = \frac{l}{4}\begin{pmatrix}3\\1\\0\end{pmatrix}$$

as well as $\tilde{\rho} = \frac{4.5}{\sqrt{2\pi}}\,\mu\text{m}^{-1}$ and $\tilde{s} = 0.2\,\mu\text{m}$. The dislocation density is assumed to be pure SSD density, i.e. $\boldsymbol{\kappa}_g(0,\cdot) \equiv \mathbf{0}$ for $g = 1, 2$.

In order to avoid an inflow or outflow at the top and bottom of the geometry, the dislocation density is restricted to a channel of $0.75\,\mu\text{m}$ height. See Figure 8.1b for an illustration of the initial density distribution. The curvature density is assumed to vanish, i.e. $q_g \equiv 0$ for $g = 1, 2$. Moreover, we assume that initially no plastic slip is present in the bicrystal, thus $\gamma_g(0,\cdot) \equiv 0$ for $g = 1, 2$.

In this simplified setting, the focus is on the dislocation interactions induced by the dislocation eigenstresses. For this reason, no external load is applied. As a consequence, the macroscopic equilibrium reflects the eigenstress state, cf. Section 7.2. To activate dislocation motion, a constant external stress $\tau^{\text{ext}} = 0.5\,\text{MPa}$ on the slip system of each grain is prescribed. A reduced dislocation velocity law is used neglecting the yield stress as well as the back stress, i.e., $\tau_g^{\text{y}} \equiv 0$ and $\tau_g^{\text{b}} \equiv 0$. Thus the overall velocity law reads

$$v_g = \frac{b}{B}(\tau_g^{\text{res}} + \tau^{\text{ext}})$$

with Burgers size $b = 2.56 \cdot 10^{-4}\,\mu\text{m}$, drag coefficient $B = 2 \cdot 10^{-4}\,\text{GPa}\cdot\text{ns}$, resolved shear stress $\tau_g^{\text{res}} = \mathbb{C}[\boldsymbol{\varepsilon} - \boldsymbol{\varepsilon}^{\text{pl}}(\gamma_g)] : (\mathbf{m}_g \otimes \mathbf{d}_g)$ and Lamé parameters $\mu = 24.1277\,\text{GPa}$ and $\lambda = 54.721\,\text{GPa}$.

For the time discretization the Strang splitting (QWQ) introduced in Section 5.1 is used. The time step size is chosen to be $\triangle t = 4\,\text{ns}$.

For the space discretization the geometry is decomposed into hexahedral cells. We use an equidistant mesh which is modified by a refinement of the cells located directly at the grain boundary. The refinement is equivalent to the one we later choose for the tricrystalline geometry in Section 8.2.3. For the approximation of the CDD system the discontinuous Galerkin ansatz spaces for polynomial degree $p = 2$ are used.

8.1.2 The purpose of this setting

Taking a closer look at the CDD system (4.8) makes it clear that in a system with pure SSD density, initially only the evolution equation for $\boldsymbol{\kappa}_g$ is of importance. It can be formulated in two scalar equations as

$$\begin{aligned}\partial_t \kappa_g^1 &= \nabla(v_g \rho_g) \cdot \mathbf{l}_g \\ \partial_t \kappa_g^2 &= -\nabla(v_g \rho_g) \cdot \mathbf{d}_g.\end{aligned}$$

In the case of in space constant dislocation velocity v_g this simplifies to

$$\begin{aligned}\partial_t \kappa_g^1 &= v_g \nabla \rho_g \cdot \mathbf{l}_g \\ \partial_t \kappa_g^2 &= -v_g \nabla \rho_g \cdot \mathbf{d}_g.\end{aligned}$$

In the bicrystal setting, the initial dislocation density varies in Burgers direction $\mathbf{d}_g$ and is constant in $\mathbf{l}_g$-direction. Thus $\nabla \rho_g \cdot \mathbf{l}_g$ vanishes. Hence, in both grains the SSD density is expected to split up into positive and negative edge dislocation density. The positive edge dislocation density moves in positive Burgers direction, the negative counterpart in opposite direction. Due to this relation, the dislocation density stays limited to the domain where initially SSD density has been set, cf. Figure 8.1.

By this mechanism, positive edge dislocation density in the left grain $\mathcal{B}_1$ moves towards the grain boundary and negative edge dislocation density leaves the volume on the left. Conversely, in the right grain $\mathcal{B}_2$ the positive GND density exits whereas the negative part is transported towards the grain boundary.

The dislocation density which does not leave the volume halts when it reaches the grain boundary or the dislocation velocity vanishes, i.e. the internal stresses and the prescribed

external stress are in balance. The numerical tests are performed until such a converged state is established.

If the grains are of the same orientation ($\alpha = 0°$), the positive edge dislocations coming from the left and the negative edge dislocations coming from the right have the same shear eigenstress in the slip plane with opposite sign, cf. $\sigma_{13}^{\mathrm{ana}}$ in Section 3.7. Hence, the stresses annihilate and the dislocations can move without hindrance towards the grain boundary. Otherwise a repellent behavior is expected provoking a pile-up of dislocation density at the interface.

8.1.3 Results

Subsequently, the situation outlined above is investigated for the tilt angles $\alpha = 0°, 10°, 20°$. We are particularly interested in the behavior close to the grain boundary. We note that the case $\alpha = 0°$ is artificial. Without any misorientation of the slip systems, the geometry is actually single-crystalline. Thus dislocations can move through the material without any restrictions. For this test setting, however, the flux over the interface $\partial\mathcal{B}_1 \cap \partial\mathcal{B}_2$ is suppressed using an impenetrable boundary condition. A similar situation without misorientation in a 2D setting has been investigated by Stricker et al. (2016).

In Figure 8.2, the resulting edge dislocation density κ_g^2 is depicted for the considered tilt angles. While for $\alpha = 0°$ the dislocations move until they reach the grain boundary, for $\alpha = 10°$ and $\alpha = 20°$ the motion stops before reaching it. We observe that the dislocation density arranges perpendicular to the Burgers direction $\mathbf{d}_g$. With increasing tilt angle, the dislocation pile-up is stronger.

This behavior reflects in the plastic slip γ_g. The plastic slip integrated over the height of the system

$$\gamma_g^{\mathrm{int}}(x_1) = \int_0^l \gamma_g(x_1, x_2, \tfrac{w}{2})\,\mathrm{d}x_2$$

for the considered tilt angles is shown in Figure 8.3. The dependence of the pile-up behavior on the misorientation angle is clearly visible. For vanishing misorientation ($\alpha = 0°$) the plastic slip builds a horizontal line indicating that the entire density has passed as if the boundary did not exist. Only directly at the interface a small oscillation is observable. For $\alpha = 10°$ and $\alpha = 20°$ the plastic slip descends smoothly towards the grain boundary indicating the pile-up.

The observations in the bicrystal test are in very good agreement with the physically expected behavior. The pile-up behavior at the grain boundary is significantly affected by the relative orientation of the respective slip systems. In this numerical test, the grain

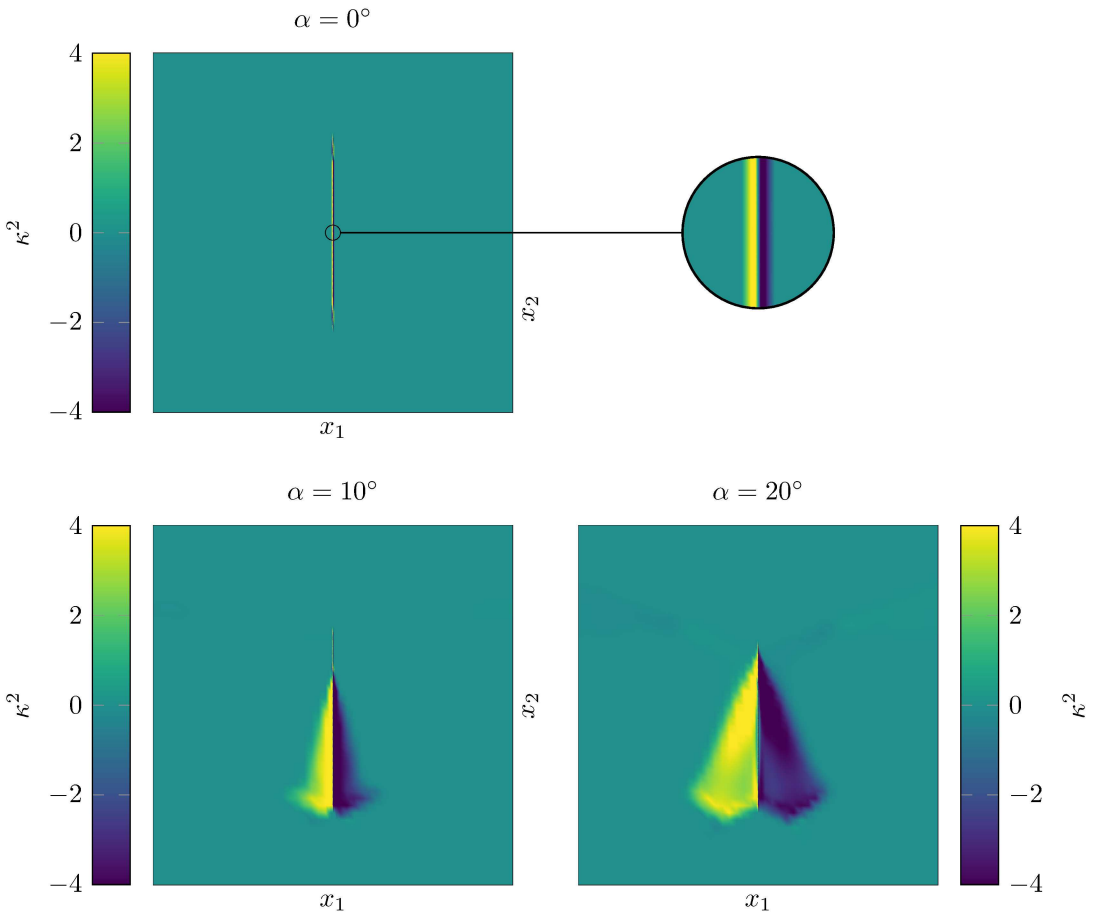

Figure 8.2: Edge dislocation density κ^2 for $x_3 = \frac{w}{2}$ in dependence of the tilt angle α

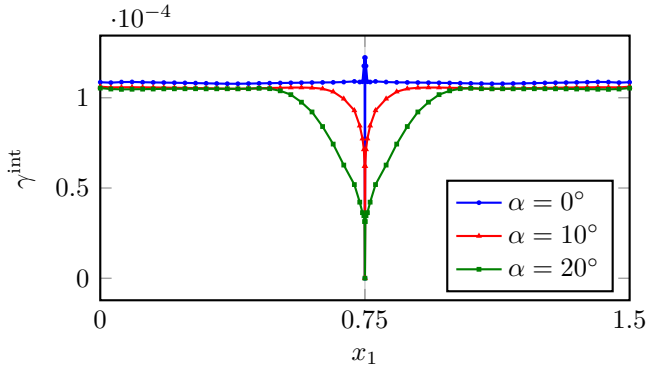

Figure 8.3: Plastic slip along the x_1-axis of the bicrystal for different tilt angles α

boundary has been realized by prescribing a vanishing numerical flux. We renounced to establish a smooth passage to zero of the velocity over several cells in order to avoid a distortion of the results. From this point of view, the oscillation in the plastic slip which we observed for $\alpha = 0°$ is tolerable. In the physically more relevant cases with higher tilt angles, the interfering stress fields naturally reduce the dislocation velocity and yield a smooth plastic slip.

8.2 System setup for the tricrystal

We are now ready to address a setting including a full face-centered cubic crystal structure. Again the focus lies on dislocation interaction across grain boundaries. Here, though, a tricrystalline rod under tensile load is considered. The configuration we give below is based on a numerical comparison between DDD and a gradient plasticity model by Bayerschen et al. (2015).

8.2.1 Geometry, initial values and material properties

We consider a tricrystalline ($G = 3$) geometry

$$\overline{\mathcal{B}} = [0\,\mu\text{m}, 2.25\,\mu\text{m}] \times [0\,\mu\text{m}, 0.75\,\mu\text{m}]^2$$

with three cubic single-crystalline grains

$$\begin{aligned}
\mathcal{B}_1 &= (0\,\mu\text{m}, 0.75\,\mu\text{m}) \times (0\,\mu\text{m}, 0.75\,\mu\text{m})^2 \\
\mathcal{B}_2 &= (0.75\,\mu\text{m}, 1.5\,\mu\text{m}) \times (0\,\mu\text{m}, 0.75\,\mu\text{m})^2 \\
\mathcal{B}_3 &= (1.5\,\mu\text{m}, 2.25\,\mu\text{m}) \times (0\,\mu\text{m}, 0.75\,\mu\text{m})^2,
\end{aligned}$$

see Figure 8.4.

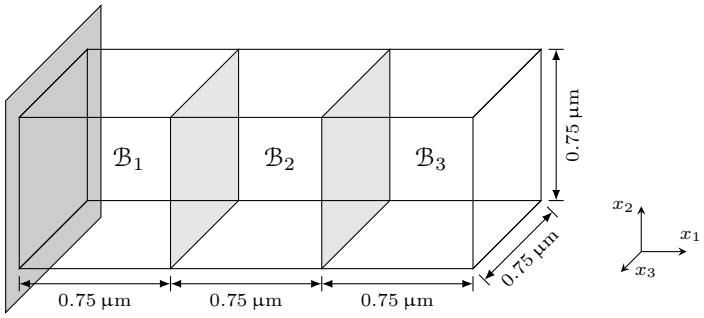

Figure 8.4: Geometry of the tricrystal configuration

Each grain is assumed to be fcc with $S = 12$ slip systems. The fcc slip systems of the left and right grain are oriented as summarized in Table 3.1. The central grain $\mathcal{B}_2$ is rotated by an angle α around the x_1-axis. The length of the Burgers vector is $b_{g,s} = 2.56 \cdot 10^{-4}$ µm for $s = 1, \dots, S$, $g = 1, 2, 3$.

In each slip system $s = 1, \dots, S$ and grain $g = 1, 2, 3$, an in space constant initial dislocation density $\rho^0 > 0$ is chosen, i.e.

$$\rho_{g,s}(0, \cdot) \equiv \rho^0,$$

and the averaged curvature of the dislocations is assumed to be constant such that the curvature density is given by

$$q_{g,s}(0, \cdot) \equiv \frac{\rho^0}{r_0}$$

with a constant dislocation radius $r_0 > 0$. We assume that there is no GND density in the beginning, i.e. $\boldsymbol{\kappa}_{g,s} \equiv \mathbf{0}$. This configuration corresponds to the presence of a homogeneous distribution of dislocation loops. Again the initial plastic slip is supposed to vanish, i.e. $\gamma_{g,s}(0, \cdot) \equiv 0$, $g = 1, 2, 3$.

The dislocation velocity is assumed to be given by the full velocity law (4.9) where the yield stress including the interaction matrix (4.11) is used. An impenetrable boundary condition without manipulating the velocity is selected on the grain boundaries and on the Dirichlet boundary (cf. Section 5.3.3 and 5.4.3).

The tricrystal $\mathcal{B}$ is subject to a tensile loading in x_1-direction which is realized by prescribing the displacement on the outer left and outer right surfaces of the geometry. Accordingly, the Dirichlet boundary reads

$$\partial_{\mathrm{D}}\mathcal{B} = \{\mathbf{x} = (x_1, x_2, x_3)^\top \in \partial\mathcal{B} \colon x_1 = 0\,\text{µm} \text{ or } x_1 = 2.25\,\text{µm}\}.$$

The load is applied with a constant strain rate $\dot{\varepsilon} = 5000\,\mathrm{s}^{-1}$, i.e. the Dirichlet values are given by

$$\mathbf{u}_{\mathrm{D}}(\mathbf{x}, t) = \begin{pmatrix} x_1 \dot{\varepsilon} t \\ 0 \\ 0 \end{pmatrix} \qquad \text{for } \mathbf{x} \in \partial_{\mathrm{D}}\mathcal{B}$$

where $t \in [0, T]$ with final time $T = 1000\,\mathrm{ns}$. On $\partial_{\mathrm{N}}\mathcal{B} = \partial\mathcal{B} \setminus \partial_{\mathrm{D}}\mathcal{B}$ homogeneous Neumann boundary conditions $\mathbf{t}_{\mathrm{N}} \equiv \mathbf{0}$ are chosen. No volume forces are considered, thus $\mathbf{b}_{\mathcal{B}} \equiv \mathbf{0}$. We note that the prescribed displacement on the Dirichlet boundary does not include transversal contraction. Therefore high stresses are expectable in the outer parts of the Dirichlet boundary.

The elastic material behavior is assumed to be linear, isotropic and homogeneous with Lamé parameters $\mu = 24.1277\,\mathrm{GPa}$ and $\lambda = 54.721\,\mathrm{GPa}$. Furthermore, we set the drag coefficient to $B = 2 \cdot 10^{-4}\,\mathrm{GPa \cdot ns}$. According to the considerations in Schmitt et al. (2015) we choose the backstress parameter $D = 0.255$.

Remark. The strain rate $\dot{\varepsilon}$ is chosen accordingly to the configuration in Bayerschen et al. (2015). It is rather large but still admissible for a problem which is assumed to be quasi-static (Senger et al., 2008). This is due to the computational limitations of the DDD method.

8.2.2 Time discretization

The time interval $[0, T]$ is discretized into 2000 time steps with step size $\triangle t = 0.5\,\mathrm{ns}$ for the macroscopic problem. In order to evaluate the CDD evolution equations, we perform in each time step of the macroscopic problem one time step for the CDD system using the Strang splitting (QWQ), cf. Section 5.1.

8.2.3 Space discretization

For the numerical tests, the system is discretized into hexahedral cells. The mesh is equidistant in x_2- and x_3-direction. We choose a non-equidistant discretization along the x_1-axis consisting of finer cells in the regions of the grain boundaries and the Dirichlet boundary. We use a smooth transition from wider to finer cells. This yields a better representation of the dislocation interactions across the grain boundaries and improves the pile-up behavior in general. With finer cells at the impenetrable boundaries, the stresses which are responsible for the pile-ups can be resolved more precisely. By this means, we obtain a stable numerical scheme without artificially reducing the dislocation velocity at impenetrable boundaries, cf. Section 5.3.3.

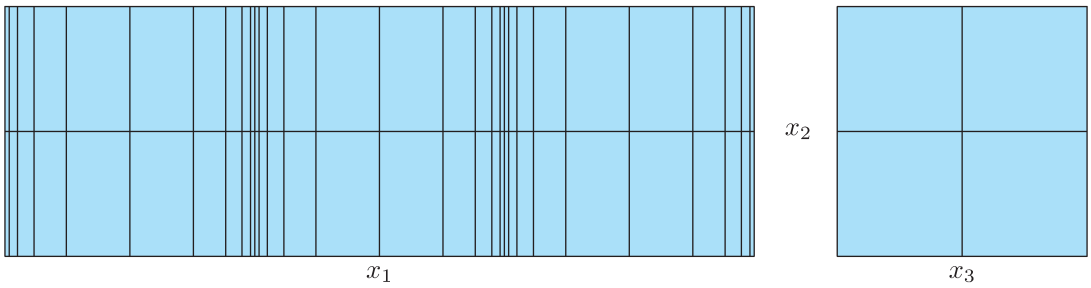

Figure 8.5: Graduated mesh for the tricrystal with $h_0 = 0.375\,\mu\text{m}$

The mesh is obtained as follows: First the geometry is discretized into congruent cubic cells with mesh width h_0 such that the grain boundaries consist of cell faces. Then each cell located at a grain boundary is refined in x_1-direction into five cells with mesh widths h_k, $k = 1, \dots, 5$. Here, a geometric refinement is used where

$$\frac{h_0}{h_1} = \frac{h_k}{h_{k+1}} \qquad \text{for } k = 1, 2, 3, 4.$$

The coarsest possible mesh of this type for $h_0 = 0.375\,\mu\text{m}$ is illustrated in Figure 8.5.

Remark. The choice of the mesh is a result of various numerical tests. It is a compromise between a high resolution of the dislocation pile-ups and reasonable numerical costs. Other choices are of course possible.

8.2.4 Concrete choice of the initial values

We aim to compare our numerical results with the DDD data given in Bayerschen et al. (2015). The different nature of CDD and DDD, however, has a direct impact on the scope of both models and makes comparisons between them challenging. The CDD model which we use does not incorporate source mechanisms that are essential in DDD. We therefore cannot directly transfer the initial data from DDD to CDD. For this reason, we use a simplified initial configuration with constant dislocation density and constant curvature density.

The choices of ρ^0 and r_0 influence the macroscopically observed material behavior. Varying ρ^0 allows to adjust the initial yield stress (4.10). Since the curvature density affects the dislocation density production via Equation (4.8a), the initial radius r_0 serves to control the amount of hardening.

We choose $\rho^0 = 11.5\,\mu\text{m}^{-2}$ and $r_0 = 0.075\,\mu\text{m}$ for both considered rotation angles $\alpha = 5°, 35°$. The resulting stress-strain curves are shown in Figure 8.6 where the normal stress and strain in x_1-direction are evaluated by averaging over the whole volume $\mathcal{B}$. The

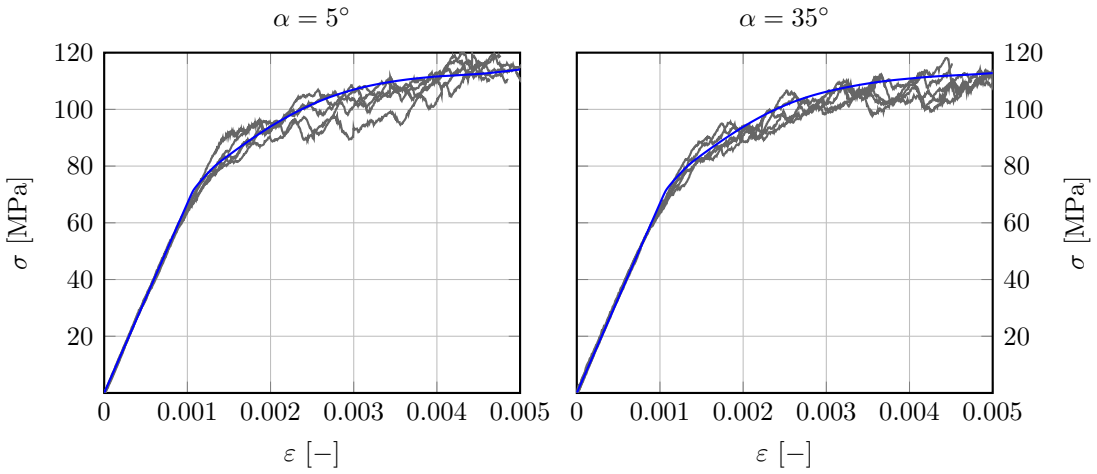

Figure 8.6: Stress-strain curve (blue) for $\alpha = 5°, 35°$ with mesh width $h_0 = 0.0625\,\mu\text{m}$, local degree $p = 2$ and $\triangle t = 0.5\,\text{ns}$ compared with DDD results (gray) from Bayerschen et al. (2015).

comparison of the CDD results with the DDD data given in Bayerschen et al. (2015) shows that the macroscopic stress-strain behavior fits well for both methods and the chosen initial values.

8.2.5 Comparison to the bicrystal

Besides the different geometry, the tricrystal setting differs from the bicrystal test in several points. While the bicrystal includes only one slip system per grain, we use a full fcc crystal structure here. Furthermore, the full velocity law (4.9) is applied for the tricrystal test. The initial values slightly differ since we start with curved dislocations. Concerning the macroscopic problem we prescribe a non-homogeneous displacement on the Dirichlet boundary.

When using the full velocity law in an fcc crystal structure, dislocation interaction is not only observable across the grain boundary. Via the interaction matrix (4.11) in the yield stress, also interaction between different glide systems is possible. Additionally, the back stress gives an interaction relation inside a glide plane.

For the bicrystal, a shear stress has been prescribed directly on the slip plane. For the tricrystal, the external stresses result from an applied external load. This implies that the resolved shear stress driving dislocation motion on a specific slip plane in general varies from slip system to slip system. Due to the yield stress it is probable that the different slip systems are activated – i.e. start dislocation motion – at different points in time.

8.2.6 Evaluation

In order to display the field quantities resulting from the numerical computations, a spatial averaging in cross-sections of the geometry in the x_2-x_3-plane is carried out. For this purpose, a physical quantity $Q\colon [0,T] \times \mathcal{B} \to \mathbb{R}$ is averaged in slices

$$\mathcal{S}(x) = \{\mathbf{x} = (x_1, x_2, x_3) \in \overline{\mathcal{B}}\colon x_1 = x\} \qquad \text{for } x \in [0\,\mu\text{m}, 2.25\,\mu\text{m}]$$

by

$$Q^{\text{avg}}\colon [0,T] \times [0\,\mu\text{m}, 2.25\,\mu\text{m}] \to \mathbb{R}, \quad (t, x_1) \mapsto \frac{1}{|\mathcal{S}(x_1)|} \int_{\mathcal{S}(x_1)} Q(t, \mathbf{x})\, \mathrm{d}(x_2, x_3).$$

For a reasonable comparison of different configurations, averaged quantities of this form are evaluated at specific instants of time which are determined by the total normal plastic strain in loading direction $\varepsilon_{11}^{\text{pl}}$. We consider the snapshots for

$$\varepsilon_{11}^{\text{pl}} \in \{0.001, 0.002, 0.003\}.$$

As a consequence of the uni-axial external load, dislocation motion on the different slip systems is supposed to start at different points in time depending on the orientation with respect to the loading direction. In each slip system s, dislocation motion is driven by the resolved shear stress $\tau_{g,s}^{\text{res}} = \boldsymbol{\sigma} : (\mathbf{m}_{g,s} \otimes \mathbf{d}_{g,s})$. This motivates a characterization of the slip systems by means of the x_1-components of the orthonormal basis vectors $\mathbf{d}_{g,s}$, $\mathbf{l}_{g,s}$ and $\mathbf{m}_{g,s}$. The x_1-component of the slip system vectors is by definition independent of the grain g. Therefore, we drop the index g in the subsequent classification of the slip systems.

Four slip systems have a vanishing x_1-component of the Burgers direction $\mathbf{d}_s$, cf. Table 3.1. Hence, hardly any dislocation motion is expected there for the considered tensile test. For this reason, the results for these systems are not investigated in more detail in the following.

For the remaining systems, the orientation of the Burgers direction $\mathbf{d}_s$ and the slip plane normal $\mathbf{m}_s$ are chosen such that the x_1-components are positive. This allows to group them depending on the sign of the x_1-component of $\mathbf{l}_s$. Both groups consist of four slip systems with similar behavior for the dislocation motion. Subsequently, the results of the numerical tests are depicted for one representative slip system of each group. According to the sign of the x_1-component of $\mathbf{l}_s$ all corresponding quantities are labeled with the index $+$ or $-$, respectively.

Remark. Although less dislocation motion occurs on the four not further investigated slip systems, they are considered in the numerical tests. They are activated later than the

other slip systems. However, also motionless dislocation density has an impact on the overall behavior via the yield stress.

8.3 Results for the tricrystal

We investigate the density distribution as well as the resulting plastic slip in the representative slip systems. In Figure 8.7, the averaged screw and edge part of the GND density along the x_1-axis are shown for the rotation angles $\alpha = 5°, 35°$ and the total plastic strain snapshots $\varepsilon_{11}^{\mathrm{pl}} = 0.001, 0.002, 0.003$. The corresponding plastic slip is depicted in Figure 8.8.

We observe that the GND density builds pile-ups on the grain boundaries as well as on the Dirichlet boundaries on the outer left and right. The width of the pile-ups increases with increasing total plastic strain. Comparing the two representative slip systems, only slight differences are visible. Moreover, we show the distribution of the screw dislocation density for both angles $\alpha = 5°, 35°$ in a longitudinal section examplarily for one representative slip system in Figure 8.9. This illustrates the distribution of the dislocation density inside the geometry. The pile-ups can clearly be identified here. Moreover, it is apparent that the SSD density is split up according to the orientation of the slip system into positive and negative GND density similar to the observations for the bicrystal.

The plastic slip smoothly decreases towards the impenetrable boundaries for all displayed configurations. It appears that the plastic slip evolution depends on the rotation angle α. While for $\alpha = 5°$ the plastic slip in the central grain is of similar magnitude as in the outer grains, for $\alpha = 35°$ the plastic slip distribution is much more pronounced in the central grain. As for the dislocation density distribution, there is no significant difference observable comparing the results of the representative slip systems.

We illustrate the norm of the plastic distortion tensor β^{pl} for $\alpha = 5°$ in a longitudinal clip for the total plastic strain snapshot $\varepsilon_{11}^{\mathrm{pl}} = 0.002$ in Figure 8.10. In the plastic distortion tensor the plastic slip distributions of all slip systems are superposed with regard to the slip system orientation, cf. Equation (3.2). Therefore, the plastic distortion tensor mainly varies in loading direction. The observations are consistent with those for the plastic slip in Figure 8.8. The pile-ups are clearly observable and the distribution in the outer grains is shifted towards the grain boundaries.

Figure 8.11 depicts the evolution of the total plastic strain in loading direction for the considered rotation angles. This data is used to validate the results by comparison with DDD data given by Bayerschen et al. (2015). We observe according to the plastic slip evolution that for $\alpha = 35°$ the plastic strain in the central grain is higher than in the

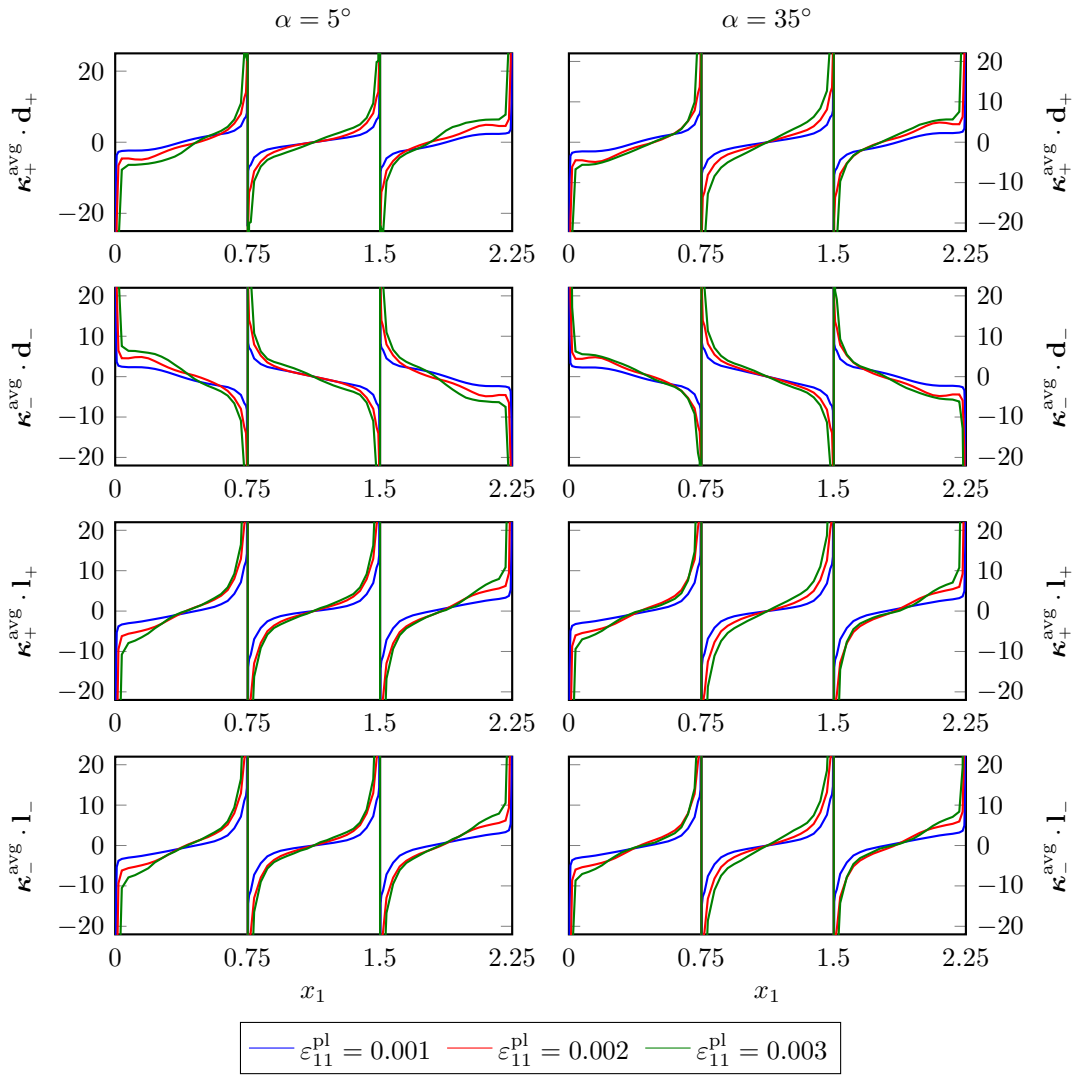

Figure 8.7: Evolution of the GND density for $\alpha = 5°, 35°$ with $h_0 = 0.0375\,\mu\text{m}$, local degree $p = 2$ and $\triangle t = 0.5\,\text{ns}$

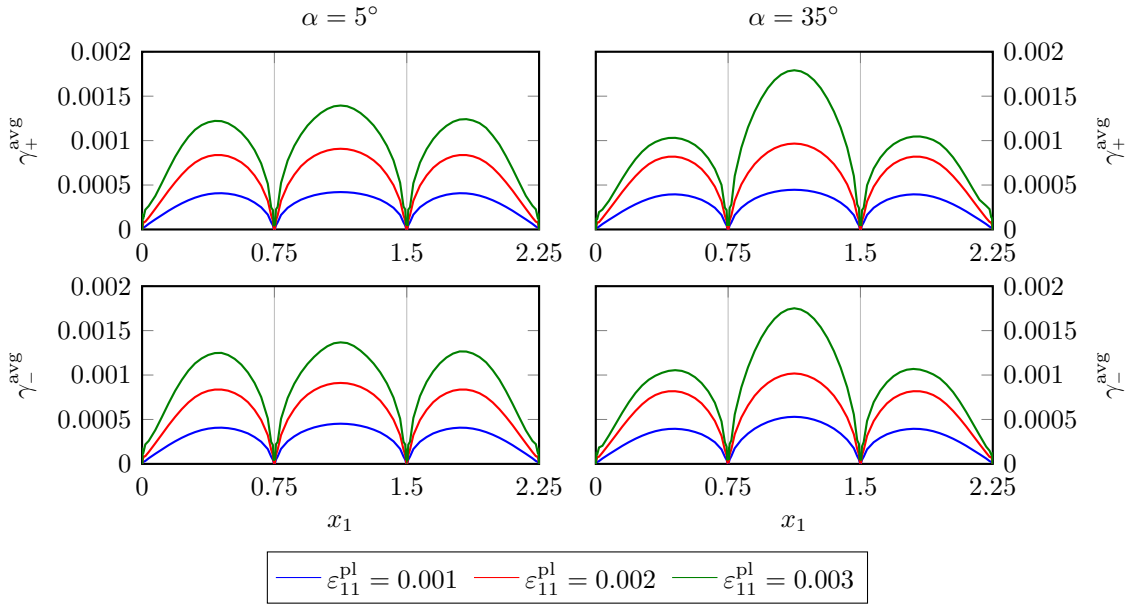

Figure 8.8: Evolution of the plastic slip for $\alpha = 5°, 35°$ with $h_0 = 0.0375\,\mu\text{m}$, local degree $p = 2$ and $\triangle t = 0.5\,\text{ns}$

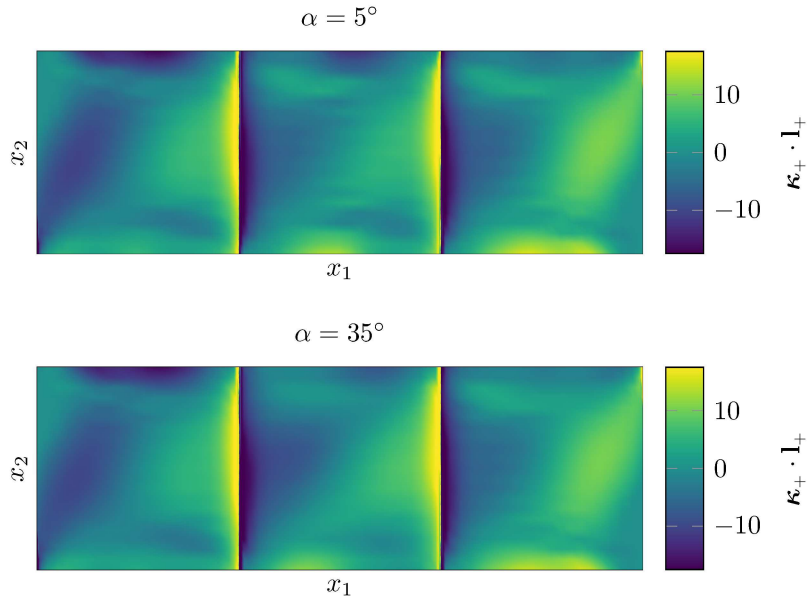

Figure 8.9: Screw dislocation density $\boldsymbol{\kappa}_+ \cdot \mathbf{l}_+$ for $x_3 = 0.375\,\mu\text{m}$ and $\varepsilon_{11}^{\text{pl}} = 0.002$ in dependence of the twist angle α

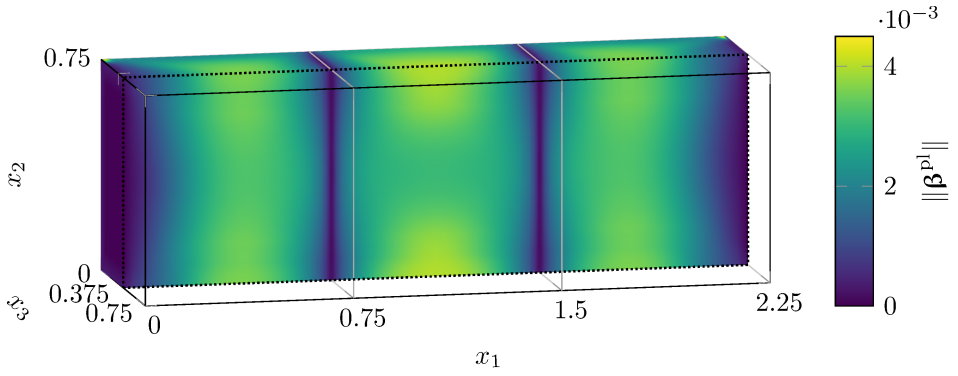

Figure 8.10: Plastic distortion for $\alpha = 5°$ and $\varepsilon_{11}^{\mathrm{pl}} = 0.002$ in a longitudinal clip for $x_3 \in [0, 0.375\,\mu\mathrm{m}]$ computed with $h_0 = 0.0375\,\mu\mathrm{m}$, local degree $p = 2$ and $\triangle t = 0.5\,\mathrm{ns}$

adjacent grains. Again a more balanced distribution can be observed for $\alpha = 5°$. These findings are in good accordance with the discrete reference results.

8.4 Discussion

We have already seen how the tilt angle in a simplified single slip bicrystal configuration affects the pile-up behavior on a grain boundary. The results for the tricrystal resemble the observations for the bicrystal. The pile-up width at the grain boundaries increases with growing misorientation in the crystal structure. This corresponds to the physically expected behavior resulting from less stress annihilation for a higher twist angle. We have illustrated this relation for the angles $\alpha = 5°, 35°$ in Figure 8.7 for two representative slip systems.

The dependence of the pile-up behavior on the angle α is particularly apparent in the plastic slip distribution given in Figure 8.8. Comparing the pile-ups at the grain boundary and the Dirichlet boundary in an outer grain, an asymmetric distribution of the plastic slip is observable. In the left and the right grain, the maximum of the plastic slip is slightly shifted towards the corresponding grain boundary. This meets the physical expectations since on the outer boundaries no interaction stresses resulting from dislocations located at the other side of the boundary occur. Hence, the pile-ups on the Dirichlet boundaries are characterized by the eigenstresses and the back stress of the dislocations located in the respective grain. On the other side, the dislocation motion on the inner boundary of the outer grains is affected by the interaction with the dislocations in the central grain. The shift of the plastic slip distribution towards the grain boundary indicates attractive forces between the adjacent grains. Owing to the different stress superposition for different twist angles this behavior depends on the angle α. Regarding the plastic slip in the central grain,

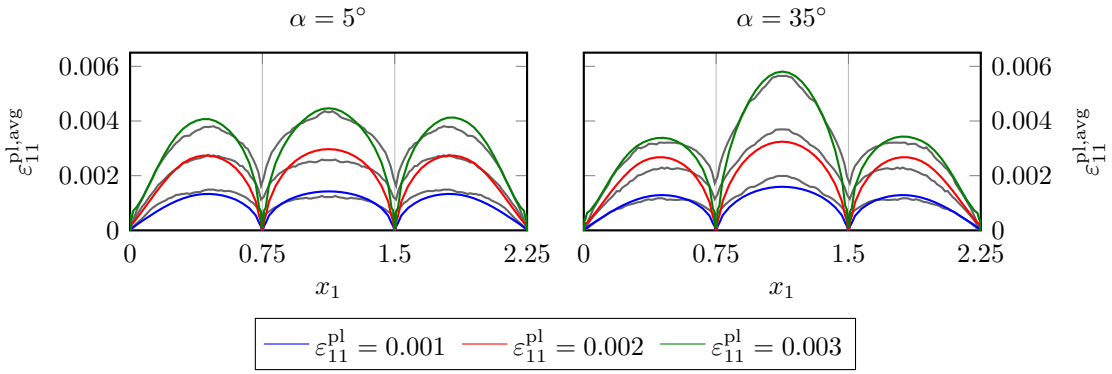

Figure 8.11: Evolution of the plastic strain for $\alpha = 5°, 35°$ with $h_0 = 0.0375\,\mu\mathrm{m}$, local degree $p = 2$ and $\triangle t = 0.5\,\mathrm{ns}$, and comparison with DDD data (gray) from Bayerschen et al. (2015)

a symmetric structure is observed consistent with the overall symmetric configuration. The misorientation angle clearly has an impact on the concrete pile-up behavior in the central grain. For $\alpha = 35°$ a significantly higher maximum of the plastic slip is obtained compared to $\alpha = 5°$.

In order to validate the numerical results for the tricrystal setting, a comparison with DDD data is given in Figure 8.11. Comparable results can be obtained by transferring the DDD configuration to the CDD setup. This requires some assumptions concerning the initial values. We have chosen a configuration that is initially constant in space. For the concrete choice of the initial values, a comparison of the macroscopic material behavior is performed, cf. Figure 8.6. The results for the total plastic strain obtained with this setting are consistent with the DDD data from Bayerschen et al. (2015). Both the position of the maxima in the plastic strain and the corresponding maximum values show a good accordance.

It is a priori uncertain which microscopic physical effects are retained and to what extent the loss of information through the averaging process from a discrete to a continuous representation of the dislocation microstructure prevails. We have shown that the interaction on a grain boundary can be represented in a satisfying way within the continuum framework we use throughout this work. The comparison to DDD data has clearly demonstrated that the expected dependence on the orientation of the adjacent grains can be observed. This means that the presented numerical approximation method reproduces the occurring short-range effects.

CHAPTER 9
Conclusion

9.1 Summary

The goal of this work was the development of a numerical approximation scheme for a continuum elastoplasticity model which incorporates the dislocation microstructure of a crystalline material. The considered physical model joins the classical linear elasticity in continuum mechanics and the discrete dislocation theory in materials science.

We used the CDD theory for the description of the kinematical properties of dislocations in the continuum. This yields a system of partial differential equations describing the evolution of dislocation densities. Using Orowan's equation, the dislocation density can be related to the plastic shear strain. This couples the macroscopic problem and the microscopic problem. For a closed theory, a constitutive law describing the motion velocity of the dislocations is necessary. The external stress state as well as the internal stresses caused by the dislocations are represented in the velocity law.

We introduced a fully-coupled numerical formulation combining a conforming finite element approximation of elastoplasticity with an implicit Runge-Kutta discontinuous Galerkin discretization of the dislocation microstructure. The formulation is fully three-dimensional and allows for multiple slip systems.

A Strang splitting method is applied for the numerical approximation of the CDD evolution equations. This allows formulating the CDD system as a vector-valued and a scalar linear conservation law each including a production term. By this means, the numerical approximation of the original nonlinear CDD system can be replaced by the approximation of two coupled linear problems. We proposed a space discretization of both problems using a discontinuous Galerkin approach. For the application in bounded geometries, suitable boundary conditions have been formulated for both free outflow and impenetrable boundaries. The discontinuous Galerkin ansatz requires the choice of numerical flux functions. We employ an upwind flux which we have derived for both problems. It is

also used for the definition of the numerical flux on the boundary satisfying the respective boundary condition. The discontinuous Galerkin space discretization is supplemented by a time discretization using the implicit midpoint rule.

The quasi-static macroscopic behavior is given by the governing balance laws subject to boundary conditions accounting for external loads. It is approximated using a finite element discretization with continuous piecewise trilinear shape functions. The coupling of the CDD system with the macroscopic problem requires a transfer operator relating the discontinuous Galerkin ansatz spaces with the conforming ansatz space for the macroscopic problem. We introduced a suitable averaging operator and proposed an evaluation scheme for the dislocation velocity based on it. This allows to compute a continuous dislocation velocity using a constitutive mobility law including the external and the internal stress state.

The presented numerical method has been validated in several benchmark tests. Analytical solutions for simplified velocity laws have been derived. They allow to examine the approximation of the CDD system. Both the space and time convergence showed the expected behavior. The numerical tests clearly demonstrated that the Strang splitting method is an appropriate instrument for the approximation of the CDD system. Comparing the space discretization depending on the polynomial degree of the discontinuous Galerkin spaces, the examinations showed that the classical finite volume method with piecewise constant ansatz functions is distinctly inferior to the discontinuous Galerkin method with higher polynomial degree. This corresponds well with the theoretically expected behavior.

Concerning the validation of the solution scheme for the macroscopic problem, a comparison of numerical results for the dislocation eigenstresses with well-known analytical reference solutions from the literature has been carried out.

We extended the presented numerical method to polycrystals. For this purpose, a numerical formulation of impenetrable grain boundaries has been implemented. The fully-coupled algorithm for polycrystals has been applied to two configurations: a single slip bicrystal and an fcc tricrystal. In both numerical tests the focus was on the dislocation interaction across the grain boundaries. Here, the difficulty is to represent the short-range effects in a continuum context. Additionally, the shock-like effect of an impenetrable barrier inside the volume is numerically challenging. In order to retain the local physical effects in the continuum formulation, we use graduated meshes that are refined close to impenetrable boundaries. In combination with a Taylor-type yield stress formulation implicitly ensuring a declining dislocation velocity towards an impenetrable boundary, a stable numerical scheme is obtained. Both test configurations showed the expected physical behavior in the numerical tests. The results for the tricrystal have been compared to smaller scale reference

outcomes based on the DDD method. We demonstrated that our numerical results are in good accordance with the comparison data.

9.2 Outlook

The precise modeling of physical effects occurring on atomic scale in a continuum framework is the topic of ongoing research. The numerical method provided in this work can be extended and modified in a straightforward way in order to account for advances in the modeling of dislocation motion and interaction. It thus allows to investigate further developments of the physical model numerically in a three-dimensional setting. This can help to verify new approaches in a direct way by comparison with results from models based on smaller scales or experimental data.

In this work, we limited ourselves to dislocation gliding. A natural extension is the consideration of further types of dislocation motion. A first step towards the representation of cross-slip in the CDD model has recently been accomplished by Monavari and Zaiser (2018). We refer to Stricker et al. (2018) for an alternative view on dislocation multiplication mechanisms like cross-slip based on DDD simulations and a discussion on the impact on CDD. These works indicate that the incorporation of cross-slip in the presented numerical approximation method is a promising approach for a more detailed prediction of dislocation motion.

With an improved understanding of the underlying physical relations of dislocation motion and their representation in a continuum framework, a more precise numerical simulation of elastoplasticity is achievable. In conjunction with appropriate and accurate numerical methods, the overall goal of a dislocation based plasticity model suited for engineering applications is reached step by step.

Danksagung

Bei Prof. Dr. Christian Wieners bedanke ich mich für die Möglichkeit, bei ihm zu promovieren. Ich habe viel von ihm gelernt und bin dankbar dafür, dass er bei Bedarf immer bereit war, viel Zeit zu investieren und das zu tun, was er vermutlich am besten kann: Probleme lösen.

Ich danke Prof. Dr. Willy Dörfler für die Übernahme des Korreferats. Außerdem möchte ich mich bei ihm für die gute und unkomplizierte Betreuung im Hauptdiplom – insbesondere kurz vor der Abgabe meiner Diplomarbeit – bedanken.

Wie eingangs schon erwähnt, ist diese Arbeit im Rahmen der DFG-Forschergruppe FOR1650 entstanden. Die daraus resultierende Zusammenarbeit mit dem Institut für Angewandte Materialien – Computational Materials Science war für mich von großer Bedeutung. Ich danke Dr. Katrin Schulz dafür, dass sie von Anfang an immer als Ansprechpartnerin zur Verfügung stand. Darüber hinaus danke ich allen, die im Laufe der Zeit mit meinem Programm gearbeitet und dabei eine Vielzahl an Fehlern gefunden haben, vor allem Markus Sudmanns.

Meine Zeit am Institut für Angewandte und Numerische Mathematik 3 hat mir sehr große Freude bereitet. Ich bedanke mich bei allen aktuellen und ehemaligen Kollegen. Vielen Dank für Kuchenwetten, Spieleabende, fachlichen Rat, mehr und weniger sinnvolle Diskussionen, Geschenkideen, die gemeinsame künstlerische Verwendung von Klebezetteln und vieles mehr an Andreas, Benny, Bob, Christian, Christine, Daniel, Daniel, Daniel, Ekkachai, Fabio, Johannes, Jonathan, Julian, Julian, Katharina, Laura, Marcel, Nathalie, Niklas, Patrick, Philip, Ramin, Simon und Sonja sowie Tobias Jahnke, Andreas Rieder und Christian Wieners. Besonders hervorheben möchte ich Julian und Tine, die beide einen großen Einfluss auf meinen Arbeitsalltag hatten. An Julian übergebe ich hiermit offiziell das Amt des dienstältesten Doktoranden in der Hoffnung, dass er es nur kurze Zeit innehaben wird. Außerdem möchte ich mich an dieser Stelle bei Luca bedanken, der mir erklärt hat, wie wichtig Danksagungen sind.

Meinem Verlobten Stefan danke ich für die Selbstverständlichkeit, mit der er mich in der gesamten Zeit und ganz besonders in den letzten Monaten unterstützt, bestärkt, aufgemuntert und mit Essen versorgt hat.

Bei meiner Familie bedanke ich mich für die vielfältige Unterstützung, die sie mir jederzeit entgegenbringt. Vielen Dank an meine Mutter, Felix und Ingo.

Mein größter Dank gilt meinem Vater, der schon früh mein Interesse an technischen Fragestellungen geweckt hat. Auch wenn ich seinem Wunsch, dass ich ebenfalls Maschinenbau studiere, nicht gefolgt bin, so habe ich doch einen ähnlichen Weg eingeschlagen wie er. Dass ich diesen Weg inzwischen ohne ihn gehen muss, macht mich unfassbar traurig. In tiefer Dankbarkeit für all das, was er für mich getan hat, widme ich ihm diese Arbeit.

Lydia Wagner
Karlsruhe, im April 2019

Bibliography

A. Acharya. A model of crystal plasticity based on the theory of continuously distributed dislocations. *Journal of the Mechanics and Physics of Solids*, 49(4):761–784, 2001.

N. Ahmed and A. Hartmaier. A two-dimensional dislocation dynamics model of the plastic deformation of polycrystalline metals. *Journal of the Mechanics and Physics of Solids*, 58(12):2054–2064, 2010.

A. Arsenlis, D. M. Parks, R. Becker, and V. V. Bulatov. On the evolution of crystallographic dislocation density in non-homogeneously deforming crystals. *Journal of the Mechanics and Physics of Solids*, 52(6):1213–1246, 2004.

D. Balint, V. Deshpande, A. Needleman, and E. Van der Giessen. Discrete dislocation plasticity analysis of the grain size dependence of the flow strength of polycrystals. *International Journal of Plasticity*, 24(12):2149–2172, 2008.

E. Bayerschen, M. Stricker, S. Wulfinghoff, D. Weygand, and T. Böhlke. Equivalent plastic strain gradient plasticity with grain boundary hardening and comparison to discrete dislocation dynamics. *Proceedings of the Royal Society A*, 471(2184):20150388, 2015.

B. A. Bilby, R. Bullough, and E. Smith. Continuous distributions of dislocations: a new application of the methods of non-Riemannian geometry. *Proceedings of the Royal Society A*, 231(1185):263–273, 1955.

B. Devincre, L. Kubin, and T. Hoc. Physical analyses of crystal plasticity by DD simulations. *Scripta Materialia*, 54(5):741–746, 2006.

D. A. Di Pietro and A. Ern. *Mathematical Aspects of Discontinuous Galerkin Methods*, volume 69 of *Mathématiques et Applications*. Springer, Berlin, 2012.

A. El-Azab. Statistical mechanics treatment of the evolution of dislocation distributions in single crystals. *Physical Review B*, 61(18):11956–11966, 2000.

A. Ern and J.-L. Guermond. *Theory and Practice of Finite Elements*, volume 159 of *Applied Mathematical Sciences*. Springer, New York, 2004.

P. Franciosi, M. Berveiller, and A. Zaoui. Latent hardening in copper and aluminium single crystals. *Acta Metallurgica*, 28(3):273–283, 1980.

N. M. Ghoniem and L. Z. Sun. Fast-sum method for the elastic field of three-dimensional dislocation ensembles. *Physical Review B*, 60(1):128–140, 1999.

I. Groma. Link between the microscopic and mesoscopic length-scale description of the collective behavior of dislocations. *Physical Review B*, 56(10):5807–5813, 1997.

I. Groma, F. Csikor, and M. Zaiser. Spatial correlations and higher-order gradient terms in a continuum description of dislocation dynamics. *Acta Materialia*, 51(5):1271–1281, 2003.

M. E. Gurtin. *An introduction to continuum mechanics*, volume 158 of *Mathematics in Science and Engineering*. Academic press, New York, 1982.

E. Hall. The Deformation and Ageing of Mild Steel: III Discussion of Results. *Proceedings of the Physical Society. Section B*, 64(9):747–753, 1951.

J. S. Hesthaven and T. Warburton. *Nodal Discontinuous Galerkin Methods*, volume 54 of *Texts in Applied Mathematics*. Springer, New York, 2008.

J. P. Hirth and J. Lothe. *Theory of dislocations*. John Wiley & Sons, New York, 2$^{\text{nd}}$ edition, 1982.

T. Hochrainer. *Evolving systems of curved dislocations: Mathematical foundations of a statistical theory*, volume 34 of *Schriftenreihe Werkstoffwissenschaft und Werkstofftechnik*. Shaker, Aachen, 2007. PhD thesis.

T. Hochrainer. Multipole expansion of continuum dislocations dynamics in terms of alignment tensors. *Philosophical Magazine*, 95(12):1321–1367, 2015.

T. Hochrainer, M. Zaiser, and P. Gumbsch. A three-dimensional continuum theory of dislocation systems: kinematics and mean-field formulation. *Philosophical Magazine*, 87 (8-9):1261–1282, 2007.

T. Hochrainer, S. Sandfeld, M. Zaiser, and P. Gumbsch. Continuum dislocation dynamics: Towards a physical theory of crystal plasticity. *Journal of the Mechanics and Physics of Solids*, 63:167–178, 2014.

D. Hull and D. J. Bacon. *Introduction to dislocations*. Butterworth-Heinemann, Amsterdam, 5$^{\text{th}}$ edition, 2011.

R. Kapoor and N. Verdhan. Interaction of dislocation pile-up with a low-angle tilt boundary: a discrete dislocation dynamics study. *Philosophical Magazine*, 97(7):465–488, 2017.

K. Kondo. On the geometrical and physical foundations of the theory of yielding. *Proceedings of the 2nd Japan National Congress for Applied Mechanics*, 2:41–47, 1952.

E. Kröner. *Kontinuumstheorie der Versetzungen und Eigenspannungen*, volume 5 of *Ergebnisse der angewandten Mathematik*. Springer, Berlin, 1958.

L. Kubin and G. Canova. The modeling of dislocation patterns. *Scripta Metallurgica et Materialia*, 27(8):957–962, 1992.

L. Kubin, B. Devincre, and T. Hoc. Modeling dislocation storage rates and mean free paths in face-centered cubic crystals. *Acta Materialia*, 56(20):6040–6049, 2008.

R. Kumar, L. Nicola, and E. V. der Giessen. Density of grain boundaries and plasticity size effects: A discrete dislocation dynamics study. *Materials Science and Engineering: A*, 527(1-2):7–15, 2009.

R. J. LeVeque. *Finite volume methods for hyperbolic problems*, volume 31 of *Cambridge Texts in Applied Mathematics*. Cambridge University Press, Cambridge, 2011.

J. E. Marsden and T. J. Hughes. *Mathematical foundations of elasticity*. Dover Publications, New York, 1994.

M. Monavari and M. Zaiser. Annihilation and sources in continuum dislocation dynamics. *Materials Theory*, 2(3), 2018.

M. Monavari, M. Zaiser, and S. Sandfeld. Comparison of closure approximations for continuous dislocation dynamics. *Materials Research Society Proceedings*, 1651, 2014.

M. Monavari, S. Sandfeld, and M. Zaiser. Continuum representation of systems of dislocation lines: A general method for deriving closed-form evolution equations. *Journal of the Mechanics and Physics of Solids*, 95:575–601, 2016.

T. Mura. Continuous distribution of moving dislocations. *Philosophical Magazine*, 8(89): 843–857, 1963.

J. Nye. Some geometrical relations in dislocated crystals. *Acta Metallurgica*, 1(2):153–162, 1953.

E. Orowan. Zur Kristallplastizität. *Zeitschrift für Physik*, 89:605–659, 1934.

N. J. Petch. The cleavage strength of polycrystals. *Journal of the Iron and Steel Institute*, 174:25–28, 1953.

Y. Saad and M. H. Schultz. GMRES: A generalized minimal residual algorithm for solving nonsymmetric linear systems. *SIAM Journal on Scientific and Statistical Computing*, 7 (3):856–869, 1986.

S. Sandfeld. *The Evolution of Dislocation Density in a Higher-order Continuum Theory of Dislocation Plasticity*, volume 64 of *Schriftenreihe Werkstoffwissenschaft und Werkstofftechnik*. Shaker, Aachen, 2010. PhD thesis.

S. Sandfeld, T. Hochrainer, P. Gumbsch, and M. Zaiser. Numerical implementation of a 3D continuum theory of dislocation dynamics and application to micro-bending. *Philosophical Magazine*, 90(27-28):3697–3728, 2010.

S. Sandfeld, E. Thawinan, and C. Wieners. A link between microstructure evolution and macroscopic response in elasto-plasticity: Formulation and numerical approximation of the higher-dimensional Continuum Dislocation Dynamics theory. *International Journal of Plasticity*, 72:1–20, 2015.

S. Schmitt, P. Gumbsch, and K. Schulz. Internal stresses in a homogenized representation of dislocation microstructures. *Journal of the Mechanics and Physics of Solids*, 84:528–544, 2015.

A. Schulz. *Numerical Analysis of the Electro-Magnetic Perfectly Matched Layer in a Discontinuous Galerkin Discretization*. PhD thesis, Karlsruhe Institute of Technology, Karlsruhe, 2015.

K. Schulz, L. Wagner, and C. Wieners. A mesoscale continuum approach of dislocation dynamics and the approximation by a Runge-Kutta discontinuous Galerkin method. *International Journal of Plasticity*, 120:248–261, 2019.

J. Senger, D. Weygand, P. Gumbsch, and O. Kraft. Discrete dislocation simulations of the plasticity of micro-pillars under uniaxial loading. *Scripta Materialia*, 58(7):587–590, 2008.

G. Strang. On the construction and comparison of difference schemes. *SIAM Journal on Numerical Analysis*, 5(3):506–517, 1968.

M. Stricker, J. Gagel, S. Schmitt, K. Schulz, D. Weygand, and P. Gumbsch. On slip transmission and grain boundary yielding. *Meccanica*, 51(2):271–278, 2016.

M. Stricker, M. Sudmanns, K. Schulz, T. Hochrainer, and D. Weygand. Dislocation multiplication in stage II deformation of fcc multi-slip single crystals. *Journal of the Mechanics and Physics of Solids*, 119:319–333, 2018.

G. I. Taylor. The Mechanism of Plastic Deformation of Crystals. *Proceedings of the Royal Society A*, 145(855):362–404, 1934.

D. Weygand, L. H. Friedman, E. van der Giessen, and A. Needleman. Aspects of boundary-value problem solutions with three-dimensional dislocation dynamics. *Modelling and Simulation in Materials Science and Engineering*, 10(4):437–468, 2002.

C. Wieners. Distributed point objects. A new concept for parallel finite elements. In *Domain Decomposition Methods in Science and Engineering*, volume 40 of *Lecture Notes in Computational Science and Engineering*, 175–182, Springer, Berlin, 2005.

C. Wieners. A geometric data structure for parallel finite elements and the application to multigrid methods with block smoothing. *Computing and Visualization in Science*, 13 (4):161–175, 2010.

M. Zaiser. Local density approximation for the energy functional of three-dimensional dislocation systems. *Physical Review B*, 92(17):174120, 2015.